

Gold nanoparticles as a new tool in amyloid studies

Présentée le 5 juin 2020

à la Faculté des sciences et techniques de l'ingénieur
Laboratoire des nanomatériaux supramoléculaires et interfaces - Chaire Constellium
Programme doctoral en science et génie des matériaux

pour l'obtention du grade de Docteur ès Sciences

par

Urszula Beata CENDROWSKA

Acceptée sur proposition du jury

Prof. P. Bowen, président du jury
Prof. F. Stellacci, Prof. H. Lashuel, directeurs de thèse
Prof. M. Faendrich, rapporteur
Prof. B. Rothen-Rutishauser, rapporteuse
Prof. G. Dietler, rapporteur

Acknowledgements

Few years ago, I arrived to Lausanne to start my two months internship in prof. Giovanni Dietler group. Suddenly, these two months turned into few years of work at EPFL. No one was expecting this fortunate turn of events, especially me, as I was living in Lausanne for several months with only few clothes and personal items that could fit in one travelling bag. When I look back at my time in Lausanne, I can only think of fantastic people who I have met and who influenced my life in a positive way. I would like to take a moment and express my appreciation for the support, trust and help I received in this period of my life.

First, I would like to thank my supervisor, prof. Francesco Stellacci. I truly appreciate his mentoring – he left the space for my curiosity and my ideas, yet I always could count on his guidance and support when needed. I really learned and grew under his supervision, but I am especially grateful for the trust he placed in me and in this project.

I owe the final shape of this thesis to prof. Hilal Lashuel, who was my co-advisor during my PhD studies. I would like to thank him for his valuable contribution in the form of mentoring and readiness to share excellent quality samples from his lab. They added immense value to this thesis and became a scaffold on which this project was built.

At this point I need to mention Dr. Paulo H. Jacob Silva, whom I was shadowing for the first year of my PhD. If not for his curiosity, knowledge and persistence, this project would never exist. He placed the fundamentals of this project, and whether he likes it or not, he is a grandfather of this thesis.

I would like to thank my thesis committee – prof. Paul Bowen, prof. Rothen-Rutishauser, prof. Marcus Fändrich and prof. Giovanni Dietler for accepting to be in my thesis committee and evaluating my work. I especially would like to thank prof. Giovanni Dietler who instilled scientific curiosity in me and actually kick started my career. I also would like to thank prof. Marcus Fändrich for contributing to this project by sharing priceless *ex vivo* material, which raised the significance level of this thesis.

This heavily cryo TEM oriented project would not fly as high without the training and support I received from CIME facility. I especially would like to thank Dr. Davide Dermatas for patient introduction to cryo TEM technique. I am also very grateful to Ms. Chiara Donini, who kept helping me with administrative issues, especially during my internship in Germany.

Being a member of SuNMIL group was one of the best parts of my PhD studies. I need to express my appreciation for prof. Francesco Stellacci's nose for his employees. SuNMIL was always consisted of trustworthy, helpful and kind people. Here, I would like to thank SuNMIL members, in particular: Sergio, Matej, Rosie, Zhi, Elif, Ahmet, Simone G., Matteo, Suyiang, Quy, Francesca, Nicolo', Ting, Lixia, Yong and my polish buddy Łukasz, for making my everyday work fun and pleasant. However, there is a special place in my heart for a few people with whom I developed a special bond: Pelin was more fun part of our Pula duet, her kindness and outgoing attitude was often bringing me up. Evi is my brave, smart and thoughtful role model. Ozgun's self-confidence was always an object of my admiration. Anna was my fun and supportive iSwitch companion. Nikos is my beautiful muse and the best source of inspiration. How fortunate, that we still did not kill each other! I would lose a really valuable part of my life.

I would also like to thank very helpful, welcoming and professional people from my co-advisor's group – LMNN. I would especially like to express my gratitude to Anass, Senthil, and Sophie, Nadine, Anne-Laurie and Marie for immense help and support.

I definitely need to mention my outside-work friends who kept me company during all of these years. Simone R., Simone M., Luka, Manu, Alex and Petar were always there to share time and good word. I am so grateful, that I had a chance to meet you. Beside them, far away in a different country, there was a group of people that always supported me remotely and believed in me despite the distance. I would like to thank my polish friends: Adzia, Majki, Fjotek, Kasia, Jasiu, and Andrzej, who also paid his price for my PhD studies. These people are the best.

Last, but not least I would like to thank my family – my sister and my parents. My older and wise sister Ola, for her understanding and support. Szczególne podziękowania należą się moim rodzicom, którzy zapewnili mi wspaniały start w życiu, zawsze we mnie wierzyli i pozwalali mi na ściganie moich ambicji. Dziękuję za siłę, cierpliwość, wyrozumiałość i nieustanne wsparcie.

Abstract

The misfolding and self-assembly of proteins into fibrils is a hallmark of several neurodegenerative and systemic diseases. These disease-associated proteins have the propensity to form fibrils with a cross- β sheet structure, called amyloids. Amyloids can assemble into structures of various morphologies and increasing evidence suggests, that this polymorphism gives rise to distinct toxicity and pathology spreading patterns. This was observed for fibrils formed under different conditions or derived from different diseased tissues. Validation of this hypothesis remains challenging due to the laborious methods that are employed to enable the direct visualization and analysis of amyloid fibrils polymorphism in hydrated and complex biological samples.

This thesis presents a novel microscopy method for assessing amyloid fibrils polymorphism using small gold nanoparticles (~ 3 nm diameter) coated with a mixture of 1-octanethiol and 11-mercapto-1-undecanesulfonate. These nanoparticles efficiently label amyloid fibrils that were produced *in vitro* as well as fibrils that were derived from tissues of human patients (*ex vivo*), that suffered from diseases linked to amyloid aggregates. Decoration with gold nanoparticles enabled the rapid visualization of the labelled contours of the amyloid fibrils that were imaged using Cryogenic transmission electron microscopy (cryo TEM). This method rendered the structural analysis of the fibrils relatively easy.

Due to the labelling of the fibrils, we were able to observe a wide range of the morphologically polymorphic amyloids for *in vitro* derived samples. Moreover, comparative analysis of these fibrils with *ex vivo* derived amyloids, revealed significant differences in the morphological homogeneity. Our results showed an unexpected uniformity of the *ex vivo* derived fibrils, highlighting the influence of the milieu on the aggregation of amyloid fibrils (Chapter 4 and 5).

The nanoparticles were also used as a probe to analyze amyloid fibrils surfaces. For example, we showed that sequence modification influences the efficiency of amyloid fibril decoration with our nanomaterial. In Chapter 3, we present that two types of fibrils and their truncated versions, were differently labelled due to the modification of their charged domains. This shows, that we can assess the changes in the primary structure of the amyloidogenic protein by monitoring the interactions between the nanoparticles and the surface of amyloids.

Furthermore, results presented in Chapter 6 show that the decoration of the amyloids is possible in various types of biological milieu, including cerebrospinal fluids (CSF) and cell lysates. This finding suggests that our gold nanomaterial can potentially be used for targeted amyloid decoration in more complex systems, such as cells or tissues.

The results presented in this thesis show that gold nanoparticles may represent a novel tool for rapid determination of the polymorphism of *in vitro* and *ex vivo* derived amyloid fibrils. We demonstrate

and validate the advantages of our technique such as simplicity, quick data acquisition and analysis, stability of the labelling and high efficiency of decoration in the complex samples. This can be of high value for the studies of amyloid related diseases as this method allows for relatively easy screen of fibrils derived from the patients' tissue and recognition of polymorphic species.

Keywords: amyloids, gold nanoparticles, polymorphism, cryo TEM, contrast marker

Riassunto

Il ripiegamento incorretto (misfolding) e l'autoassemblaggio di proteine in fibrille sono caratteristici di diverse malattie neurodegenerative e sistemiche. Queste proteine associate alle malattie sono propense a formare fibrille con una struttura a foglietto β chiamate amiloidi, che possono assemblarsi in strutture di svariate morfologie. Evidenze crescenti suggeriscono che questo polimorfismo dia origine a diversa tossicità e a diversi modelli di avanzamento della patologia. Questo è stato osservato in fibrille formatesi in condizioni differenti o ottenute da diversi tessuti malati. La validazione di questa ipotesi è complicata in quanto i metodi utilizzati per la visualizzazione diretta e l'analisi del polimorfismo delle fibrille in campioni biologici complessi e idratati sono particolarmente laboriosi. In questa tesi viene presentato un nuovo metodo di microscopia per lo studio del polimorfismo delle fibrille amiloidi tramite l'uso di piccole nanoparticelle d'oro (diametro di ~ 3 nm) ricoperte con una miscela di 1-ottantiolo e 11-mercapto-1-undecansulfonato. Queste nanoparticelle marcano efficacemente fibrille amiloidi sia prodotte *in vitro* sia derivate (*ex vivo*) da tessuti di pazienti umani affetti da malattie associate ad aggregazione amiloide. La decorazione delle fibrille con nanoparticelle d'oro permette una rapida visualizzazione dei loro contorni, quando osservate tramite microscopia crioelettronica (cryo TEM). Questo metodo rende l'analisi strutturale delle fibrille relativamente semplice.

Grazie alla marcatura delle fibrille abbiamo potuto osservare una gran varietà di amiloidi morfologicamente polimorfi per i campioni ottenuti *in vitro*. Inoltre, un'analisi comparativa di queste fibrille con quelle ottenute *ex vivo* ha rivelato differenze significative nell'omogeneità morfologica. I nostri risultati hanno mostrato un'inattesa uniformità delle fibrille derivate *ex vivo*, sottolineando l'influenza dell'ambiente sui processi aggregativi delle stesse (Capitoli 4 e 5).

Le nanoparticelle sono anche state usate come sonda per analizzare la superficie delle fibrille amiloidi. Per esempio, abbiamo mostrato come modifiche nella sequenza influenzino l'efficienza di decorazione con il nostro nanomateriale. Nel Capitolo 3, mostriamo come due tipi di fibrille e le loro versioni troncate siano state marcate in modo diverso in seguito alla modifica dei loro domini carichi. Questo dimostra che possiamo rilevare cambiamenti nella struttura primaria delle proteine amiloidogeniche osservando le interazioni tra le nanoparticelle e la superficie degli amiloidi.

Inoltre, I risultati presentati nel Capitolo 6 mostrano che la decorazione con gli amiloidi è possibile in vari tipi di ambiente biologico, tra cui i fluidi cerebrospinali (CSF) e il lisato cellulare. Questo risultato suggerisce che il nostro nanomateriale possa essere potenzialmente utilizzato per la decorazione di amiloidi in sistemi più complessi, quali cellule e tessuti.

I risultati presentati in questa tesi mostrano che le nanoparticelle d'oro possono rappresentare un nuovo strumento per la rapida determinazione del polimorfismo delle fibrille amiloidi *in vitro* ed *ex*

vivo. Vengono dimostrati e convalidati i vantaggi della nostra tecnica quali semplicità, rapidità di acquisizione e analisi dati, stabilità della marcatura ed alta efficienza della decorazione nei campioni complessi. Questo può essere molto importante per gli studi sulle malattie associate agli amiloidi poiché questo metodo consente uno screening relativamente semplice delle fibrille derivate dal tessuto dei pazienti ed il riconoscimento delle specie polimorfe.

Parole chiave: amiloidi, nanoparticelle d'oro, polimorfismo, cryo TEM, marcatori di contrasto

Table of content

Acknowledgements	i
Abstract	iii
Riassunto	v
Abbreviations	ix

Chapter 1

Motivation of the study and thesis structure	1
1.1 Motivation of the study	1
1.2 Thesis structure	4

Chapter 2

Introduction	7
2.1 Protein misfolding and amyloids	7
2.1.1 Amyloids and human diseases	12
2.1.2 Amyloid polymorphism and strains	16
2.1.3 Techniques used for studying amyloid fibrils.....	19
2.2 Nanoparticles	22
2.2.1 Nanoparticles in biosciences	23
2.2.2 Nanoparticles amyloid studies	23
2.2.3 State of art	27

Chapter 3

Investigating amyloid surface with the use of nanoparticles	33
3.1 Introduction.....	33
3.2 Results and discussion	36
3.3 Conclusions.....	46
3.4 Materials and methods	48

Chapter 4

Investigating polymorphism of the recombinant and synthetic fibrils with use of the gold nanoparticles	55
4.1 Introduction.....	55
4.1.1 Periodicity of the fibrils as a function of the number of protofilaments.....	56
4.2 Results and discussion	60
4.2.1 A β ₄₀ analysis	60

4.2.2 R2 analysis	64
4.3 Conclusion	68
4.4 Materials and methods	70
Chapter 5	
Morphological analysis of human derived amyloids	73
5.1 Introduction.....	73
5.2 Results and discussion	75
5.2.1 Comparison between ex vivo and in vitro obtained fibrils	82
5.3 Conclusions.....	85
5.4 Materials and methods	86
Chapter 6	
Stability of the decoration and labelling in complex solutions	89
6.1 Introduction.....	89
6.2 Results and discussion	90
6.2.1 Stability of decoration with the nanoparticles.....	90
6.2.2 Labelling of amyloid fibrils in complex solutions.....	96
6.3 Conclusions.....	103
6.4 Materials and methods	104
Chapter 7	
Conclusions and outlook.....	107
7.1 Summary and conclusions	107
7.2 Outlook.....	109
7.2.1 Amyloid growth and behavior monitoring with the use of liquid cell TEM	109
7.2.2 Separation of amyloid polymorphic species with use of nanoparticles	111
7.2.3 Facilitating microscopy studies of ex vivo derived amyloids and in vivo studies of aggregates	114
7.2.4 Materials and methods	115
References	116
Curriculum Vitae.....	130

Abbreviations

AD	Alzheimer's Disease
AFM	Atomic Force Microscopy
ATTR	transthyretin amyloidosis
A β	Amyloid β
BAM	N-tert-butylacrylamide
Cryo TEM	Cryogenic Transmission Electron Microscopy
dSTORM	direct Stochastic Optical Reconstruction Microscopy
Fab	Antigen binding fragment
FL Httex1 43Q	Full length exon1 huntingtin with 43 glutamines
HD	Huntington's Disease
HSA	Hierarchical assembly model
MUP	11-mercaptoundecylphosphoric acid
MUS	11-mercapto-1-undecanesulfonate
N17	17 amino acids in the N terminus
NAC	Non A β component
NIPAM	N-isopropylacrylamide
nPHF	Native Paired Helical Filaments
NPs	Nanoparticles
NT Httex1 43Q	N truncated exon1 huntingtin with 43 glutamines
OT	1-octanethiol
PET	Positron Emission Tomography
PD	Parkinson's Disease
PHF	Paired Helical Filaments
polyQ	Poly glutamine region

SDD – AGE	Semi – Denaturing Detergent Agarose Gel Electrophoresis
ssNMR	Solid State Nuclear Magnetic Resonance
STEM	Scanning Transmission Electron Microscopy
TEM	Transmission electron microscopy
TGA	Thermogravimetric analysis
ThT	Thioflavin T
TMA	N,N,N-trimethyl(11-mercaptoundecyl)ammonium chloride
TTR	Transthyretin
WT	Wild type
ZW	Zwitterionic

Chapter 1

Motivation of the study and thesis structure

1.1 Motivation of the study

The quality and expectancy of human life underwent enormous change and roughly doubled during the last century (1). Modern medicine, food accessibility and technology have made our lives easier, better and exceptionally long in comparison to other species of the animal kingdom. Wild animals that live in their natural habitat rarely become senescent (2), which makes surviving to old age specific for the human species, by limiting the most infectious diseases, improving hygiene and inventing antibiotics and vaccines. We have replaced hunting for mammoths with hunting for anti-ageing products. Life expectancy becomes longer for each consecutive generation and scientific predictions assume that this trend will be preserved (1). However optimistic this may sound at first, we need to give a second look to this phenomenon to understand the possible disadvantages and think on how to address them, as increased life expectancy will increase the prevalence of age-related diseases, such as Dementia, Alzheimer's disease, and Parkinson's disease.

The top three leading causes of death in 1900's: (I) pneumonia and influenza, (II) tuberculosis and (III) diarrhea and enteritis are replaced today with heart diseases, cancer and stroke. Alzheimer's Disease (AD), that falls under the umbrella of dementia disorders, is nowadays among the 10 leading causes of death in some populations (3). Despite its rather low place in the ranking, it attracts a lot of attention since living with dementia can last for several years (4) during which the affected individuals are rarely active, productive or living a fulfilling life. In fact, the most drastic everyday experiences of patients affected by dementia are fear of being a burden, fear of losing control and independence and suicidal ideations (5, 6). In 2015, the number of people worldwide affected by dementia was estimated to be around 47 million and this number is expected to increase to 131 million by the year 2050 (7). Therefore, without effective therapies to treat or slow the progression of dementia and other aging-related disorders, these diseases represent a major threat to national economies, especially of developed nations. Moreover, these kind of disorders are a huge burden not only for affected people but also their caretakers and society at large (8, 9).

Dementia is characterized by decline of cognitive functions and impaired memory. In 2016 1.5-2% of EU population had dementia syndromes (10) and 50-70% of people dealing with such disorders were diagnosed with Alzheimer's Disease (7). Several other neurodegenerative diseases are also associated with dementia and cognitive decline, including Parkinson's Disease (PD), Huntington's disease (HD) and Dementia with Lewy Bodies (DLB) (11). Despite the fact that these age-related neurodegenerative diseases affect different brain regions and are manifested in different clinical symptoms, increasing evidence point towards common mechanisms of pathogenesis and possibly common therapeutic and intervention strategies. At the pathological levels, AD, PD, HD and DLB are all characterized by pathological cytoplasmic (AD, PD, HD, DLB) and extracellular (AD) proteinaceous inclusions and deposits (12, 13). These deposits form as a result of the misfolding, accumulation and aggregation of specific proteins into insoluble, highly ordered unbranched protein fibrils. Such fibrillar structures are consisting of stacked laterally misfolded monomers with assumed β -sheet structure (14). Despite the fact, that proteins linked to these diseases are distinct and do not share sequence or structural homology, they form fibrils that share a characteristic cross- β -sheet structures. These structural features and the binding of these pathological aggregates to hydrophobic dyes such as Congo red and Thioflavin T have led to the classification of these filamentous aggregates as amyloids (15, 16). Several other diseases are characterized by protein misfolding and amyloid formation in peripheral organs, including cataract or type II diabetes, nonneuropathic systemic amyloidosis, and immunoglobulin light chain amyloidosis (17).

Even though amyloids consist of one type of misfolded protein, they exhibit a high degree of structural and morphological diversity and many aspects related to their mechanisms of formation and clearance have still to be clarified (18). There are many ways of approaching this problem and the number of studies on dementia and other amyloid related disorders is rapidly increasing. Unfortunately, despite the effort that the scientific community is undertaking, so far there is no effective therapy to treat or slow the progression of most amyloid related neurodegenerative disorders (7).

Cryogenic Transmission Electron Microscopy (cryo TEM) studies have shown that amyloid fibrils comprise of 2-8 protofilaments, that can interact with each other in various manners to give rise to amyloid fibrils with distinct structures and morphologies (19, 20). Propensity of

amyloid fibrils to exist in various forms, stem from the (I) ability of the protein to fold in different ways (21) and (II) interactions between the protofilaments, such as their number and way of intertwining (20). To this day, studies performed on different polymorphic species highlighted the differences in various features between these assemblies such as toxicity (22), nano-mechanics (23) or kinetics (24).

In vitro, polymorphism of the amyloids can be induced by the external environment, such as applied agitation, specific temperature or specific ionic strength during the aggregation process (25–29). However, the population of fibrils very often remains heterogenous even in the same batch (30, 31). Some polymorphism of the fibrils derived *ex vivo* was also observed, for example in the case of tau fibrils from a patient suffering from AD (32) or amyloids originating from animals and patients affected with systemic amyloidosis (33).

Recent studies suggest, that amyloid polymorphism may be correlated with the diversity of the AD disease onset and course (34, 35). Variation of clinical presentation and persistence of AD and other neurodegenerative disorders is well known (21) and increasing evidence suggests that the clinical variability in the disease may be connected to the polymorphism of amyloid and tau fibrils in AD brains (36). Establishing a relation between the type of the amyloid polymorph and disorder symptoms would be a great contribution to the dementia field. Connecting polymorph types with exact symptoms of dementia would improve current therapeutic methods by, for example, allowing the design of more precise and maybe personalized drugs. Moreover, knowledge about the specific influence of each polymorph would improve prognosis for patients affected by one of the polymorph species and it would help in developing more effective individual ways of treatment.

One of the fundamental factors that determines the existence of polymorphic species is the distinct morphology of the fibrils. This can be examined with the use of various types of microscopic techniques such as Atomic Force Microscopy (37), Transmission Electron Microscopy (TEM) (33) or cryo TEM (38). Each of them can deliver a specific type of information about the studied fibrils, however they all can introduce some artefacts to the measured sample. There is no rapid and flawless approach to characterize polymorphism in amyloids.

In this thesis, we propose the use of gold nanoparticles, which efficiently label synthetic, recombinant and native amyloid fibrils in a specific manner that highlights their polymorphism and morphological features. We also demonstrate how nanoparticles can be used in the probing of the amyloid surface, by monitoring the interactions between nanoparticles and fibrils composed of modified and unmodified amyloidogenic proteins. In order to image various amyloid fibrils labelled with the nanoparticles, we applied cryo TEM. We could obtain the same labeling degree and efficiency on the recombinant, synthetic and human tissue-derived fibrils. This enabled the morphological analysis and comparison between amyloids obtained *ex vivo* and *in vitro*. The results support the hypothesis that the physiological milieu significantly influence fibril structure morphology. Our work demonstrates that the use of nanoparticles provides an immediate and easy method to investigate the polymorphism of amyloids in minute amounts of samples under hydrated conditions. This approach offers several advantages, including (I) the ability to investigate complex samples without the need of extensive sample processing and (II) possibility of using only small amounts of the sample for the measurements. This facilitates sample screening and the determination of the fibrils' polymorphism in human derived samples, including organ-derived aggregates and amyloids in complex mixtures. Collectively, our work demonstrates that gold nanoparticles combined with cryo TEM technique represent a powerful tool candidate for the studies of amyloid polymorphism. We show, that our nanomaterial can be applied in the studies of the *in vitro* obtained amyloids, as well as more complex samples, derived from patients. Moreover, increasing the contrast and accelerating the sample screening makes the analysis of the aggregates much faster, easier and cheaper, which may open a new chapter for future treatment of dementia and other diseases related to amyloid aggregation.

1.2 Thesis structure

This thesis is structured as follows:

Chapter 2 introduces the reader to the concept of protein misfolding leading to the amyloid aggregation, fibril polymorphism and the role of amyloids in human diseases. The second part of the chapter focuses on metal nanoparticles and their current use in neuroscience. The last section covers the state of the art and describes briefly the previous results obtained on the use of gold nanoparticles described in this thesis.

Chapter 3 focuses on the use of nanoparticles as a probing material for amyloid surface, by monitoring propensity of the amyloid fibrils to the decoration. This work is done on (I) two

variants of Huntingtin exon1 protein that differ in the presence of N terminus and (II) two variants of α -synuclein fibrils: full length and C-terminus truncated. This chapter also introduces and describes the nearest neighbor measurement, where the center to center distance of the adjacent nanoparticles, decorating the amyloid fibril surface, is measured and analyzed. **Chapter 4** describes the analysis of the *in vitro* obtained polymorphic fibrils. The various morphology types of A β ₄₀ and R2 amyloid fibrils are reported and the periodicity analysis of the two-fold symmetric fibrils is performed and presented.

Chapter 5 is the continuation of the work done and presented in Chapter 4, but performed on more challenging samples. The first part of this chapter establishes that our gold nanoparticles label with success the *ex vivo* obtained samples allowing for a quick and robust analysis of the fibril morphology. The tests were done on the amyloids derived from the heart and the brain of human patients. The second part of this chapter describes the differences between the morphology of the *in vitro* and *ex vivo* obtained fibrils.

Chapter 6 focuses on investigating the challenges that could be encountered during the labeling of amyloids in complex samples, biological fluids and under various manipulations and conditions. We examine the stability of amyloid fibrils labelled with gold nanoparticles. We establish that this decoration is resistant to washing, dilution, sonication, addition of other biomolecules and significant pH changes. The second part of this chapter, describes the labelling efficiency in the presence of more complex solutions. We demonstrate that we are able to label amyloid fibrils in biologically crowded environments, such as cell debris and cerebrospinal fluid.

Chapter 7 provides the summary of all experimental results along with the perspective of future work. We propose that our gold nanoparticles can be used as a contrast agent in the liquid cell TEM measurements. This would allow the observations of amyloid fibrils aggregation kinetics and behavior in the solution. Due to their physical properties and different labelling efficiency of the various morphological types, gold nanoparticles can also be used as a separation tool for polymorphic species. That would be of immense help in the understanding of the properties, role and toxicity of the polymorphic type rather than average the effect of the whole amyloid population present in a sample. Finally, we propose that nanoparticles could be an important and an everyday use tool for studying challenging *ex vivo* derived amyloid fibrils and fibrils obtained *in vivo* without extensive purification and treatment.

Chapter 2

Introduction

All living organisms could be compared to complex machineries with thousands of processes carried out constantly at the same time. The human body is not an exception and at every second our cells, tissues and organs conduct numerous of intricate processes that are essential to life. All of this is confined in a delicate network of different elements among which proteins are the most prominent, by making up more than 50% of the dry weight of cells (39). The biological function of proteins is immensely diverse ranging from being elemental building blocks to sophisticated enzymes that are involved in many vital processes such as DNA replication. Among their other roles, proteins are responsible for transport, defense and storage. They also serve as chaperones in the process of folding of other proteins, which is a crucial step in the appropriate workflow of a healthy organism. Without the proper fold, proteins are losing their default conformation which affects their biological role. Moreover, multiple disease states, including many forms of dementia, are connected with the erroneous folding of these structures (39).

2.1 Protein misfolding and amyloids

The process of protein folding into their desired and functional conformation is affected by multiple factors, including the intrinsic property of the polypeptide chain and the complex cellular milieu. The number of possible conformations that a polypeptide chain can assume is enormous but the number of conformations that are physiologically desired is limited. The amino acid sequence already contains information about the folding, however it still has to meet thermodynamic and kinetic requirements to form the proper native state (40). Thermodynamic requirements assume that the natively folded protein has to be stable in the physiological conditions, while kinetic requirements post that the folding process, into the native state, has to be quicker than folding into aberrant conformation. The native states of the proteins almost always meet these requirements and on average the polypeptide chain finds its most thermodynamically stable structure (41). This process can be illustrated with the energy landscape of a funnel shape, which shows how the free energy of the polypeptide chain changes due to the conformation (Figure 2.1) (42).

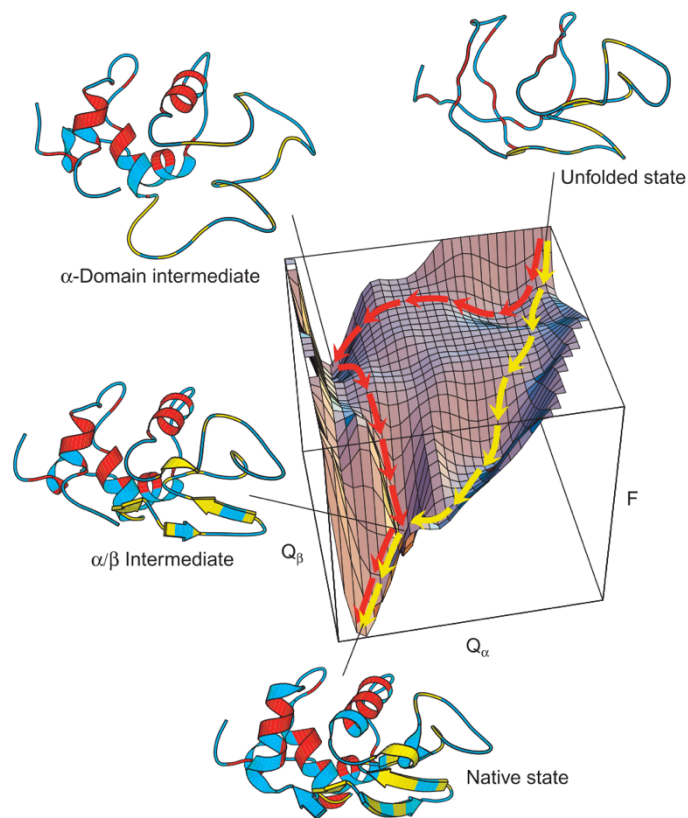


Figure 2.1 Schematic free-energy (F) surface representing two possible ways of folding of the protein that consists two domains: α and β . Q_α or Q_β is the number of native contacts in the α or β domain. The yellow arrows follow a faster “track” in which the α and β domains form at the same time resulting in the only one intermediate α/β . The red arrows follow a slow “track”, in which the intermediate with native contacts in the α domain is created first. In this case the protein assumes the native state after either a transition over a higher barrier or partial unfolding that would enable the remainder of the folding process to follow the faster “track”. Residues that are protected from solvent exchange in the native structure are colored red (α domain) or yellow (β domain), all others are blue. Reprinted with permission from (5).

During the folding process, the polypeptide chain becomes more compact by hiding the hydrophobic regions inside the protein and exposing the more polar side chains to the solvent (39, 43). This stage, called “molten globule”, is then interconverted into the native state by close packing of the side chains. The native state of the protein is attained and so is the most optimal balance between the free energy and entropy for a given sequence (43). To reach the default native conformation, the protein has to navigate through the free energy landscape and find the minimum energy conformer (44).

The environment can influence the protein conformation *in vitro* by changes in temperature, pH or addition of different solvents. *In vivo* conditions are not subjected to such

harsh changes; however, the cellular milieu is far more complex and crowded than *in vitro* environment. *In vivo*, some of the proteins start to fold while still attached to the ribosomes and other proteins are being folded in the cytoplasm or in the endoplasmic reticulum. This indicates that the folding process may somehow depend on the specific local cellular environment. Proteins synthesized in the cell very often reach their native conformation spontaneously, but some side reactions may limit the efficiency of the proper folding. This may require the assistance of chaperones or folding catalysts that assist this process (42).

Despite this quality control mechanism, the folding process is still error-prone due to the significant number of possible diverse conformations that can be assumed by the polypeptide chain. This bears the risk that beside natively folded protein species (on-pathway folding), aberrant fold may occur (off-pathway folding) (42, 45). Off-pathway folding can be induced

by (I) the mutations within the coding gene that results in the synthesis of a truncated protein or a protein with altered amino acid chain and thus folding properties, (II) defects in the translation and transcription processes, (III) errors in the assisting process that includes chaperones and catalysts, (IV) errors in the post-translational modifications and trafficking, (V) undesirable environmental changes or (VI) seeding of misfolded proteins (46). Proteins that failed the proper folding process or their fold is not stable, are recognized and targeted for degradation, but most frequently they tend to self-aggregate due to their exposed hydrophobic regions (42, 46).

As a result, several pathological conditions called *protein misfolding diseases* or *protein conformational diseases* may occur. These conditions stem from the insufficient amount of properly folded and functional proteins, wrong trafficking or the occurrence of the highly organized amyloid fibrillar aggregates (17).

Amyloid fibrils arise by self-assembly of misfolded proteins or peptides into β -sheet rich, ordered and elongated fibrillar structures (17). The process begins with misfolded monomers (proteins or peptides) that bind to each other, forming more complex assemblies until the structure of mature amyloid fibril is reached (47) (Figure 2.2).

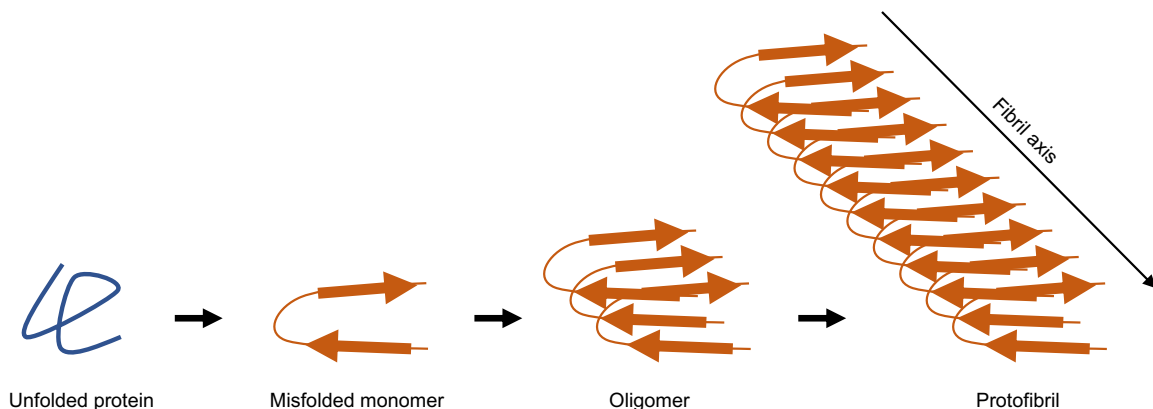


Figure 2.2 Schematic representation of amyloid fibril formation. β -sheet segments of each molecule in amyloid fibril are running across the fibril length.

The whole process can be explained by the hierarchical assembly model (HSA) that was proposed by Zanetti et al. (48) and then further explored by Khurana et al. (49). This model assumes that mature amyloid fibrils are formed by intertwined elongated precursors, driven by electrostatics and hydrophobic interactions. Fibrillation occurs when partially folded monomeric intermediates, driven by the hydrophobic force, interact with each other forming protofilaments. Subsequently, hydrophobicity drives protofilaments to interact with each other and intertwine to form protofibrils. Hydrophobic interactions between the protofibrils causes further intertwining of the elongated precursors, which results in the creation of a mature

amyloid fibril. The HSA model predicts visible periodicity of the amyloids due to the helical entanglement of the precursors. Figure 2.3 shows three proposed models of HSA that were derived for three different amyloid fibrils.

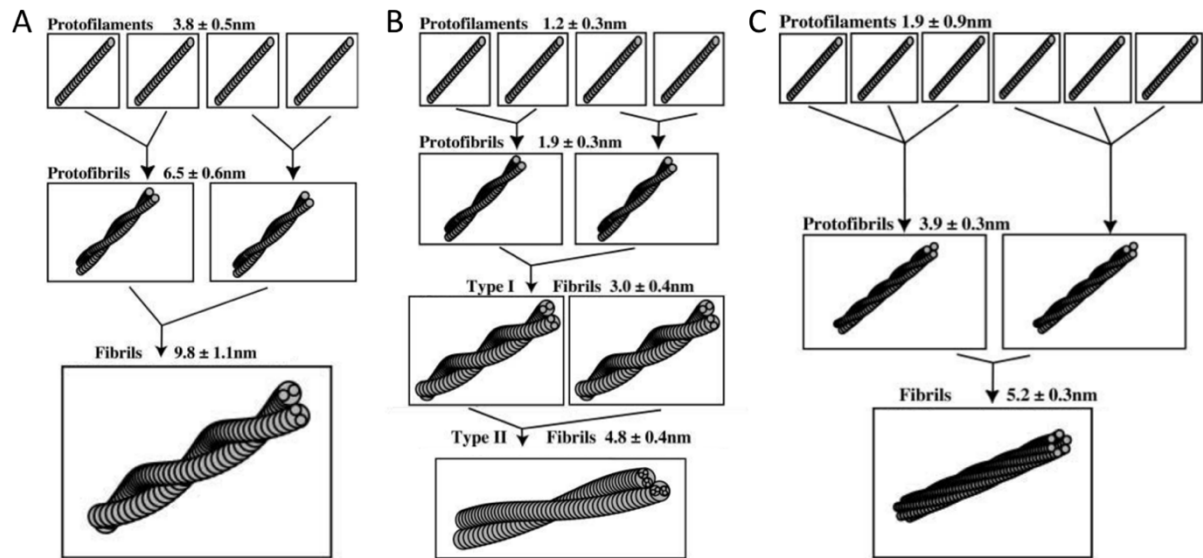


Figure 2.3 Three proposed models of HSA that were derived for three different amyloidogenic proteins. A) HSA model of α -synuclein where protofilaments pairs entangle together to form protofibrils, and consecutively two protofibrils intertwine to form a mature fibril. B) HSA model of insulin where two protofibrils entangle to form type I fibril. Two entangled type I fibrils result in type II fibril. C) HSA model of the B1 domain of protein G. Here, a protofibril is a result of three intertwined protofilaments, and mature amyloid is consisting two entangled protofibrils. Modified and reprinted with permission from (49).

The whole process of fibril formation can be kinetically described by nucleation-dependent polymerization model. This three-step process consists of (I) lag, (II) growth and (III) saturation phase. In the first step monomers start to nucleate forming bigger molecules such as oligomers. This rather long step is followed by the relatively short growth phase with rapid assembly of elongated structures such as protofilaments and protofibrils. The third step involves the entanglement of protofibrils into mature amyloids and slow saturation of the sample with fibrils. Rising amount of β -sheet as an effect of aggregation in time, resembles a characteristic “S” shape sigmoidal curve (Figure 2.4). The amount of β -sheet structures can be tracked with the use of a fluorescent dye such as Thioflavin T, which exhibit fluorescence upon binding to the β -sheet structures (20, 50).

Mature amyloid fibrils can induce further aggregation through fragmentation and seeded growth or secondary nucleation. In seeded growth aggregation, monomers are incorporated to the ends of the mature amyloids and the fragmentation of the fibrils increases the accessible surface that enhances the kinetics of the fibrillation. In this secondary nucleation process, the surface of a mature fiber serves as a nucleation site for new branching fibrils (37, 47, 51).

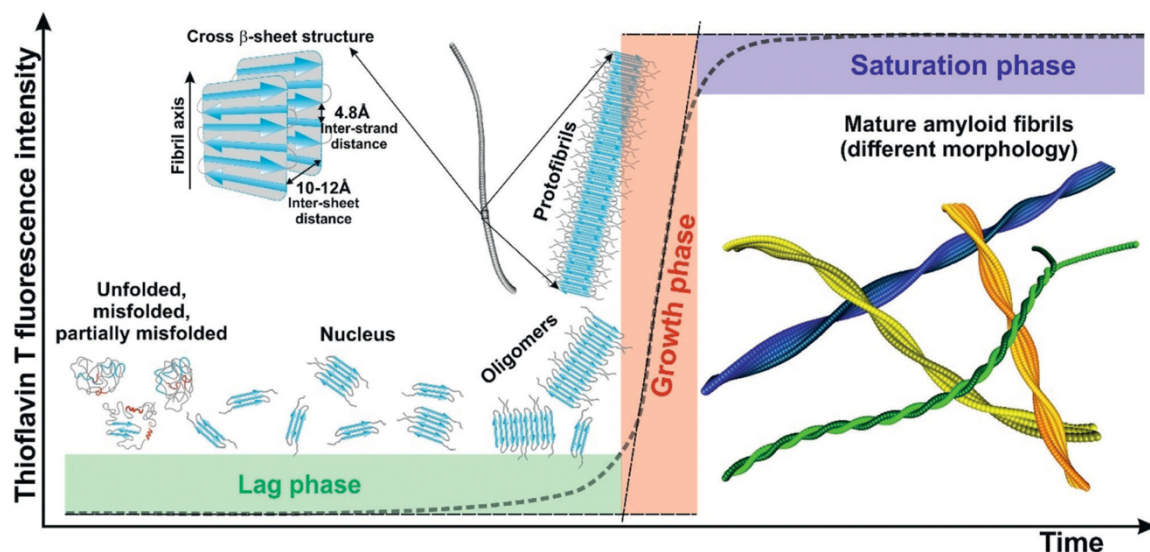


Figure 2.4 A schematic sigmoidal curve following the mature amyloid fibrils aggregation. The first (lag) phase contains the assembly of the non-natively folded polypeptide chains into bigger molecules such as oligomers where the presence of β – sheet starts to be detected by Thioflavin T dye. This phase is then followed by the growth phase, where bigger molecules assemble into intermediate elongated structures that rapidly grow and entangle to form protofibrils. The last phase involves the saturation of the sample with the maturing amyloids by assembly of protofibrils into mature amyloids. Reprinted with permission from (20).

A whole variety of proteins with a wide range in sizes, functions and structures can undergo this process. Despite these major differences, all amyloid fibrils share a number of similarities including the most prominent cross β motif in which β – strand segments lie perpendicular to the fibril axis separated by 4.6-4.8 Å. Fibrils are typically 5–15 nm wide or associate laterally to form long ribbons that are 2–5 nm thick, up to 30 nm wide and can be micrometers long. The most characteristic amyloid feature is the twisted morphology due to the twisting along the fibril axis (17, 21). Amyloids are fundamentally different than their native conformations. In the native state, intramolecular interactions dominate, whereas in the case for amyloid fibrils intermolecular interactions are more prominent (20). Off-pathway folding that results in the formation of amyloids, can be also illustrated with the use of a funnel shaped energy landscape but since the intermolecular interactions dominate and compete with the intramolecular interactions, the ruggedness of the landscape is pronounced. Amyloid fibrils are the most thermodynamically stable state of all the possible polypeptide chain assemblies with the lowest free energy. However, the natively folded protein still has to overcome the energy barrier to assume this state (Figure 2.5) (18, 20, 52).

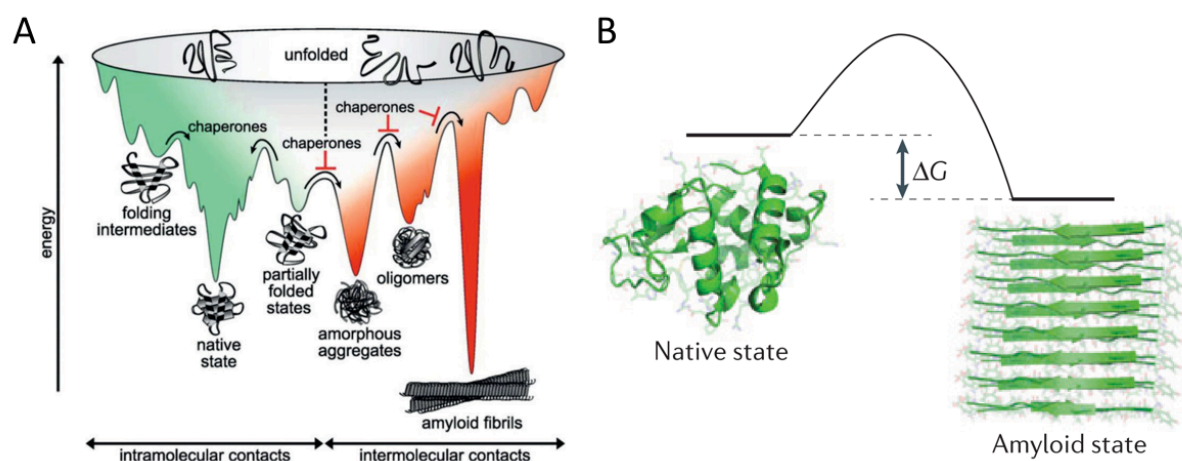


Figure 2.5 Thermodynamic stability of the fibrils. The interactions between amino acid residues that dominate in the native state of a protein are intramolecular, whereas in the amyloid state are intermolecular. A) The energy landscape of native protein folding (green) and aggregation (red). During folding toward the native state, native protein folding and aggregation are competing. Polypeptide molecules undergo various conformations driven by intramolecular interactions traveling downhill on a potential free-energy surface (green part) towards the thermodynamically favorable native state. Kinetically trapped on- or off-pathway intermediates and partially folded states occupy low-energy wells. The kinetically trapped off-pathway intermediates have a tendency to establish intermolecular interactions (red part), which results in the assembly of various aggregates such as amorphous aggregates, β -sheet rich oligomers and amyloid fibrils, which have been postulated as the thermodynamically most stable. Molecular chaperones provide folding assistance by lowering free-energy barriers and by inhibiting intermolecular interactions and promoting folding into the native conformation. Reprinted with permission from (45). B) As a protein will not spontaneously transition from a state of lower free energy to a state of higher free energy, the conversion into the amyloid state will only take place when its free energy is lower than that of the native state. At some conditions (e.g. high concentration of the protein) polypeptide is more stable in the amyloid state than in its native state. In such situations, the native state can only persist if there are high free energy barriers that hinder the transition into the more stable amyloid state. Reprinted with permission from (18).

The presence of functional amyloids, which are amyloids serving several purposes to living organisms (17, 53), has been previously reported, however occurrence of such structures is mostly connected with a pathological state (17).

2.1.1 Amyloids and human diseases

Proteins and peptides in the amyloid state are found in approximately 50 diseases that include both systemic or localized amyloidosis and neurodegenerative conditions spanning from motor neuron disorders to several types of dementia (17–19, 54, 55). Table 1 covers the disorders that are associated with proteins and peptides mentioned in this thesis. They are grouped in three classes based on the types of the affected tissues: (I) neurodegenerative disorders, (II) non-neuropathic systemic amyloidosis and (III) non-neuropathic localized amyloidosis. The first group of disorders is characterized by the aggregation taking place only in the brain, the second one manifests aggregates in multiple types of tissues and the third one displays amyloids in only one type of tissue (17). The table also includes some properties of the disease precursors such as the number of amino acids in the polypeptide chain and their desired on-pathway structure.

Table 1 Examples of amyloid diseases with their associated precursors (17).

Disease	Precursor protein or peptide	Precursor properties – number of amino acids and native fold
<i>Neurodegenerative diseases</i>		
Alzheimer's disease (AD)	Amyloid- β peptide (A β)	40 or 42; unfolded
Parkinson's disease (PD)	α -synuclein (α -syn)	140; unfolded
Dementia with Lewy bodies	α -synuclein	140; unfolded
Huntington's disease (HD)	Huntingtin with polyQ expansion	3 144; polyQ containing region is largely unstructured
Frontotemporal dementia with Parkinsonism	tau	352-441; unfolded
<i>Non-neuropathic systemic amyloidosis</i>		
AL amyloidosis	Immunoglobulin light chains or fragments	~ 90; all β -structure
Senile systemic amyloidosis	Wild type transthyretin	127; all β -structure
Familial amyloidotic polyneuropathy	Mutant transthyretin	127; all β -structure
<i>Non-neuropathic localized diseases</i>		
Inclusion-body myositis	Amyloid- β peptide (A β)	40 or 42; unfolded

The very broad group of neurodegenerative disorders ranges from motor disorders to dementia, which is mostly caused by Alzheimer's disease (AD). It is usually diagnosed by confirming the existence of extracellular plaques that consist of amyloid- β peptide (A β), accumulation of hyperphosphorylated protein tau inside the cell body (known as neurofibrillary tangles NFT) and by monitoring the synaptic degeneration. AD is predominantly an age-related disease affecting people above 60-65 years of life, however several mutations that cause early onset of this disorder have been identified. These mutations were linked to pathways and mechanisms that regulate the production of amyloid- β peptide and their aggregation and clearance (56, 57). AD is characterized with the impairment of the cognitive functions and personality changes (56, 58). The second most common illness in this group is Parkinson's disease (PD). PD is classified as a movement disorder due to the bradykinesia, which is one of PD's major symptoms. The clinical syndrome of Parkinson's disease is linked with neuronal loss in the *substantia nigra* and inclusions of α -synuclein (α -syn) protein in the remaining neurons. These

inclusions are known as Lewy bodies or Lewy neurites. α -syn aggregation is also connected to other neurodegenerative disorders such as dementia with Lewy bodies. As in the case of AD, disorders connected with α -syn aggregation are mostly age related, however there are known mutations responsible for the early onset of the disease (59, 60). In comparison with AD or PD, Huntington's disease (HD) is purely monogenetic disease that is caused by a CAG expansion, which translates into polyQ repeats in exon1 of the gene that codes for the huntingtin protein. HD is an autosomal-dominant disorder, which affects mostly motor functions with chorea, dystonia and incoordination. It also affects cognitive functions and causes behavioral problems. The onset of HD is inversely correlated with the number of glutamine (Q) residues in the polyQ region of huntingtin protein. The number of repeats vary between individuals and the higher the number of Q is, the lower is the age of onset with the cutoff between normal and pathogenic repeat lengths around 36 glutamines. Furthermore, there is a direct correlation between the number of polyQ and the aggregation propensity of huntingtin proteins, with the rates of aggregation increasing with increasing length of the polyQ repeat. From a histological point of view, HD is characterized by the presence of neuronal intranuclear and perinuclear inclusions consisting of huntingtin amyloids derived from N-terminal fragments of the protein (6).

The most common condition from the second group of amyloid related disorders is systemic light chain amyloidosis (AL amyloidosis), where the precursor protein is a monoclonal immunoglobulin light chain. The extracellular amyloid deposits are found mostly in the hearts, kidneys and livers of patients, however neuropathies are also frequently noticed. The large deposits of aggregates cause devastating organ damage and failure leading to death. Another protein linked with the non-neuropathic systemic amyloidosis is transthyretin (ATTR) involved in the development of wild type transthyretin amyloidosis or senile systemic amyloidosis. In the case of these diseases, the deposition of amyloids can be hereditary or linked with the ageing process (33, 61).

Amyloid- β has been implicated not only to neurodegenerative conditions, but also to non-neuropathic localized amyloidosis by being involved in the inclusion body myositis. In this case amyloid deposits are found intracellularly in the muscle fibers causing muscle weakness. Inclusion body myositis can be hereditary or sporadic (62).

Currently, detection of amyloid plaques, present in the organs of patients suffering from systemic amyloidosis, strongly relies on the biopsy. This allows for the histopathologic examination of amyloid deposits with the use of the specific dyes such as Congo Red (63, 64). The first step confirming the presence of amyloid deposits is followed by additional examination in order to identify the correct amyloid type. This is performed, most often, via immunochemistry, however there is a number of other techniques that can be applied, such as mass spectrometry (65). Amyloid plaques related with dementia are more challenging to detect. Limited access to the brain tissue hinders histological examinations, thus clinical diagnosis of such diseases rely mostly on the observation of specific symptoms (66). The diagnosis can be further supported with the use of brain imaging techniques, for example Positron Emission Tomography (PET) tracers or Magnetic Resonance Imaging (MRI) (66, 67). The level of the amyloidogenic proteins can be also monitored in the cerebrospinal fluid (CSF), which can also contribute to the diagnosis of the patient (68). Moreover, hereditary amyloid related disorders can be detected by genetic testing, which identifies the mutations connected with the development of amyloid diseases (63).

Despite the strong evidence pointing to a link between protein misfolding and amyloid formation to the amyloid diseases mentioned above, the role of the amyloid fibrils or the process of amyloid formation in the pathogenesis of these diseases is still not fully understood. Furthermore, elucidating the mechanism of toxicity and identification of the toxic entities remain subject of intense activity and discussion. *In vitro* aggregation studies enabled the identification of several pre amyloid oligomeric species that exist in a variety of arrangements (e.g. soluble oligomers, dense plaques or intracellular aggregates). Subsequent studies showed that many of these oligomeric species are more toxic to different types of cells and neurons, compared to the mature fibrils (69). This has led some studies to suggest that forming amyloid aggregates may be in fact a protective response on higher levels of potentially toxic misfolded protein species. Ongoing debate about the toxicity of amyloids versus oligomers remain unresolved (12, 70). The presence of amyloids in the brains of the non-symptomatic patients, have been used as the basis for arguing that the mature amyloid fibrils are less likely to be the cause of the disease (21, 71). However, this discrepancy can be also explained by the remarkable polymorphism of the amyloid fibrils and/or the fact that toxicity may arise from the activity of prefibrillar intermediates which are not detected by the conventional Positron Emission Tomography (PET) tools used to quantify amyloid.

2.1.2 Amyloid polymorphism and strains

Despite the fact that all amyloid share a common cross- β structure, several studies on different amyloid-forming proteins have shown that amyloid fibrils exhibit large variety of morphological types e.g. straight or twisted fibrils (21). These differences in morphology are commonly referred to amyloid polymorphism and are associated with differences in fibril mechanical properties or speed of propagation (72, 73). Moreover, various fibril polymorphic types derived from the same protein show different levels of toxicity on the cell cultures (27, 74) and propagation properties *in vivo* (75). This, if extrapolated on human tissue, could shed a light on the molecular basis of the clinical heterogeneity of the disease (35).

Polymorphism of the amyloid fibrils was first noticed by Cohen A. and Calkins E. already in 1959 (76). A more detailed description of the differences in fibril morphology was presented in the following work published in 1965, where Cohen and Shirahama presented their TEM investigation performed on human samples. Their results showed, that amyloids derived from the patients, suffering from amyloidosis, exhibit some differences in their dimensions (77).

Amyloid polymorphism can occur at different levels. Previous studies have established that the same protein can assemble into distinct molecular arrangements when forming an amyloid fibril, and in this thesis, we refer to this as “molecular polymorphism” (21, 32, 38). Other studies report, that the shape, e.g., the symmetry and thickness of a fibril, varies depending on the number of protofilaments that compose the fibril and their arrangement (20, 49, 78). Furthermore, in this thesis we focus only on this type of polymorphism and refer to it as “morphological polymorphism”. These two types of polymorphism are not mutually exclusive and could coexist (Figure 2.6).

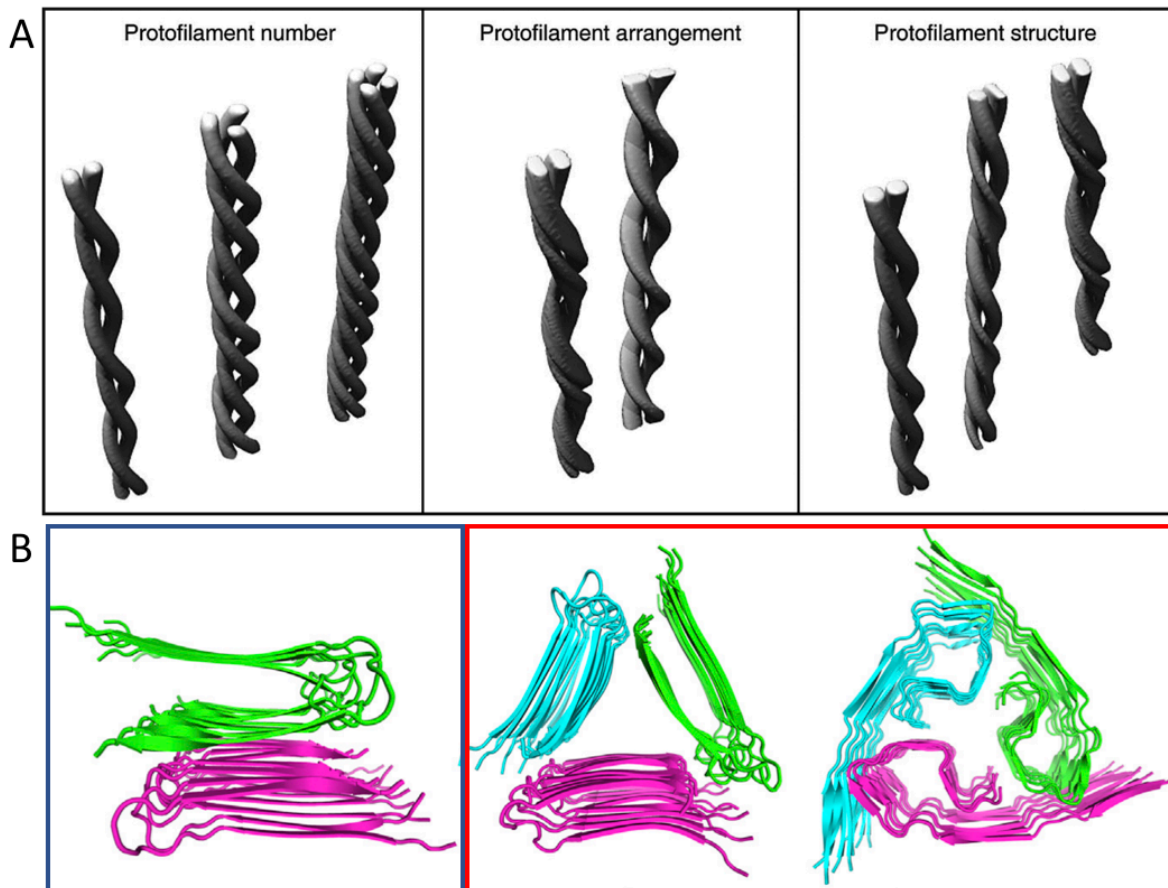


Figure 2.6 Cartoons representing different levels of amyloid polymorphism. A) different fibril morphologies that stem from different number of protofilaments, different arrangements or different structure of the protofilaments. Reprinted with permission from (79). B) Cartoon representations of A β ₄₀ polymorphic fibrils that originate from the various folding of the monomers. The blue-colored panel illustrates the cross section of the two-fold symmetric fibril and panel in the red box shows cross sections of the two types of three-fold symmetric fibrils with differently folded monomers. Reprinted and modified with permission from (21).

The most common and typical morphology of amyloids are straight or twisted fibrils, however more complex morphologies such as nanotubes, helical ribbons, crystals or three-fold symmetry fibrils are reported (20, 25). Several studies have shown that the specific morphology type can be obtained by modification of the amyloid fibrils' growth conditions such as shaking, temperature or ionic strength of the buffer (26, 74, 80). The external growth conditions may also affect the pitch length of the twisted fibrils (25–29). However, the development of the specific polymorphs is more complex and difficult to control. It was found that even in the same sample, different types of fibril polymorphs can form and coexist, which suggests that they are either in an equilibrium or are derived from morphologically distinct intermediates on the pathway to aggregation (30, 31). The polymorphism of cross- β fibrils has also been observed in *ex vivo* amyloids, for instance isolated tau fibrils from the brain of patients with AD (32) or amyloid fibrils from patients and animals with systemic amyloidosis of amyloid A (AA), transthyretin and light chain (33).

The existence of the various morphologies of the amyloid fibrils, raises additional questions about their thermodynamic stability. The plethora of possible arrangements of the polypeptide chain and interactions between the amyloidogenic intermediates results in many possible variants of amyloid fibrils. This makes the funnel-shaped energy landscape of a folding protein even more rugged. The well of lowest energy that contains amyloidogenic species can be even further expanded and divided into additional “sub-wells” since various polymorphic fibrils differ from each other regarding in their energy level. It was found that among them, the crystal form occupies the “sub-well” of the lowest energy (Figure 2.7).

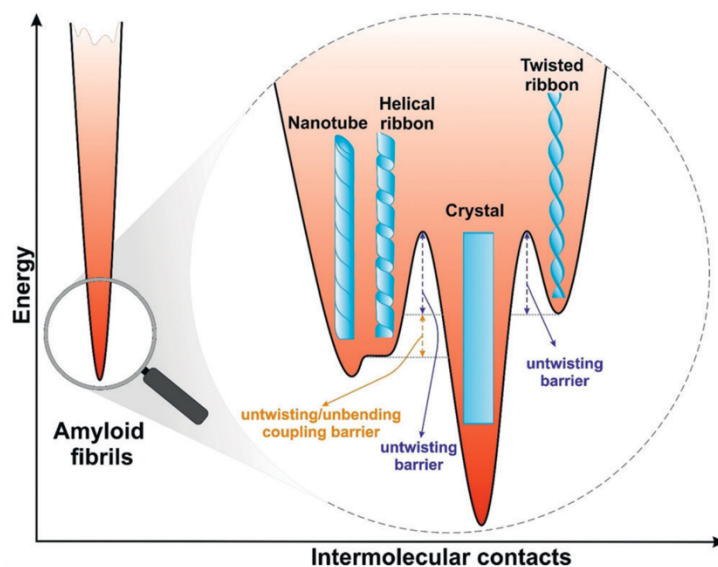


Figure 2.7 Zoom on the lowest energy well with the amyloid species that illustrates differences in the energy level between the polymorphs, where the crystal form occupy the well of the absolute minimum. Reprinted with permission from (20).

The existence of the different morphological types is of great biological relevance. It is established that conformational variations of some prion proteins result in different incubation time or symptoms of the disease (21). These different structural variants of the infectious protein are called strains and the same behavior has been observed for the polymorphic amyloid fibrils. Recent studies have

demonstrated that introducing recombinant preformed fibrils or amyloid aggregates derived from diseased postmortem brain tissues into neurons or directly into rodent brain is sufficient to induce disease-like pathology formation and spreading. In these seeding-based models, distinct fibrillar polymorphs lead to different patterns of pathology spreading and/or toxicity (59, 81–83). The correlation between the amyloid fibril polymorphism, toxicity and symptomatology was observed for A β fibrils (35, 36) and Peng et al. (82) demonstrated similar behavior of α -synuclein. In their study, cytoplasmic brain aggregates containing α -synuclein from patients with different types of synucleinopathies: Parkinson’s disease and multiple system atrophy, exhibited different conformations and seeding capacities. Similar observations were made for tau protein (84). These findings and the availability of cellular and animal models of amyloid propagation provide a unique opportunity to investigate the relationship

between amyloid molecular and morphological polymorphism, neurodegeneration and pathology spreading in neurodegenerative diseases. Nonetheless, it remains challenging to elucidate the structural basis and role of fibril polymorphism in human-derived material due to the minute amount of these aggregates and the complexity of the samples.

2.1.3 Techniques used for studying amyloid fibrils

There are many various approaches to investigate amyloid polymorphism and understand its connection with disease development. Table 2 shows selected techniques that are commonly used in amyloid studies with a short description of the advantages and limitations of each. Table 3 focuses especially on the microscopy techniques.

Table 2 Selection of the techniques used for probing amyloid fibrils, that are also successfully applied in the polymorphism studies.

Technique	Short description and observed features	Disadvantages
ssNMR (85)	Spectroscopic technique based on the ability of nuclei to absorb and re-emit electromagnetic radiation in a magnetic field. Allows to analyze atomic contacts, which enables fibril structure reconstruction.	Isotope enrichment (^{13}C , ^{15}N) necessary. Does not enable distinctions of polymorphisms in the same sample. Problematic for big molecules.
X ray diffraction (86)	A structural analysis technique that is based on the diffraction angles and intensities of X rays that scatter from the studied sample. Used for structure examination, such as parallel or antiparallel arrangement and stacking of β -sheets and side chain packing.	Requires high concentrations of well-aligned fibrils.
ThT assay (16)	Thioflavin T is a dye which exhibits enhanced fluorescence upon binding to mature fibrils. Enables monitoring amyloid formation and investigation of fibrillation kinetics.	Does not provide insight into morphology and detailed structure of the fibrils.
Circular Dichroism (86)	Light absorption spectroscopy technique that measures the absorbance of the substance of polarized light as a function of the wavelength. Used for assessing presence and abundance of the β -sheet structure.	Possible interference from the aromatic residues. Lack of insight into morphology.
SDD-AGE (87)	Technique allowing to differentiate amyloids with different molecular weight by using migration through agarose gel. Allows for differentiation of the amyloids due to their size.	Impossible insight into morphology and molecular structure. Requires complementation by western blot.

Table 3 List of the microscopy techniques used for visualization and characterization of amyloid fibrils in this study.

Technique	Short description and observed features	Disadvantages
High resolution fluorescence microscopy (dSTORM) (88)	Imaging technique that visualizes fluorescence of the analyzed material. Used for morphology and kinetics of amyloid formation visualization.	Requires labelling with fluorophores. Low resolution in comparison to other microscopy techniques.
AFM (37)	Scanning technique which uses oscillating tip that probes the surface and reads the forces between tip and surface. Allows to probe morphology, mechanical properties of fibrils and aggregation kinetics.	Does not provide insight into structural details of the fibrils, such as protein fold, possible surface influences on the amyloid aggregation and presence of tip convolution.
<i>Transmission electron microscopy techniques</i>		
Negative staining (89)	Electron heavy stain is used to add contrast to otherwise not visible in TEM organic structures. Enables observation of the morphology of the fibrils.	Possible drying and surface artefacts, lack of structural insight.
Cryo TEM (90)	Sample is frozen in thin layer of vitreous ice. Used for high resolution visualization of the fibrils and morphology studies.	Weak contrast, laborious, requires extensive data analysis.
Immunogold (91)	Application of gold nanoparticles with attached antibody. Allows the recognition of protein domains.	Requires the use of bulky antibody, possible false positives.

Molecular polymorphism has been investigated using solid-state NMR (ssNMR) spectroscopy, microcrystallography and X-ray diffraction, while transmission electron microscopy (TEM), scanning probe microscopy and atomic force microscopy (AFM) have been used to investigate morphological polymorphism (52, 92). These techniques have similar limitations: they (I) are time consuming; (II) require large amounts of protein (e.g., ssNMR); (III) can be applied only to small amyloid-forming peptides (e.g., microcrystallography); (IV) do not allow imaging of amyloids in complex systems under native and hydrated conditions (e.g., TEM); or (V) require the presence of a substrate that may strongly influence the aggregation pathway of the growing fibrils (e.g., AFM) (93). ssNMR allows to observe the atomic contacts which enable fibril structure reconstruction. However, the enrichment with an isotope (^{13}C , ^{15}N) is necessary and on top of that, ssNMR is a bulk technique that does not enable distinctions of polymorphisms in the same sample and may be problematic for big molecules. For example, direct investigation of the molecular basis of amyloid polymorphism of A β in AD brain tissue using

ssNMR spectroscopy was only possible by seeding brain-derived aggregates (seeds) to an excess of isotopically labeled monomeric proteins, yielding hundreds of milligrams of fibrils (22, 74, 94). AFM allows morphology observation, measurement of the mechanical properties of fibrils and following of the aggregation kinetics. However, the insight into structural details of the fibrils is not possible, and tip convolution may introduce artefacts or affect the final image of the sample. In TEM, samples are dried on the grid and stained with an electron-dense staining agent before imaging. Although this technique allows for rapid characterization of the structural morphology of the fibrils (33), it may introduce several artifacts, such as flattening of the structure or incomplete stain embedding (95).

Cryo TEM can address these shortcomings because it does not require drying, staining or surface deposition and allows fibrils to be imaged in their hydrated state. In this method, thermal fixation is applied, therefore the visualization of the frozen sample in a thin film of vitrified solvent is enabled (Figure 2.8).

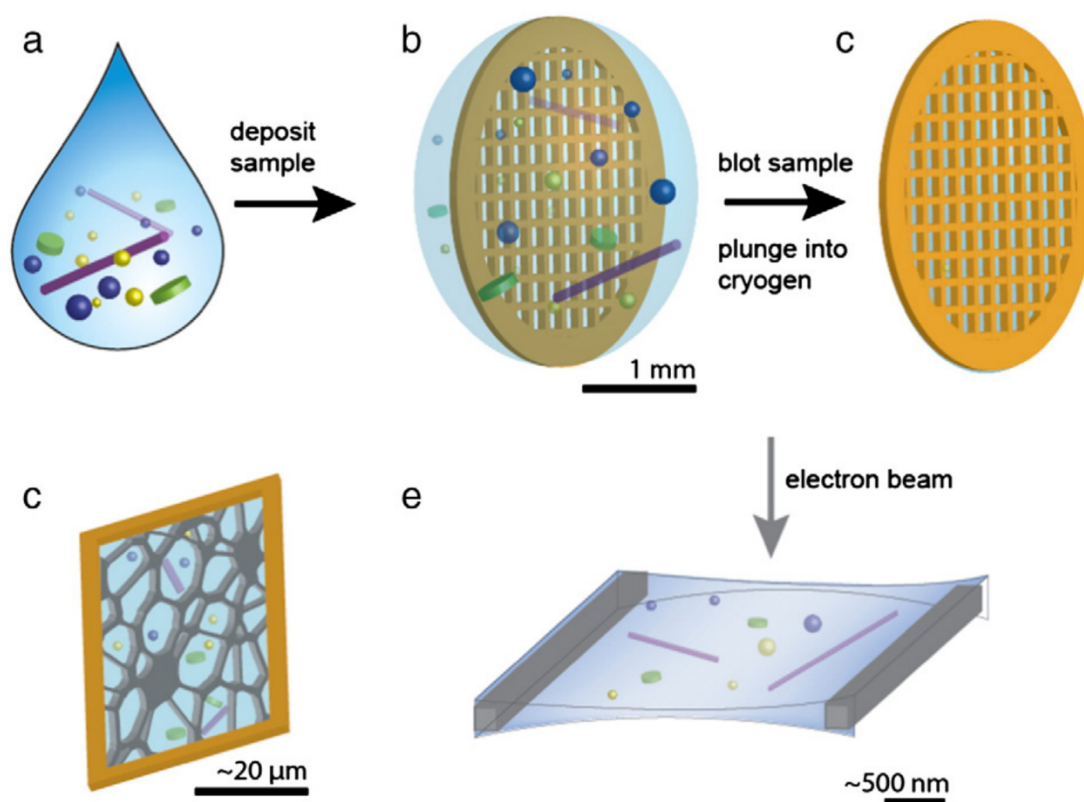


Figure 2.8 Schematic representation of the sample preparation for cryo TEM measurements. a) the sample is suspended in the solution, b) deposition of the sample onto a specific grid, c) blotting of the solution in order to remove excess liquid and quick immerse into a cryogen, typically liquid ethane, d) the representation of the frozen film of the solution with sample suspended on the carbon support, e) thin layer of the solution imaged with the electron beam. Reprinted with permission from (96).

Several different structures such as vesicles, micelles, viruses or proteins were observed with this technique (96). Cryo TEM is increasingly used to investigate the structure of amyloid fibrils prepared *in vitro* or derived from different tissues (30, 32, 97). However, the

measurements are based on the weak contrast between fibrils and glassy ice, which require careful acquisition and advanced data analysis to extract morphological information. Moreover, because of the electron beam, sample is exposed to radiation damage. Additionally, sample preparation and sample-electron interactions can introduce some artefacts in the final image (96). In this thesis we show that gold nanoparticles synthesized in our group combined with the Cryo TEM technique can address these limitations allowing for the rapid screening and detailed characterization of amyloid morphological polymorphism under hydrated conditions.

2.2 Nanoparticles

Gold nanoparticles are known in human history since ancient times when they were, and still are, used as a pigment to dye glass of ruby color (98). Since then, the use of nanoparticles improved greatly and their unique properties have opened new opportunities for many industrial branches. Their use spans from solar cell technology to cosmetology, where they serve for example as UV protection filters (99). Their numerous desirable properties stem from their size and tunability. Nanoparticles can be composed of polymers, carbon, silicates or consist of an inorganic core (typically noble metal or metal oxide) that is surrounded by a monolayer of organic molecules called ligands. The shape of the core can be spherical or non-spherical and exhibit various shapes such as rod, cube, shell, triangle or even star of sizes ranging from 1 to 100 nm. The surface of the nanomaterial can be functionalized, which introduces further properties such as charge, solubility or affinity to other structures (100) (Figure 2.9).

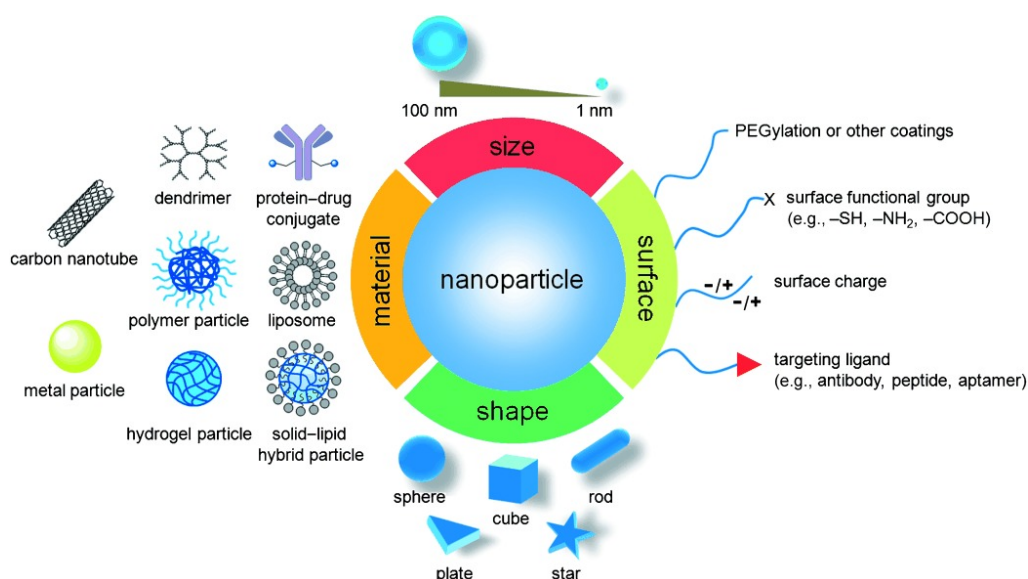


Figure 2.9 A cartoon schematically illustrating the various types of nanomaterials with their broad possible alternations including building substance, shape, size and surface functionalization. Reprinted with permission from (101).

Nanoparticles (NPs) are an intermediate state between bulk material and individual atoms or molecules. In comparison with the bulk material, a substance in the form of nanoparticle changes some of its properties e.g. increase of the surface, antimicrobial properties or hardness (99). These characteristics make nanomaterials a very flexible tool of immense amount of possible applications that include biosciences and medicine, which opens a new research area: nanomedicine (101).

2.2.1 Nanoparticles in biosciences

The application of nanomaterials in biosciences merges two big branches of research – biology and materials science. The interest in this relatively new research field is rapidly growing resulting in the constant introduction of novel solutions and tools in the biosciences. The most common application of nanoparticles in this field are fluorescent labels, drug and gene delivery, biosensing, bioimaging for *in vivo* studies or biomaterial compounds (102, 103). In the past two decades, the number of commercially available nanotechnology-based therapeutics significantly increased and several nanotechnology based products were approved for clinical use (104). Commercial applications of nanoparticles in biotechnology span from toothpaste and surface disinfectants to drug delivery technologies that are able to pass the blood-brain barrier (105). Besides that, nanoparticles can be potentially used in antibacterial creams and powders, bone growth promoters or biocompatible coatings (106).

Nanoscale materials are also increasingly used in neuroscience. For example, nanotubes and nanofibers can be used as cell growth promoting scaffolds to repair neuronal damage after stroke or spinal cord trauma. Nanomaterials can also be neuroprotective, as studies have shown that they can provide protection from reactive oxygen species in the brain by endowing them with antioxidant properties (107). Moreover, nanoparticles can be designed to cross the blood brain barrier, which normally blocks the access of drugs to the central nervous system. In this case nanoparticles can be considered as a vector to transport therapeutic agents to the brain (108). Among other neurobiologically related topics, a significant number of studies with use of nanomaterials was performed strictly on amyloids.

2.2.2 Nanoparticles in amyloid studies

The influence of nanoparticles on the protein misfolding and amyloid assembly process was tested and reported by numerous researchers. The possibility of controlling the aggregation process via nanoparticles that could play the role of artificial chaperones is very interesting and from the available results, two opposing mechanisms have been proposed. Nanoparticles may

change the monomer conformation upon binding or increase the local concentration of the protein in the vicinity of the nanoparticle surface promoting aggregation. On the other hand, the off-pathway intermediates could be trapped on the nanoparticle surface which may inhibit further amyloid formation (109). It was found, that depending on the core material, nanoparticles can either promote or inhibit amyloid growth. For example, TiO₂ nanoparticles triggered the formation of A β ₄₂ fibrils, possibly due to the absorption of A β ₄₂ monomers onto the particle surface. This increased the local concentration of monomers enhanced fibrillation. In the same study, nanoparticles made from other substances did not affect fibrillation, which demonstrates the importance of the material composition (110). Linse et al. found that fibrillation of β ₂-microglobulin can be promoted by nanoparticles made from N-isopropylacrylamide (NIPAM) and N-tert-butylacrylamide (BAM). Nanoparticles of 70 nm and 200 nm core diameter were incubated with protein monomers causing faster fibrillation. In this study, the ratio between NIPAM and BAM had more significant effect on promoting fibrillation than nanoparticle size (111). Later, it was discovered that the same nanomaterial is able to inhibit fibrillation of A β ₄₀. As in previous cases, material composition was crucial. There was a correlation between NIPAM/BAM ratio and rate of fibrillation, which was slower with increased content of NIPAM (112). Aggregation of A β ₄₀ can be also inhibited by negatively charged and bare gold nanoparticles. Moreover, a decrease in ThT intensity was observed after adding the nanomaterial to the mature fibrils, which can suggest precipitation of the material (113). Studies reporting both inhibiting and accelerating effect of nanomaterials of various compositions on amyloid formation were also performed on different proteins such as α -synuclein, human serum album or insulin (114). Interesting studies were performed by Kim et al., on the influence of the size, charge and shape of the gold nanoparticles on the aggregation of A β peptide. It was found that the size of nanomaterial plays a crucial role in amyloid aggregation and among three sizes of gold nanoparticles (20 nm, 50 nm and 80 nm diameter size), nanoparticles of larger sizes significantly accelerated growth of A β on the brain lipid extract-based supported lipid bilayer. The same studies showed that negatively charged gold nanoparticles formed larger aggregates of A β than gold nanoparticles of the same size with positive charge. Lastly, among three shapes tested-rods, spheres and cubes, nanocubes were forming larger aggregates of A β peptide (115). The size effect on A β ₄₀ formation was also found for L-glutathione stabilized gold nanoparticles, where nanoparticles of diameter 18 nm and higher, were accelerating growth of amyloid fibrils, while nanoparticles of diameter 6 nm inhibited this process. Interestingly, in the same studies, nanocubes stabilized with L-

glutathione were having inhibitory effect on the A β ₄₀ fibrillation, and even completely blocked it at higher concentrations (116). The above studies concluded that controlling the aggregation process with the use of nanoparticles is very intricate and strongly depends on nanomaterial, protein properties and solution conditions.

Aside from the aggregation process, nanoparticles can also influence mature amyloid fibrils. For example, upon addition to mature A β ₄₀ fibrils, bare gold nanoparticles with a diameter size of 30 nm changed their morphology from smooth to ragged (113). According to studies, nanomaterials can also serve as a potential tool for aggregates destruction, for example by photothermal ablation with gold nanoparticles or penetration and extraction of peptides from preformed fibrils by graphene nanosheets (117, 118).

Another creative application of nanomaterials in amyloid studies is the separation and removal of amyloid fibrils from a solution with use of, for example, magnetic nanoparticles (119–121). Nanomaterials were also successfully used as a marker for imaging of amyloid plaques in the brain with the use of magnetic resonance imaging (122), however the same procedure for imaging of the morphology of a single fibril has been proven slightly challenging.

In 1971 Faulk and Tylor developed an immunocolloid method for imaging in electron microscopy (91). An antibody can be attached to a gold nanoparticle that will co-localize with the target-antigens in a tissue section allowing for ultrastructural localization of proteins and organelles. Immunogold is still commonly used in biology and has been beneficial in amyloid research (123). But despite offering a detailed view of biomolecules, immunogold labelling has a few limitations. For example, due to the use of the antigen-binding fragment (Fab), the gold nanoparticle can anchor only as close as 7 nm away from the place of interest due to the antibody size to which the gold nanoparticle is attached. This distance can increase with the use of an indirect labelling system which requires primary and secondary antibodies bound to each other. In this system the primary antibody attaches to the place of interest and the secondary antibody is carrying the gold nanoparticle (Figure 2.10) (124).

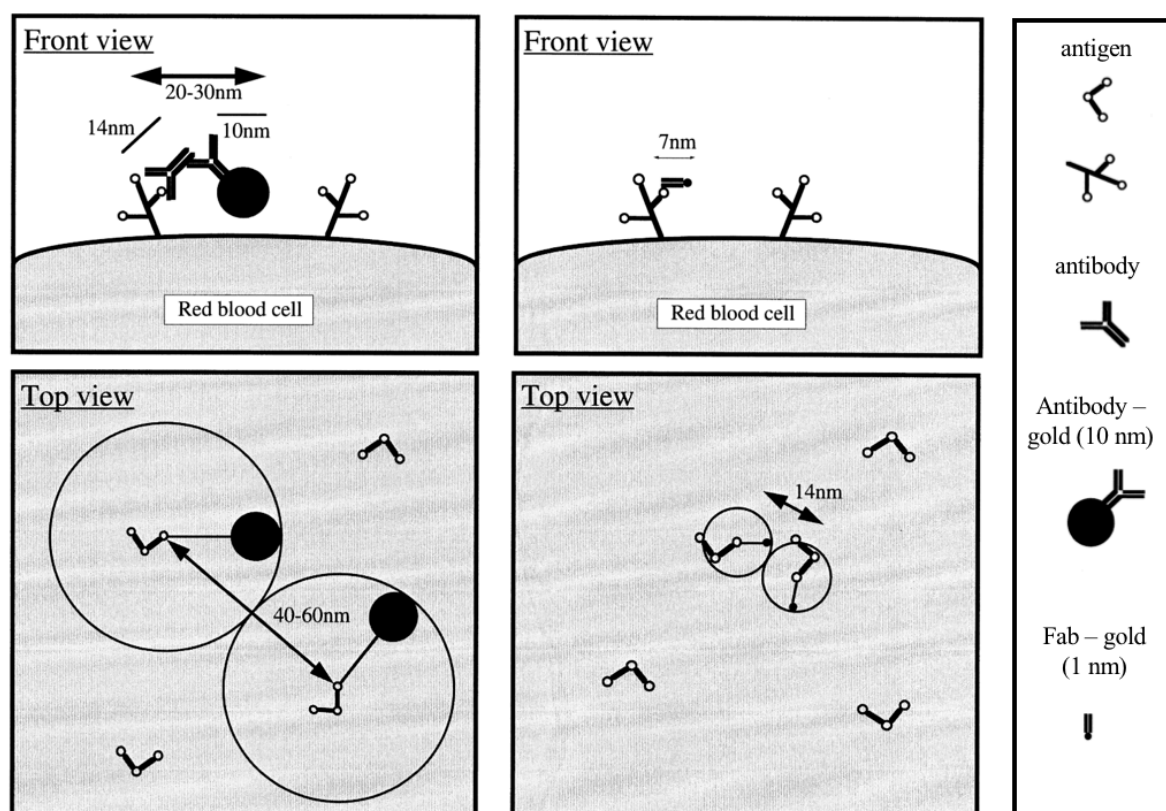


Figure 2.10 Scheme of indirect (left panel) and direct (middle panel) immunogold labelling with colloidal gold. The red blood cell is presented as an example. Indirect labelling requires two antibodies that can place the gold 15-30 nm away from the antigenic sites. The direct labelling allows for the placing the small colloidal gold 7 nm away from the target. Reprinted and modified with permission from (124).

Incorrect antibody handling can lead to nonspecific binding, false positives or absence of labeling (125). Furthermore, the interactions between gold nanoparticles and proteins are not fully understood: this means that non-specific interactions in the use of immunogold remain largely unexplained.

There are also examples of amyloids being labeled using a nanomaterial without spacers, such as maghemite NPs (120, 121), gold nanorods (126) or gold NPs (113, 127). Due to their bulky size and the nonspecific nature of their interactions with amyloid fibrils, these nanomaterials are also unsuitable for unravelling morphological features and heterogeneity of fibrils (Figure 2.11).

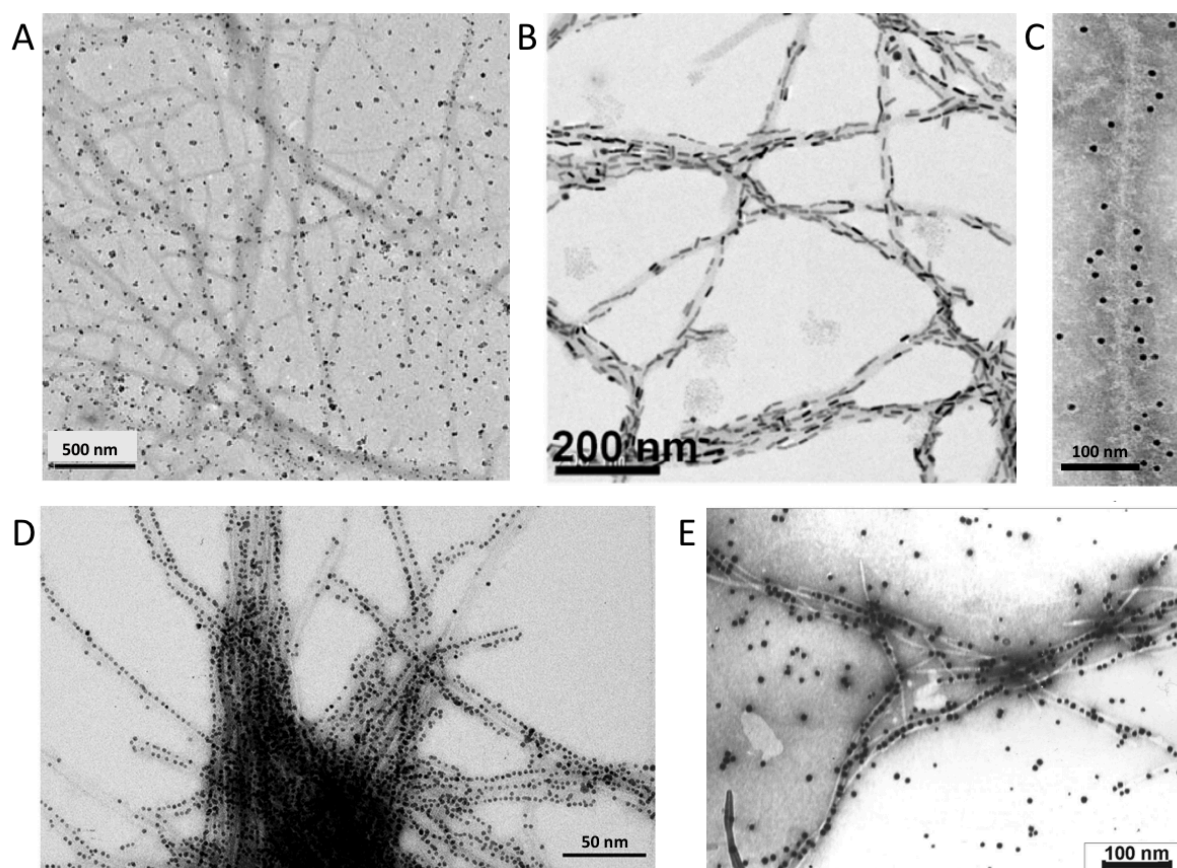


Figure 2.11 TEM images presenting previous work done on the amyloid fibrils labelled with nanomaterials. A) A β ₄₀ fibrils with magnetic Fe₂O₃ nanoparticles, B) α -synuclein fibrils labeled with gold nanorods, C) immunogold labeling of recombinant tau (a paired helical filament), D) A β ₄₀ fibrils labeled with negatively charged colloidal gold, E) modified α -synuclein with biotin labeled with gold nanoparticles conjugated with neutravidin. All images were reprinted and modified with permission from respectively A) (121), B) (126), C) (128), D) (127), E) (129).

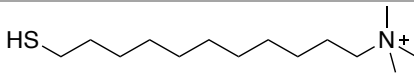
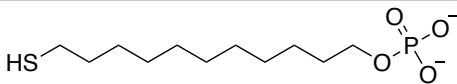
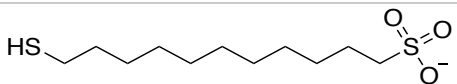
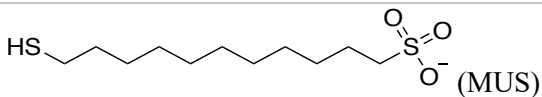
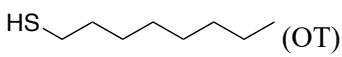
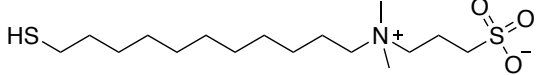
To address this limitation, our group developed gold nanoparticles that exhibit several important features for imaging the morphology of a single amyloid fibril. We synthesize monolayer protected gold nanoparticles of various sizes and ligand compositions on the surface (130, 131). Such nanoparticles have an electron dense core, but unlike gold particles used for immunostaining, they are not bound to an antibody. Recent experiments showed that amphiphilic gold nanoparticles, decorated with a mixture of hydrophobic and anionic ligands, can discriminatively adsorb on the edges of the amyloid fibrils made from different polypeptides. Among many possible applications, these gold nanoparticles facilitate the morphological characterization of different amyloid fibrils polymorphs (132).

2.2.3 State of art

The foundations of this work were established by Dr. Paulo H. Jacob Silva, who synthesized a variety of nanoparticles and tested their labelling efficiency on different mature amyloid fibrils with use of TEM and cryo TEM (132). Gold nanoparticles with various charges and ligands

were synthesized via two different methods – (I) modification of method developed by Zheng et al. (133) and (II) one-phase method, that was described previously (133). Among the nanomaterials that were tested on amyloid fibrils were small (with a core diameter of ~3 nm on average) spherical gold nanoparticles with (I) positive and (II) negative charge, (III) negatively charged nanoparticles with mixed ligands and (IV) zwitterionic nanoparticles (Table 4).

Table 4 List of the nanoparticles synthesized and tested by P. H. J. Silva with their charge, name and chemical structure of the protective ligands.

Nanoparticle charge	Nanoparticle name	Chemical structure of the protective ligands
Positive	allTMA	
	allMUP	
Negative	allMUS	
	MUS:OT ¹	 
Zwitterionic	ZW	

Positively charged nanoparticles (allTMA) were synthesized via modification of the method developed by Zheng et al. (133) and were protected by N,N,N-trimethyl(11-mercaptopundecyl)ammonium chloride. This type of nanoparticles was reported to adsorb on the surface of A β ₄₀ fibrils in the cooperative manner that very often led to total coverage and sedimentation of the fibrils. Moreover, all TMA nanoparticles were also reported to mediate in the bundling of the fibrils. This could be an effect of the elimination of repulsive interactions between different amyloids. Similar results were also observed for α -synuclein fibrils.

The same method of synthesis was used for obtaining zwitterionic (ZW) nanoparticles protected with 3-[(11-mercapto-undecyl)-N,N-dimethylamino]propane-1-sulfonate. The mode of interacting with amyloid fibrils was significantly different from the allTMA nanoparticles and no binding to A β ₄₀ or tau fibril surface was observed. Instead ZW nanoparticles were

¹ The percentage of OT in the ligand shell varied between 20% and 30% according to ¹H NMR analysis. No significant difference was observed in the labelling propensity of nanoparticles with OT amount within this range.

distributed evenly in the buffer and, as previously reported, resisted non-specific protein adsorption (134).

Negatively charged nanoparticles were synthesized via one-phase method, as described previously (133) and showed different levels of labelling amyloid fibrils due to their protective ligand. Nanoparticles protected with 11-mercaptoundecylphosphoric acid (allMUP) tend to aggregate in the presence of A β ₄₀ fibrils. Negatively charged nanoparticles protected by 11-mercaptop-1-undecanesulfonate (allMUS) showed good distribution in the buffer and no visible labelling of A β ₄₀ amyloid fibrils. This propensity changed after removal of the bigger nanoparticles and narrowing the size distribution in the batch by applying fractionation in sucrose gradient. allMUS nanoparticles fractionated in this way exhibited much better labeling of A β ₄₀ fibrils (Figure 2.12).

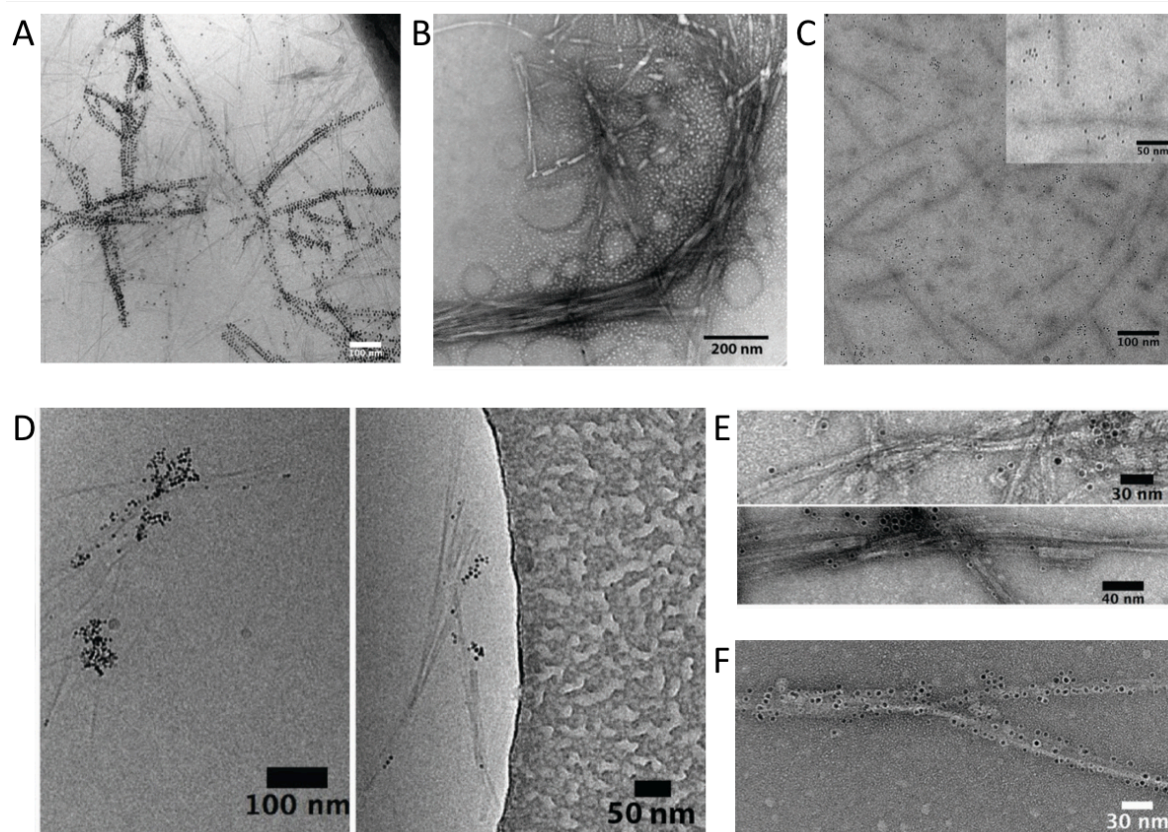


Figure 2.12 TEM and cryo TEM images of amyloid fibrils labelled with gold nanoparticles synthesized by P. H. J. Silva. A) Cryo TEM image of A β ₄₀ fibrils covered with allTMA nanoparticles, B) TEM image of α -synuclein bundle-like formation mediated by TEM nanoparticles. C) Cryo TEM image of tau protein incubated with ZW nanoparticles showing no labelling. D) Cryo TEM images of allMUP nanoparticles aggregated on the surface of A β ₄₀ fibrils. E) TEM image of A β ₄₀ fibrils sporadically decorated with allMUS nanoparticles. F) TEM image depicting improved labelling of A β ₄₀ fibrils with fractionated allMUS nanoparticles. All images are modified and reprinted from (132).

Addition of 1-octanethiol, hydrophobic ligand to the MUS ligand shell (MUS:OT nanoparticles) significantly improved labelling of A β ₄₀. Among different batches of MUS:OT nanoparticles, the percentage of 1-octanethiol in the ligand shell ranged from 10% to 30% (the

ligand shell composition was determined by ^1H -NMR spectroscopy). All these batches of MUS:OT nanoparticles exhibited well labelling properties. The coverage of $\text{A}\beta_{40}$ and α -synuclein fibrils was improved in comparison with fractionated allMUS nanoparticles. MUS:OT particles decorated preferentially edges of the twisted fibrils with better reproducibility and at longer length scales highlighting the fibril geometry. This kind of nanoparticles labelled also amyloid fibrils of tau protein (Figure 2.13).

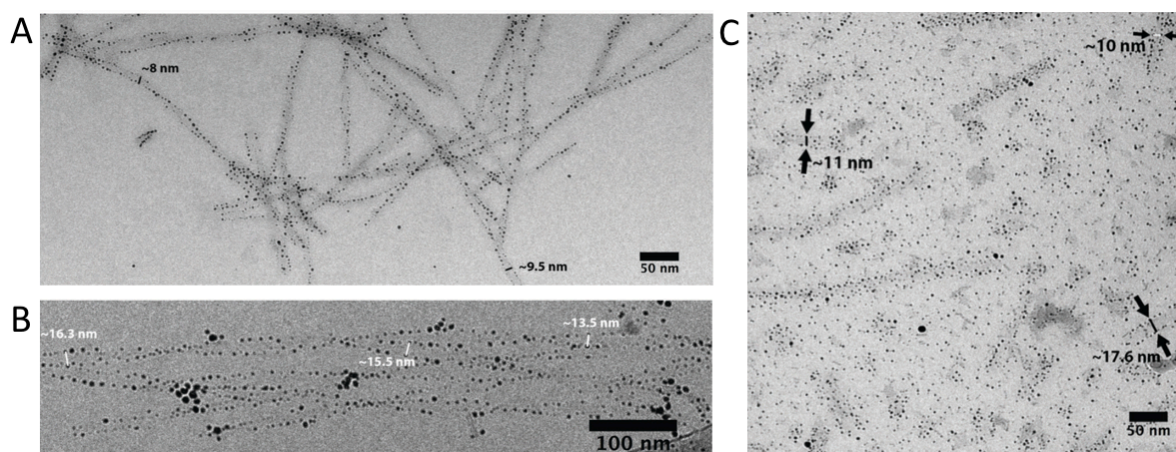


Figure 2.13 Cryo TEM images of MUS:OT nanoparticles decorating A) $\text{A}\beta_{40}$, B) α -synuclein and C) tau amyloid fibrils. Arrows and numbers depict distance between the nanoparticles on the two edges of the amyloid fibril. All images are modified and reprinted from (132).

More importantly, it was possible to visualize different morphologies of $\text{A}\beta_{40}$ fibrils such as twists of different widths and polymorphic species of three- and two-fold symmetric fibrils. The complex 3D arrangements such as splitting of the fibrils or overlapping in ice were also possible to visualize (Figure 2.14).

Further experiments showed that MUS:OT nanoparticles bind to the fibrils with better efficiency when the time of the coincubation is prolonged (more than 5 hours), there is lack of other structures that would compete with amyloids over the labelling with nanoparticles (e.g. fetal bovine serum), nanoparticles are synthesized via one-phase method and the diameter size of the nanoparticles does not exceed 5 nm. MUS:OT nanoparticles were also found to label first oligomers and decorate mature fibrils of tau protein after increasing the nanomaterial concentration. They were also reported to detect secondary nucleation sites by labelling small secondary nuclei protruding from the surfaces of the mature fibrils. These findings show that MUS:OT possess the affinity to intermediate structures of aggregation. It was also established that the interaction between nanoparticles and amyloids depends on the properties of amyloid fibril and the charge, size and solubility of the nanoparticle.

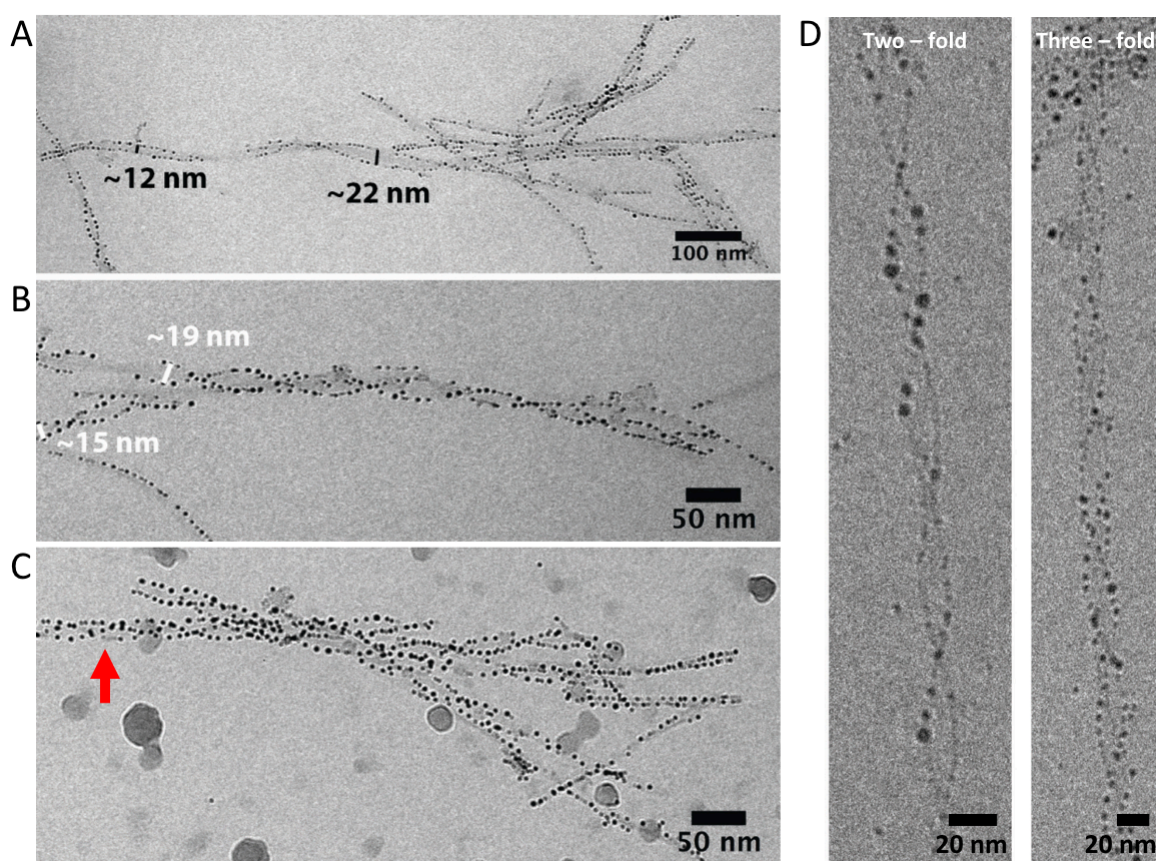


Figure 2.14 Cryo TEM images of A β ₄₀ amyloid fibrils decorated with MUS:OT nanoparticles showing A) fibrils of different width, B) splitting and entangling of two separate fibrils, C) mixture of two- and three-fold symmetric fibrils. Red arrow points at three-fold symmetric fibril. Panel D) shows the comparison between two single A β ₄₀ fibrils of different symmetry: two – and three-fold symmetry. Images are modified and reprinted from (132).

Research performed by Dr. P. H. J. Silva confirmed that MUS:OT nanoparticles are the most optimal tool for decorating amyloid fibrils. Moreover, these nanoparticles became a great candidate for studying intermediate species and protein-nanoparticle interactions. By subtly connecting material science with neuroscience, this work opened a new chapter of research conducted in our group. This thesis, as a direct heir of results presented in (132), shows further application of allMUS and MUS:OT nanoparticles in amyloid studies, especially in probing amyloid polymorphism and its properties.

Chapter 3

Investigating amyloid surface with the use of nanoparticles

3.1 Introduction

An alternative explanation for the different toxicity levels of polymorphic amyloid fibrils may lie in the variance of their surface properties. Interactions between the surface of the amyloid fibril and other biomolecules are mostly driven by electrostatic forces. These interactions play an important role in the aggregation process and the interplay with the membrane proteins, which is strictly linked to the cytotoxicity of the amyloid fibrils (127, 135). Previous studies have shown that distribution of the charge on the amyloid surface depends on the conformation of the fibril (135). For example, it was found that the surface potential of β -lactoglobulin was strictly correlated with the diameter of the fibril. The overall charge of the fibril was also found to depend on the pH of the buffer solution. This finding can be connected to the different polymorphic fibrils that are found in the tissues characterized with the distinct physiological milieu (135). Moreover, various studies proved that the toxicity of the A β fibrils, that possess a net negative charge, can be inhibited by covering their surface with positively charged proteins (127). These findings indicate that the toxicity of the amyloid fibrils may be connected to their surface properties and signifies the importance of studying this subject further.

The electrostatic properties of amyloids were previously assessed with the use of electrophoresis, however such measurement lacks the quantitative information about the distribution of the charge on the amyloid surface (136). In this chapter, we are proposing the use of our gold nanoparticles as a probing tool for the amyloid surface properties (Figure 3.1). For this purpose, we tested how MUS:OT and fractionated allMUS nanoparticles label modified huntingtin and α -synuclein amyloid fibrils.

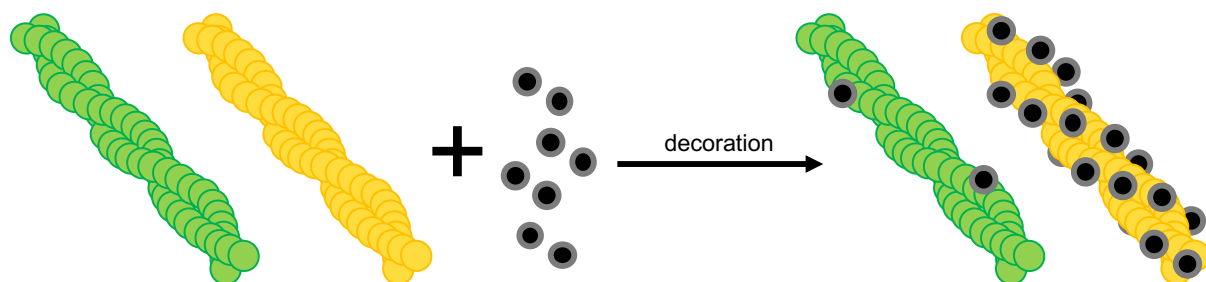


Figure 3.1 Schematic representation of the experimental section of this Chapter, which focuses on the amyloid surface probing with use of the gold nanoparticles.

Huntingtin (348 kDa) is a large, completely soluble protein composed of 3144 amino acids. The highest levels of this protein are expressed in the central nervous system neurons and testes (137). Huntingtin was found to be essential for the embryogenesis and forebrain development. Apart of that, some studies indicate its role in the formation of the central nervous system (137, 138). In a healthy organism, wild type huntingtin was also found to be connected to many other functions, such as neuroprotection or involvement in the brain-derived neurotrophic factor production and vesicular transport along microtubules. Due to the interaction with various cytoskeletal and synaptic vesicle proteins, huntingtin is also claimed to be involved in the synaptic transmission (137, 138).

The first exon of the huntingtin gene (*Httex1*) contains several repeats of CAG codon responsible for the glutamine expression. The wild type protein contains 10-35 CAG repeats, a higher number is associated with the development of Huntington's Disease (6). The onset of the disease is strictly correlated with the number of glutamines in the huntingtin: higher number of CAG repeats triggers the disease development earlier in the patient's life. In most cases however, the disease manifestation occurs at the age of 35 (137–139).

It was found that the polyQ regions aggregate when the polyQ domain exceeds 37 glutamines and the higher number of glutamines corresponds to the rate of the huntingtin aggregation (6). This aggregation results in the formation of amyloid fibrils, that are found in the nuclear and cytoplasmic inclusions of Huntington's Disease affected patients (6, 140).

Recent studies showed possible aberrant splicing, which leads to the spanning transcripts of *Httex1* instead of the full protein. Presence of smaller N-terminal fragments of huntingtin was found in the HD postmortem brains and the nuclear inclusions are detected only by antibodies targeting the N terminus of huntingtin. Moreover, mutant *Httex1* protein is sufficient to trigger the key features of Huntington's Disease in animal models (141). This suggests that the *Httex1* region plays a critical role in the development of the disease. *Httex1* contains three domains: N17 terminus fragment, polyQ region and proline rich domain. All of them are reported to be involved in the misfolding of the *Httex1* or full length huntingtin with CAG expansion (142). Positively charged N17 was reported to be a key regulator of localization of huntingtin, and as a place of several post translational modifications such as phosphorylation, SUMOylation or acetylation. Posttranslational modifications are reported to play an important role in the *Httex1* aggregation (142–144). Apart from that, N17 is linked with regulating the structure of huntingtin, its aggregation and interactions with other proteins and membrane binding (145). Moreover, presence of N17 terminus was found to enhance the aggregation of huntingtin, whereas deletion of this fragment resulted in the retardation of this process (140).

In order to understand how the surface of Httex1 amyloid changes upon the deletion of positively charged N17 terminus, we used two types of Httex1 amyloid fibrils – N17 truncated and full length Httex1. Both of them contained a toxic amount of 43 glutamines.

The second type of the investigated protein was α -synuclein (40 kDa), a small protein containing 140 amino acids, which is a part of the bigger synuclein family. This group of proteins includes also β - and γ -synucleins, however only α -synuclein was reported to be involved in the Lewy body disorders, such as Parkinson's Disease or Dementia with Lewy bodies (13, 146). Lewy bodies are cytoplasmic inclusions in the *substantia nigra* and they are the neuropathological characteristic of these diseases. It was found that Lewy bodies contain mostly α -synuclein amyloid fibrils (146, 147). In the physiological state, α -synuclein is associated with the synaptic vesicles and it is suggested to play an important role in the transmitter release (13). Due to this role, α -synuclein is especially abundant in the nervous system, mainly in the presynaptic terminals. To facilitate the interaction with the membranes, α -synuclein possess the apolipoprotein lipid binding motifs in its amino terminus (146, 147). Other regions present in α -synuclein are (I) hydrophobic NAC region (non A β component), which can fold into β -sheet, and (II) highly negatively charged polar C terminus (147). C terminus of α -synuclein is a site of several posttranslational modifications and it is involved in the protein-protein interactions (148). Truncation of this region enhances the aggregation of α -synuclein *in vivo* and *in vitro*, probably due to the removal of highly negatively charged domains, which normally contribute to the repulsion between the proteins (13, 148).

For the purpose of our studies we used two types of amyloids made from the first exon of the huntingtin protein: full length exon 1 with 43 glutamine repeats (FL Httex1 43Q) and N17 truncated exon 1 with exactly the same number of glutamines (NT Httex1 43Q). We also used two types of α -synuclein: unmodified wild type (α -syn WT) and α -synuclein with 20 amino acids truncated from the C-terminus (α -syn 120) (Figure 3.2)

This indicates that such a tight decoration of the FL Httex1 43Q is mediated by the presence of the positively charged N17. Moreover, lack of NPs attachment in the case of the N17 truncated protein, suggests the significant involvement of the N17 to the surface of the amyloid fibrils prepared from Httex1 fragment.

In order to examine the OT influence on the decoration, we incubated both types of the fibrils with MUS:OT nanoparticles. Cryo TEM images revealed densely decorated FL Httex1 43Q, which resembled the effect obtained with the use of fractionated allMUS nanoparticles (Figure 3.4). However, NT Httex1 43Q displayed slightly different behavior and few nanoparticles were observed on their surface. The amount of the MUS:OT nanoparticles that were decorating the NT Httex1 43Q amyloids were insignificant in comparison with the decoration obtained for FL Httex1 43Q with the use of the same nanomaterial in the same conditions (Figure 3.4 A-B). To address whether the decoration of NT Httex1 43Q is concentration depended, we performed concentration assay and incubated the same amount of fibrils with a 5 and 10 times more concentrated water solution of MUS:OT nanoparticles. The exact concentration values are mentioned on the caption of Figure 3.4. Cryo TEM images undeniably showed that the coverage is slightly improved as the MUS:OT nanoparticles ratio is increased, however it is still not as efficient as the labelling observed in the case of FL Httex1 43Q amyloids. Moreover, there was no visible difference between the decoration obtained with 5 or 10 times more concentrated solution of nanomaterial, which can suggest “saturation” of the fibrils’ surface already after the use of 5 times more concentrated MUS:OT solution.

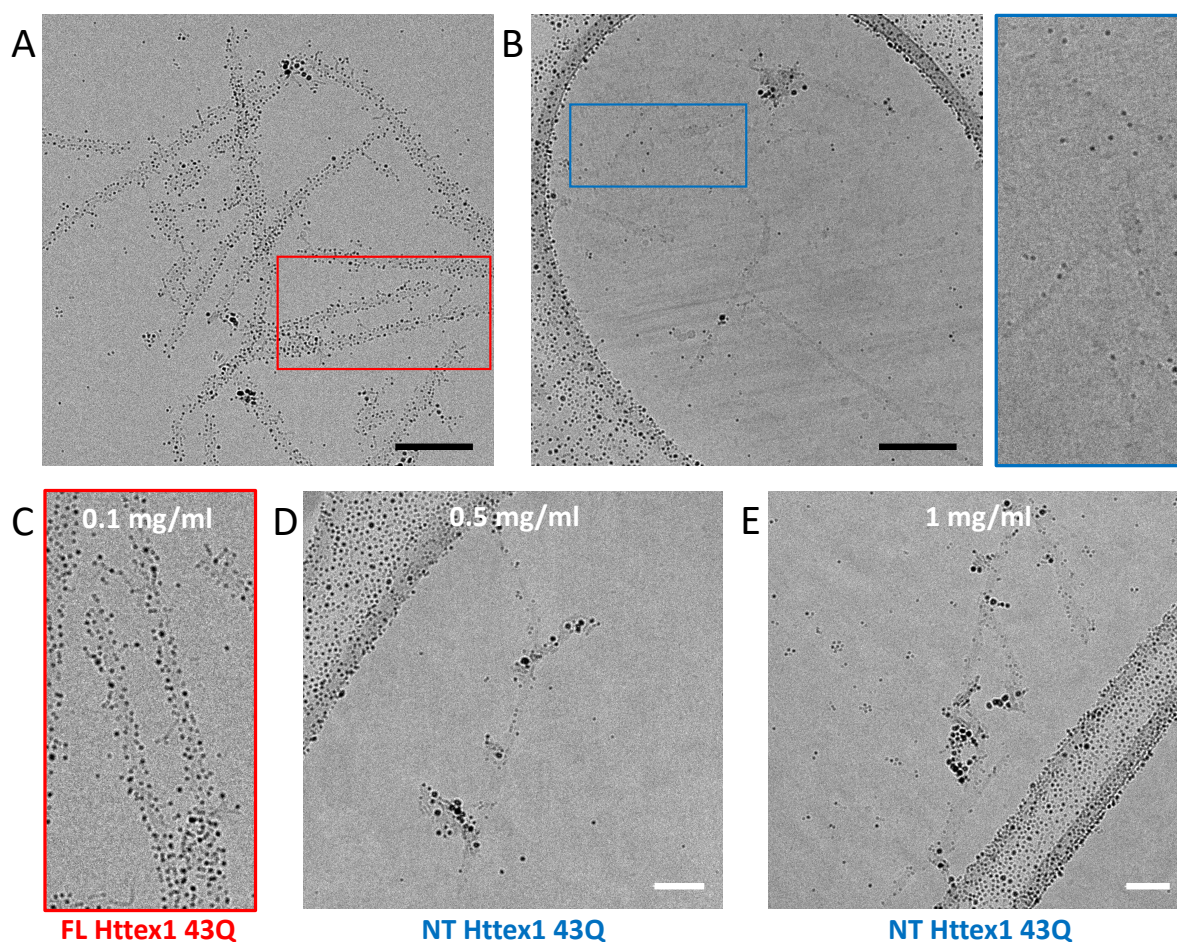


Figure 3.4 Cryo TEM images of FL Httex1 43Q and NT Httex1 43Q fibrils incubated with MUS:OT nanoparticles. A) FL Httex1 43Q incubated with MUS:OT nanoparticles (0.1 mg/ml concentration in the total solution). B) NT Httex1 43Q incubated with MUS:OT nanoparticles (0.1 mg/ml concentration in the total solution). The right panel depicts magnified and rotated blue box shown on the cryo TEM image in the left panel. C) Magnified and rotated red box from the cryo TEM image A. D) NT Httex1 43Q incubated with 5 times higher concentration of MUS:OT nanoparticles (0.5 mg/ml concentration in the total solution). E) NT Httex1 43Q incubated with 10 times higher concentration of MUS:OT nanoparticles (1 mg/ml concentration in the total solution). Black scale bars are 100 nm and white scale bars are 50 nm.

This study proved that the surface properties vary greatly between the FL Httex1 43Q and NT Httex1 43Q and this difference can be observed with use of both types of used nanoparticles. The presence of OT in the ligand shell improves the decoration of NT Httex1 43Q, which suggests that there are hydrophobic sites on the surface of the fibril that can attract MUS:OT nanoparticles more than fractionated allMUS nanoparticles. Despite that, this effect is minimal in comparison with the decoration obtained for FL Httex1 43Q with the use of the same type of nanoparticles. Even in the solution with 10 times higher concentration of nanoparticles, NT Httex1 43Q remains largely undecorated (Figure 3.4 C-E).

Interestingly, we found that this propensity is visible only with the use of cryo TEM. Both samples presented in Figure 3.4 were also visualized with the use of negative stain TEM. FL Httex1 43Q were found to create aggregates of rather short and tightly decorated fibrils, which was in agreement with the cryo TEM data. However, we noticed significant difference in the

NT Httex1 43Q behavior. Negative stain TEM images depicted long entangled fibrils, with previously not apparent nanoparticle labelling (Figure 3.5). This effect is achieved due to the blotting and drying steps of the negative stain TEM sample preparation process. These steps cause motion of the solution and unbound nanoparticles, that are mechanically stopped by the fibrils attached to the surface of the grid. Another possible explanation of this effect is that nanoparticles are trapped below the immobilized fibrils and cannot be removed during the blotting step. This at first may be mistaken as labelled fibrils.

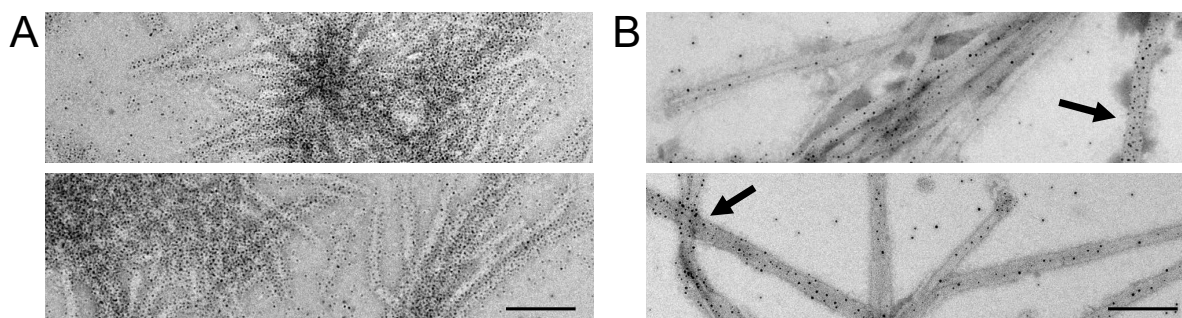


Figure 3.5 Negative stain TEM images of the Httex1 43Q amyloid fibrils incubated with the fractionated allMUS nanoparticles. A) FL Httex1 43Q aggregates, B) NT Httex1 43Q fibrils “decorated” with the nanoparticles. Black arrows point at the fibrils highly associated with the nanoparticles, which is an artifact stemming from the sample preparation. Scale bars are 100 nm.

Results obtained with the use of negative stain TEM, indicate that cryo TEM is more suitable technique for visualization of amyloid fibrils interactions with the gold nanoparticles. This technique is devoid of not only surface interactions with the sample, but also excludes the blotting and drying steps, which can induce false positives as shown in Figure 3.5 B.

The next step was to understand if the lack of decoration observed with the use of fractionated allMUS nanoparticles originates from their possible depletion by the small intermediate structures present in the NT Httex1 43Q sample. To address this question, we attempted the separation of the structures present in the solution with the use of centrifuge. First, the stock solution of NT Httex1 43Q fibrils was divided in to two major aliquots. The first one was centrifuged and separated into two equal parts due to their position in the tube after the centrifugation. The upper part of the solution (named henceforth “supernatant”) was expected to contain only smaller particles such as oligomers or monomers while the bottom part (referred as “fibrils”) was expected to be richer in mature amyloid fibrils. The two parts were then incubated with fractionated allMUS nanoparticles. This approach should demonstrate whether the presence of potentially more susceptible for the decoration structures inhibit the labelling of NT Httex1 43Q fibrils. The second aliquot of the NT Httex1 43Q fibrils stock solution was first incubated with the fractionated allMUS nanoparticles prior to the centrifugation.

Centrifugation and division of the obtained solution was performed in exactly the same way as described for the first aliquot. The aim of this approach was to concentrate the amount of the fibrils, which would increase the probability of detecting the decorated ones during the microscopy analysis. Another reason was to perform imaging of the smaller structures present in the upper layers of the solution immediately after the disturbance of the balance between all of the species present in the sample. This step interrupted possible fibrillation of the intermediate structures. The schematic representation and results of these experiments are shown in Figure 3.6.

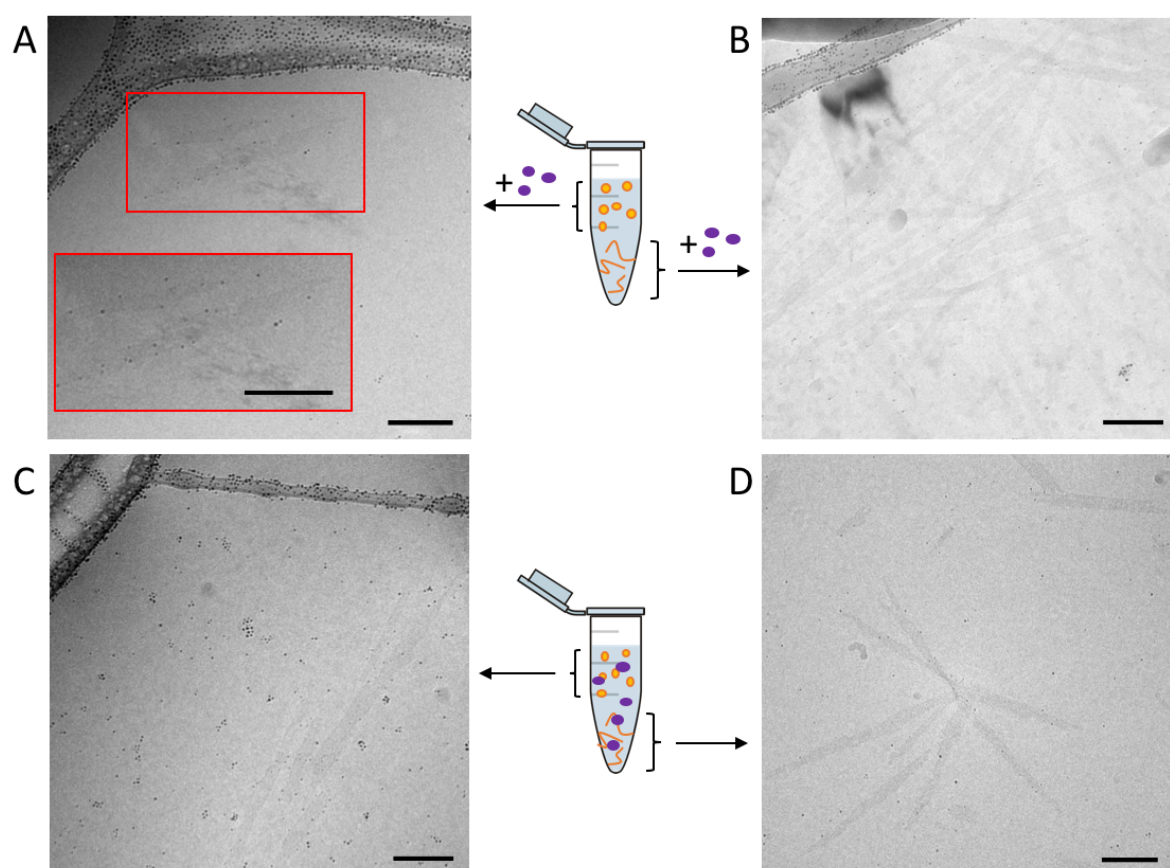


Figure 3.6 Schematic representation and results of the experiment that should elucidate the role of the intermediate structures in the apparent lack of NT Httex1 43Q fibrils decoration. Following panels are showing cryo TEM images of A) “Supernatant”, that was first separated from the bulk solution and then incubated with the fractionated allMUS nanoparticles. The red box is enlarged fragment of the image, showing elongated structures that are sparsely labelled by nanomaterial, B) “Fibrils” derived from the bulk solution and then incubated with the gold nanoparticles, which shows no apparent labelling of the fibrils, C) “Supernatant” obtained after the incubation of the bulk solution with the nanomaterial, that shows no particular labelling of the fibrils but small assemblies of the nanoparticles suggesting the decoration of smaller structures present in this part of the solution and D) “Fibrils” solution obtained after the incubation with fractionated allMUS nanoparticles and centrifuged, which show no apparent decoration. All scale bars are 100 nm.

Noticeably, in both “supernatant” solutions, we were able to find mature amyloid fibrils, however, their amount was significantly diminished compared to the control sample, and only few fibrils were spotted in the ice during the cryo TEM measurement. This could be due to the imperfect separation of the solution or not sufficient time or speed of the centrifugation.

However, this can also elucidate the behavior of these fibrils in different fibrils/nanoparticles ratio. There was no noticeable labelling of amyloids in both samples containing “fibrils”. In these samples, the amount of the amyloids was increased and all of the imaged fibrils were uniformly bare. More interesting behavior was noticed in the case of the fibrils captured in the “supernatant” sample, which was incubated with the nanomaterial after the separation from the bulk solution (Figure 3.6 A). Few nanoparticles were loosely attached to the edges of the fibrils, presumably due to the high nanoparticles to amyloids ratio. However, the majority of them was concentrated on the grid support and the decoration of these NT Httex1 43Q fibrils was significantly low in comparison with the decoration of the FL Httex1 43Q fibrils captured in the previous experiment. Moreover, the sample containing “supernatant” (that was derived from the bulk solution which was incubated with the nanomaterial prior to the centrifugation) displayed small aggregates of nanoparticles (Figure 3.6 C). These small agglomerations can indicate the presence of smaller structures prone to the labelling with fractionated allMUS nanoparticles. Few nanoparticles were also spotted at the edges of the visualized fibrils, however as it is apparent in the Figure 3.6 A, their number is insignificant. The presence of these small agglomerates was not pronounced as much in the “supernatant”, which was incubated with the gold nanomaterial after the separation from the bulk solution. The decoration of smaller structures, possibly oligomers, with the nanoparticles may suggest different surface properties, such as different charge or presence of spatial “pockets” that could mechanically trap nanoparticles.

Importantly, results of this study indicate that the slight decoration of NT Httex1 43Q with fractionated allMUS nanoparticles is possible only with the higher ratio of nanoparticles to the fibrils and even then, the decoration is insignificant in comparison with FL Httex1 43Q fibrils. In order to unify the treatment of NT Httex1 43Q and FL Httex1 43Q fibrils and compare the results obtained in exactly the same procedure, we prepared a 50:50 mixture of both Httex1 43Q fibrils. This mixture was then incubated with fractionated allMUS nanoparticles. The cryo TEM images reveal the two populations of the fibrils to be easily distinguished by the interaction with the nanomaterial (Figure 3.7).

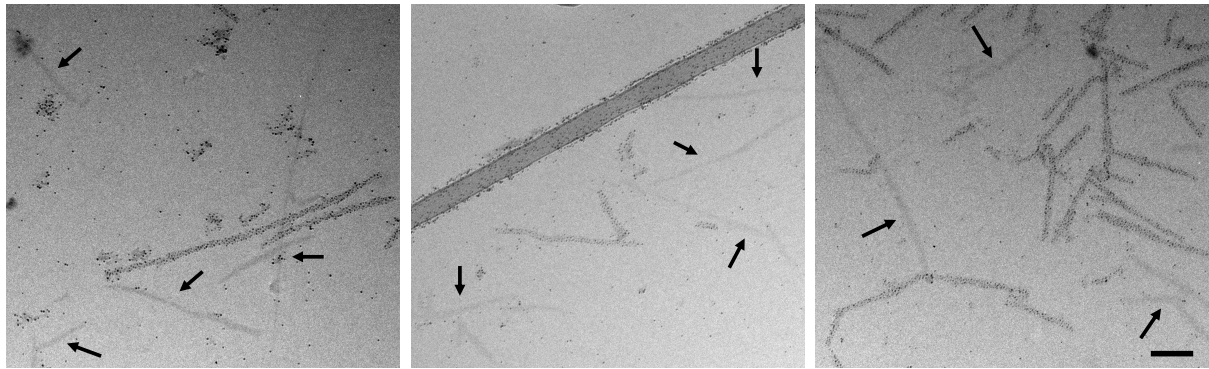


Figure 3.7 Compilation of cryo TEM images of the 50:50 FL Httex1 43Q and NT Httex1 43Q mixture that was incubated with fractionated allMUS nanoparticles. The images show two populations of the fibrils: bare (supposedly NT Httex1 43Q) and decorated (supposedly FT Httex1 43Q). The arrows are pointing at the bare fibrils. Scale bar is 100 nm.

One group of the fibrils was tightly decorated by the nanomaterial in a manner that resembled the decoration of FL Httex1 43Q. The other group of the fibrils remained bare as in the case of NT Httex1 43Q. We assume, that these two populations of differently labelled fibrils are in fact NT Httex1 43Q and FL Httex1 43Q, which proves that our gold nanomaterial could potentially serve as a probing tool for distinguishing different types of the amyloids with one measurement.

A more challenging system was encountered by wild type and C truncated α -synuclein. In this case both of the types were decorated by MUS:OT and fractionated allMUS nanoparticles (Figure 3.8).

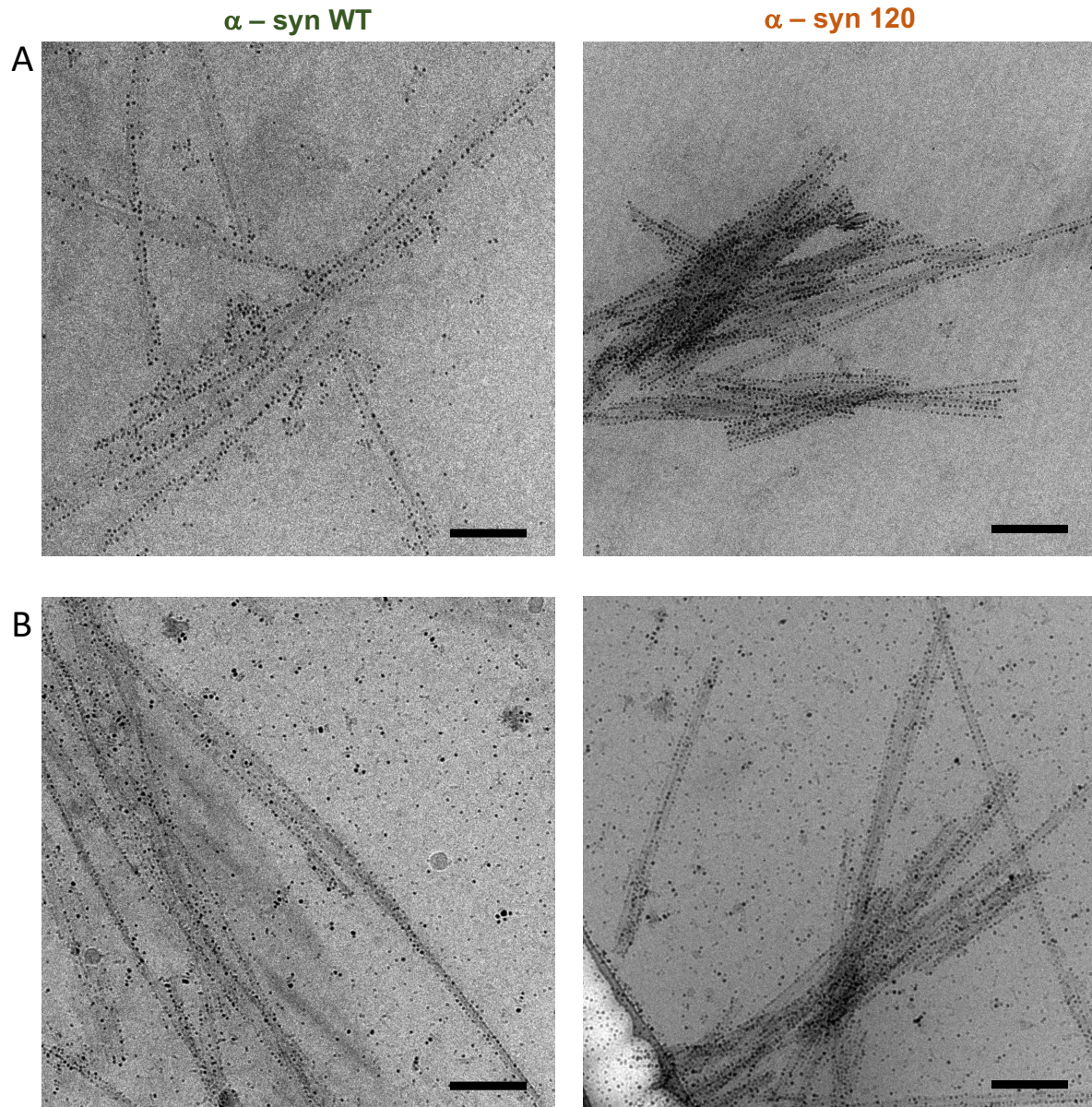


Figure 3.8 Cryo TEM images of α -syn WT and α -syn 120 fibrils decorated with A) fractionated allMUS and B) MUS:OT nanoparticles. Scale bars are 100 nm.

Both types of the fibrils displayed slightly different morphology: α -syn WT amyloids were longer and better distributed in the ice than shorter α -syn 120 fibrils, which tend to create small aggregates. After incubation with MUS:OT and fractionated allMUS both types of the fibrils were decorated, however α -syn 120 seemed to be decorated more densely. This observation would be supported by the fact that the C terminus of α -synuclein is strongly negatively charged and removal of last 20 amino acids from the C end significantly lowers the net negative charge of this protein. Moreover, decoration of α -syn WT with negatively charged nanoparticles indicates the presence of positive charge on the surface of the fibril, that gets only more pronounced after the C terminus modification.

To quantify the subtle differences between the nanoparticle decoration of these two types of α -synuclein, we developed a nearest neighbor analysis. On this analysis, the center to center distance between two adjacent nanoparticles decorating the edge of the fibril, was measured. As previously observed on the cryo TEM images in Figure 3.8, calculations showed that α -syn 120 fibrils were on average more densely decorated than α -syn WT fibrils. Average nearest neighbor distance between MUS:OT nanoparticles decorating α -syn 120 was 6.7 ± 1.2 nm, while for α -syn WT the average nearest neighbor distance was 7.0 ± 1.3 nm. The same values were obtained for fractionated allMUS nanoparticles, 7.0 ± 1 nm for α -syn 120 and 8.5 ± 2.1 nm for α -syn WT. The obtained values were subsequently plotted in histograms, which highlighted the differences in the coverage between the two studied types of α -synuclein (Figure 3.9).

Figure 3.9 A shows the comparison between nearest neighbor values obtained with the same type of nanoparticles on two different α -synuclein fibrils. Both types of the nanoparticles label α -syn 120 more tightly than WT, which can be explained by the absence of highly negatively charged C terminus. This facilitates the labelling of the amyloid fibrils with our negatively charged nanoparticles. Figure 3.9 B shows the comparison of nearest neighbor values obtained on the same type of fibril with different nanoparticles. In both cases fractionated allMUS nanoparticles label fibrils less tightly, while MUS:OT nanoparticles tend to decorate both types of the fibrils more closely. An explanation for the more thorough decoration that was obtained with the use of MUS:OT nanoparticles, could derive from the presence of the hydrophobic OT in the MUS:OT nanoparticles ligand shell. OT ligands could contribute to the decoration via strengthening hydrophobic interactions between the nanomaterial and the surface of the fibril. All of discussed differences were statistically significant (Figure 3.9 C).

This study showed that with the use of our gold nanomaterial, we could address the changes in the surface of amyloid fibrils, derived from the protein primary structure modification. Measurement of the nearest neighbor distance, allowed us to quantify the differences in the decoration propensity between the unmodified and C-truncated α -synuclein fibrils. Fibrils that lacked highly negatively charged C-terminus were decorated more efficiently with both tested types of the nanoparticles, than wild type fibrils. This result shows the contribution of the C-terminus domain to the surface of the amyloids formed by the two types of examined α -synuclein proteins. This data shows that our gold nanoparticles could be potentially used as a tool for probing the surface of amyloid fibrils.

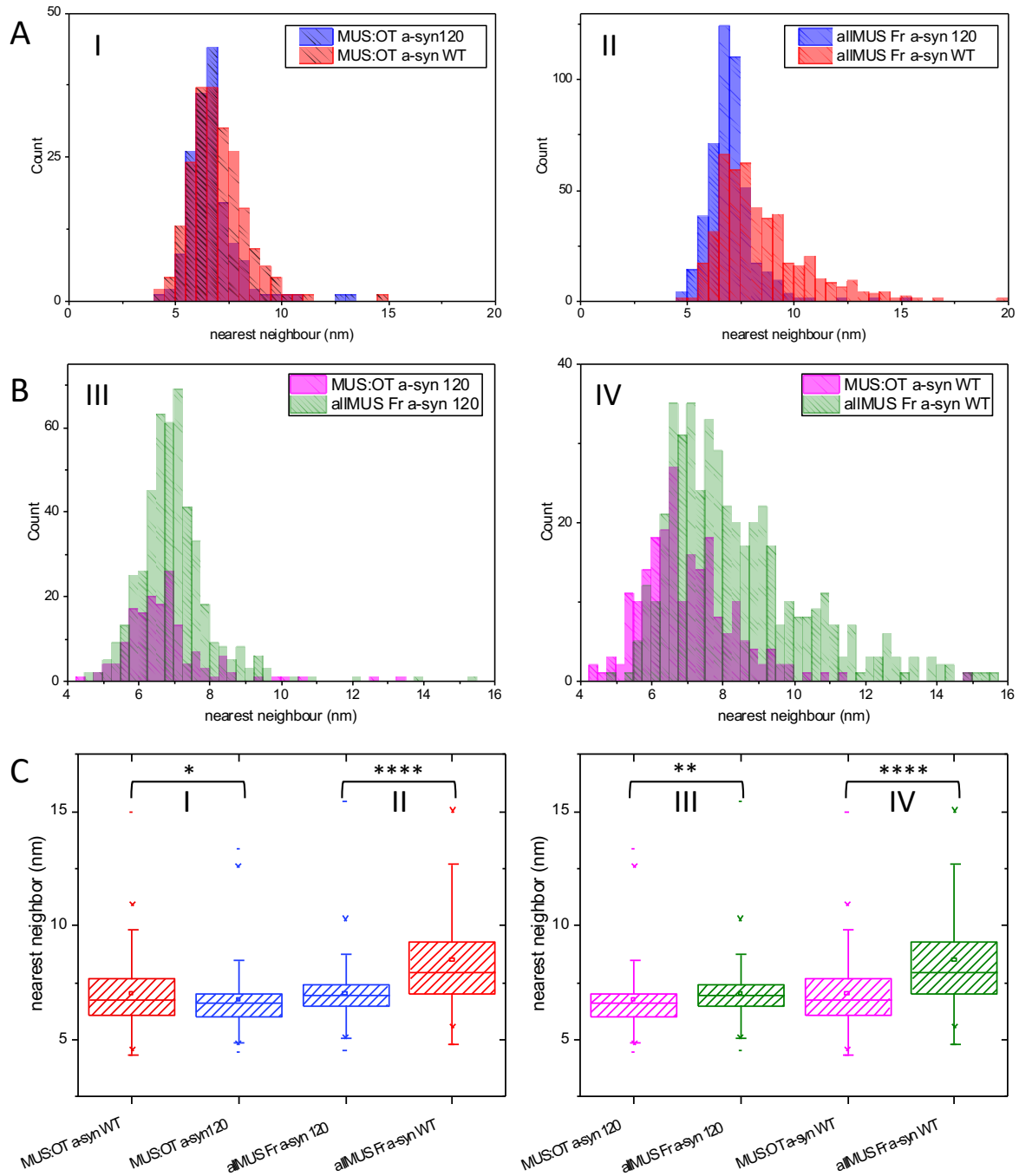


Figure 3.9 Nearest neighbor measurement of gold MUS:OT and fractionated allMUS nanoparticles decorating α -syn 120 and α -syn WT fibrils. A) comparison of the results due to the type of the fibril. Panel I shows the difference in the nearest neighbor distance obtained for both types of the fibrils with use of MUS:OT nanoparticles and panel II shows the same measurements obtained for fractionated allMUS nanoparticles. B) comparison of the results due to the type of the nanoparticles. Panel III shows the nearest neighbor values calculated on α -syn 120 with the use of both types of the nanoparticles and panel IV presents the same measurements obtained for α -syn WT fibrils. C) Statistical analysis of the obtained results. Left panel shows the comparison between the different types of the fibrils decorated with the same nanoparticles and right panel shows the comparison between the different types of nanoparticles labelling the same type of the α -synuclein fibrils.

In order to address the possible operator related error of the nearest neighbor measurement, two independent operators performed this measurement on R2 peptide derived from the tau protein. R2 fibrils were decorated with fractionated allMUS nanoparticles (Figure 3.10). Both

operators were free to choose the images and the visible structures for the analysis. Operator 1 was more selective by picking 5 images and making 443 counts in total, while operator 2 made 647 counts on only 4 images. Despite these two different approaches, there was no statistical difference between the results obtained by both operators, which indicates, that operator related errors are minimal in this method.

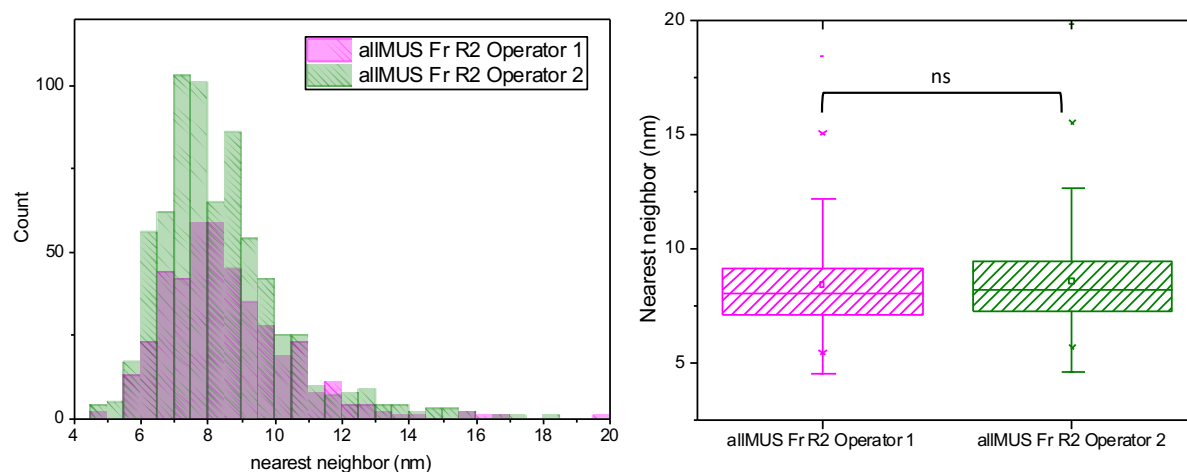


Figure 3.10 Nearest neighbor measurement performed by the two independent operators on the same sample. Left panel shows overlapped histograms with the results and right panel shows the statistical analysis that indicated no significant difference between the obtained values.

Nevertheless, this method is very sensitive to other variabilities. One of them is the ratio between the nanoparticles and fibril concentration. Nanoparticles may first sit on the unoccupied surface in such way as to mitigate the repulsion between them. The concentration of the nanoparticles and fibrils should be strictly monitored in order to perform the comparison. Another point that should be controlled is the size of the nanoparticles. The value of nearest neighbor is based on the center to center distance and will be significantly bigger for the nanoparticles with bigger diameter, even with the tight decoration.

3.3 Conclusions

We were able to compare surface properties of two wild type amyloids and their modified versions. We can observe significant differences in the decoration of FL Httex1 43Q and NT Httex1 43Q, which was connected to the loss of the positively charged N17 terminus. The effect was more pronounced for fractionated allMUS nanoparticles that are devoid of hydrophobic ligand. This effect suggests that fractionated allMUS nanoparticles are a more sensitive probing tool, but less effective for decoration. The slight improvement of the decoration obtained with use of the MUS:OT nanoparticles suggest the contribution of the hydrophobic domains placed on the surface of the NT Httex1 43Q fibrils.

This difference was not possible to capture with the use of negative stain TEM due to the drying artefacts.

Nanoparticles were also successfully used in the surface probing of α -synuclein and its modified C-truncated version. This system was marginally more challenging since both of the α -synuclein types were decorated by MUS:OT and fractionated allMUS nanoparticles. This obstacle was overcome with the application of nearest neighbor measurement, which quantifies the density of the decoration of the fibrils. Employing this analysis, we could see the differences in the labelling mode between both α -synuclein fibrils, among which α -syn 120 was decorated significantly more tightly than α -syn WT. This difference may stem from the truncation of the highly negatively charged 20 amino acids from the C terminus, which mitigated the repulsion of the negatively charged nanoparticles. This hypothesis is also supported by the observation that MUS:OT nanoparticles decorated the fibrils more tightly, probably due to the presence of the hydrophobic OT ligand. Visible good decoration of α -syn WT fibrils with negatively charged nanoparticles points towards the contribution of positive charge displayed on the fibril surface, despite its strong net negative charge.

Study performed in this chapter, shows that our gold nanoparticles are a good potential tool to probe and study the surface of the amyloid fibrils, including differently folded polymorphic species.

3.4 Materials and methods

Nanoparticles

MUS:OT nanoparticles were synthesized according to the one-phase method (149) with modifications in the particle purification step. The whole procedure of synthesis and purification was previously described by Guven et al. (150).

Briefly, 180.9 mg (0.3 mmol) of gold salt ($\text{HAuCl}_4 \cdot 3\text{H}_2\text{O}$) in 200 ml of ethanol was stirred in a 500 ml round-bottom flask, until the gold salt was completely dissolved. In a separate glass vial, the mixture of MUS:OT was dissolved in 15 ml of methanol, aided by sonication. To reach a 1:1 feed ratio of the ligands, 65.5 mg of MUS and 39 μl of OT were used. The desired thiolated ligand mixture was then added to the gold salt, dissolved in ethanol while stirring and stirred together for approximately 15 min. During that time, the color of the solution changed from translucent to turbid yellow, indicating the formation of gold-thiolate complexes. Then, a filtered, saturated solution of 500 mg of sodium borohydride (NaBH_4) dissolved in 100 ml of ethanol was added dropwise. The addition of NaBH_4 was adjusted in such a way that the whole process took 1 h in order to avoid quick reduction. The solution was stirred for another hour. After that time, the reaction was assumed to be finished, and the vessel was closed with the septum pierced with a needle to allow controlled H_2 gas release. The flask was then placed in the refrigerator and kept at 4°C overnight. After that time, a black precipitate was collected via decantation. This residue was washed several times (5 times at each step) with ethanol and dried under vacuum to remove ethanol. To completely remove unbound species, particles were centrifuged several times with MilliQ water using Amicon® Ultra-15 centrifugal filter devices (10k or 30k nominal molecular weight limit (NMWL)). The particles were then suspended in a small amount of water (~ 2 ml) and freeze-dried.

AllMUS nanoparticles were obtained in the same way except MUS constituted 100% of thiolated ligands added to the gold salt solution at the first step of the synthesis.

Characterization of the nanoparticles

The NPs were characterized using TEM, ^1H -NMR spectroscopy and thermogravimetric analysis (TGA), as presented in Figure 3.11. The ligand density on nanoparticle was measured by TGA, size and polydispersity of the nanoparticles were characterized by TEM and the nuclear magnetic resonance spectroscopy was used both to assess the presence of unbound ligands and to determine the ligand-shell composition.

To analyze the level of impurities in the sample 5 mg of the nanoparticles powder was dissolved in 600 μ l of D₂O before ¹H-NMR analysis was performed. The absence of sharp peaks in the NMR spectrum indicates the absence of impurities in the solution.

The ratio between protective ligands was assessed also with the use of ¹H-NMR spectroscopy in the following way: an etching solution of 15 mg of iodine (Acros) in 100 ml of MeOD-d₄ (Sigma) was prepared. Between 1 and 5 mg of nanoparticles were suspended in 0.6 ml of the etchant mixture for 30 min under sonication. After the NMR spectrum for the etched solution was obtained, the ligand ratio was calculated according to the integrals of the given peaks indicating the ligand ratio on this batch of nanoparticles corresponds to 21% of OT and 79% of MUS.

To perform TGA analysis between 2 and 8 mg of the NPs powder was placed into a TGA crucible. The temperature was increased to 900°C with heating at 5°C per min. The organic ligands degrade in time as the temperature increases, leaving the gold core of the nanoparticles. Degradation of the ligands causes weight loss, which is monitored and plotted against the temperature, enabling the monitoring of ligand desorption with time. The difference between the beginning and the final weight for the sample allows for the determination of the ligand density on the NPs. The equipment used was a TGA 4000 system from Perkin Elmer.

For analyzing the size and dispersity of the nanoparticles a drop of 4 μ l of NPs (0.1-0.5 mg/ml) was deposited onto a 400-mesh carbon-supported copper grid and left to dry. TEM images were acquired using a FEI TALOSTM electron microscope with an acceleration voltage of 200 kV and equipped with a Ceta CCD camera. Images of the nanoparticles were analyzed using Fiji software, and their diameter was calculated using a homemade script compatible with this software. The analysis shown that the size of the used batch of the MUS:OT nanoparticles is equal to 2.5 nm \pm 0.5 nm.

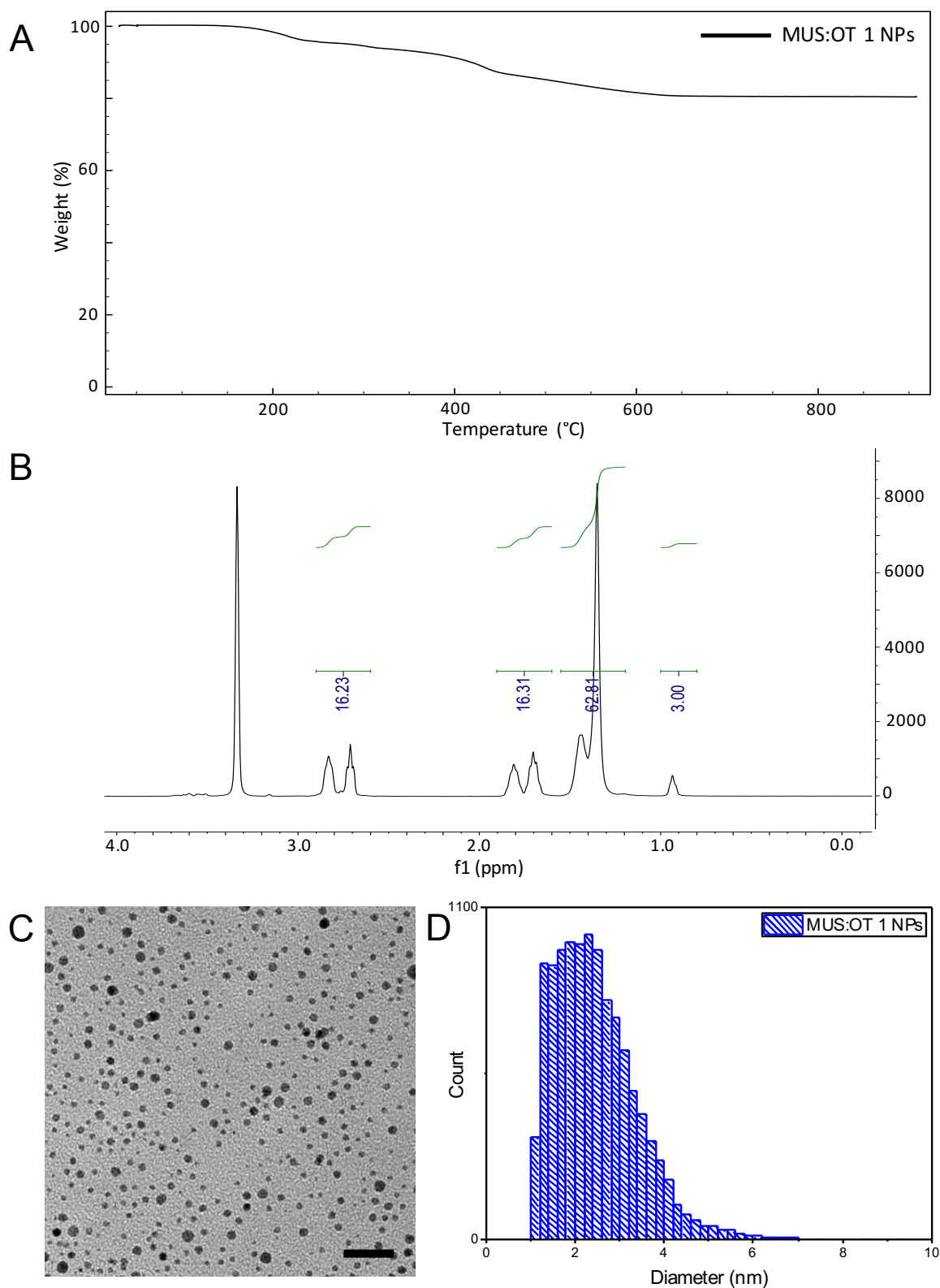


Figure 3.11 Characterization of MUS:OT nanoparticles. a) Thermogravimetric analysis (TGA) plot of MUS:OT nanoparticles. The TGA curve is indicative of drying, desorption and thermal degradation of organic ligands. In the case of the MUS:OT nanoparticles, OT desorbs between 176°C and 233°C, while MUS is decomposed at approximately 800°C. The remaining weight at higher temperatures corresponds to the gold core of the nanoparticles. The mass difference between the beginning and the end of this analysis allows for the ligand density estimation. b) ^1H -NMR analysis of MUS:OT etched with iodine solution in MeOD- d_4 reveals the MUS:OT stoichiometric ratio, which in the case of MUS:OT is 21 to 79, MUS to OT. c) Cryo TEM images of MUS:OT. Scale bar is 20 nm. d) Particle size distribution of MUS:OT obtained from the analysis of several cryo TEM images.

Fractionation of allMUS nanoparticles

To limit the size polydispersity the sucrose-gradient fractionation was used on the allMUS nanoparticles. The technique was described previously by Carney et al. (151). Briefly, from 20% to 50% w/w sucrose solutions were prepared and placed in SW32 centrifuge tubes in the way that the interface between them was clearly visible. Then with the use of Gradient Station (Biocomp Instruments) the linear gradient of sucrose solution was created. The solution of allMUS nanoparticles was placed on the top of the tube where the sucrose concentration was the smallest and centrifuged in a Beckmann XL90 ultracentrifuge with SW32 Ti swinging bucket rotor for 2 h at 32000 rpm at 20°C. This allows nanoparticles to migrate in the sucrose gradient according to their size and surface properties: the biggest nanoparticles will migrate to the lower part of the tube with the higher sucrose density, whereas smaller nanoparticles will remain in the upper layers of the less concentrated sucrose gradient. Then with the use of the Gradient Station samples were manually fractionated with use of the piston that allows for the manual drain of the centrifuge tube from the meniscus to the bottom. This procedure decreased the polydispersity of the used allMUS nanoparticles from 2.4 ± 1.8 nm to 2.7 ± 0.9 nm.

Huntingtin exon 1 (Httex 1)

Both fibril types: N-truncated 43Q (with the first 17 amino acids removed) and full length 43Q Httex1 were prepared according to a previously reported protocol (152). Briefly, Httex1 with polyQ repeats equal to 43Q was synthesized using an intein-based strategy that allows for the production of native tag-free huntingtin exon 1. Fibrils were formed by keeping the solution of monomers at 37°C without shaking. Fibrils were prepared by Dr. Sophie Vieweg.

Wild type α -synuclein

Human full length α -synuclein was purchased from rPeptides and used as received. To 1 mg of lyophilized powder, 1 ml of TBS buffer was added, and the solution was filtered through a 100 kDa MW cutoff Microcon filter (13000 g, 15 min, 4°C). The concentration was adjusted to 40 μ M using the extinction coefficient at 275 nm ($5974 \text{ M}^{-1}\text{cm}^{-1}$). Fibrils were grown over the period of one week at 1000 rpm and 37°C. Fibrils were prepared by Anass Chiki.

Modified α -synuclein

Human truncated α -synuclein (1-120) in pT7-7 was expressed in *E. coli* strain BL21, purified and characterized as described by Fauvet et al. (153) except that the anion exchange chromatography step was replaced by a cation exchange chromatography step due to the lack

of the negatively charged C-terminal domain. The fibrils were prepared as described for the wild type protein. Fibrils were prepared by Anass Chiki.

Incubation of the amyloid fibrils with nanoparticles

Mature amyloid fibrils prepared as described above were dispersed in their corresponding buffer and incubated at 37°C in a thermomixer with a water solution of nanoparticles. The samples were incubated for the period of 24 h to 72 h under the shaking speed in the range 300-600 rpm. At the end of the incubation, samples were gently resuspended using a pipette to generate some agitation immediately prior to cryo grid preparation.

Negative stain TEM of amyloids

Recombinant samples were deposited onto glow-discharged 400-mesh carbon-supported copper grids for 1.5 min at room temperature. The grids were then blotted with filter paper, washed once with MilliQ water and stained with a 1% w/v uranyl acetate solution for 30 s. The blotted grids were air-dried and imaged using a FEI TALOS electron microscope at an acceleration voltage of 200 kV and equipped with a Ceta CCD camera.

In the case of the *ex vivo* samples, 3.5 µl of each sample was applied onto glow-discharged Formvar/carbon coated 200-mesh copper grids (Electron Microscopy Sciences) for 1 min. The grids were blotted with filter paper, washed twice with ultrapure water, washed once with uranyl formate 0.7% (w/V), stained with uranyl formate for 30 s, blotted and dried. The prepared specimens were inspected with a Tecnai Spirit BioTWIN system operated at 80 kV and equipped with an Eagle CCD camera.

Cryo electron microscopy of amyloid and nanoparticle samples

For cryo TEM microscopy, a 3 µl droplet of sample containing amyloids and nanoparticles suspended in buffer was deposited onto a lacey carbon film (Electron Microscopy Sciences) and blotted to a thin (100-300 nm) layer of liquid that was flash frozen in liquid ethane using an FEI Vitrobot Mark IV. Imaging was performed using a Gatan single tilt cryo holder operated on an FEI Tecnai Spirit BioTWIN 80 kV transmission electron microscope in LowDose Mode to visualize the samples at an average exposure of 1-3 electrons/Å² on a Ceta camera.

Nearest neighbor measurement

To quantify and compare the decoration of different amyloids with different nanoparticles an analytical method based on cryo TEM images was developed.

Analysis is performed in Pebbles and in Matlab software with the use of homemade script. First step is scanning for nanoparticles on the cryo TEM images in the Pebbles software. Scanning is based on contrast between dark core of the nanoparticle and bright ice around it. Center and radius of all scanned nanoparticles are automatically calculated and saved by the software in Matlab file format. Then homemade script based on Euclidean distance formula calculates the center to center distance of given nanoparticles (Figure 3.12).

This type of analysis allows the experimentalist to compare and quantify differences of decoration level between various amyloid fibrils and polymorphic amyloid fibrils composed of the same protein but with different morphology.

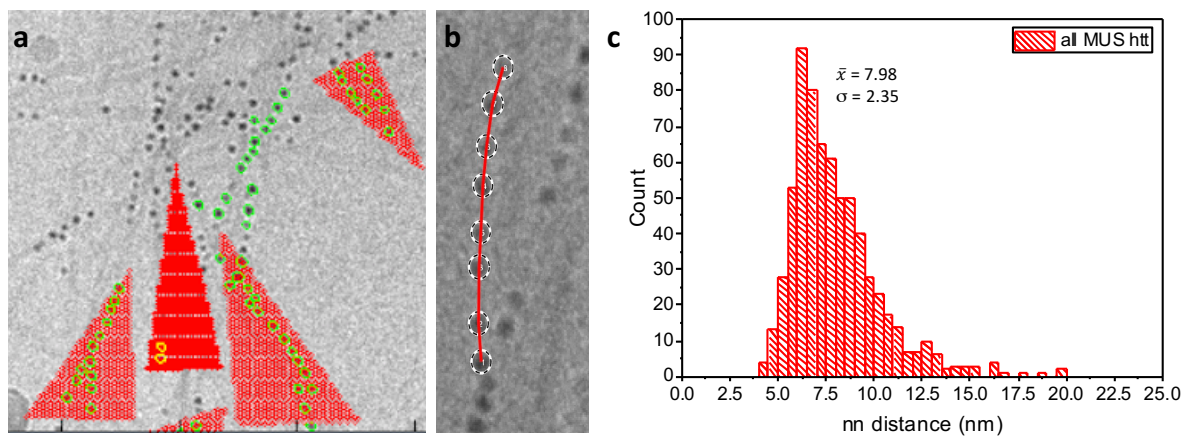


Figure 3.12 Nearest Neighbor measurement proceedings. a) Detecting nanoparticles and calculating their centers with Pebbles software, b) measurement of a distance between given nanoparticles along the edge of an amyloid fibril, c) exemplary histogram showing nearest neighbor distance distribution between allMUS (fraction 2) nanoparticles labelling FL Httex1 43Q fibrils.

Test T

Test T was performed in Microsoft Excel software with use of two-sample equal variance T.TEST function of two tailed distribution.

Chapter 4

Investigating polymorphism of the recombinant and synthetic fibrils with use of the gold nanoparticles

4.1 Introduction

The remarkable propensity of amyloid fibrils to assume a wide variety of morphological types was already reported in 1959 and since then, it became an important and crucial part of amyloid studies (154). Nowadays, our understanding of this subject has expanded and we can draw from the knowledge, which came from various approaches, ideas and usage of a whole variety of analytical techniques. Aside from the morphology itself, other polymorph dependent features like kinetics of aggregation (2), nano-mechanics (for instance elastic, torsional shear and Young's modulus or bending) (3–5) or toxicity (6) were studied on many amyloid fibrils. Our knowledge on the phenomenon of polymorphism grew in the last decades, however, amyloid polymorphism is still not fully understood. This demonstrates the complexity of this phenomenon.

The propensity of amyloids to assume various morphologies was found to depend on external factors, such as aggregation conditions or changes of the ionic strength of the buffer solution (25, 80, 155, 156). Among the morphological variations observed in the amyloid fibrils (that include nanotubes, helical ribbons or crystals), twisted ribbons are the most characteristic and probably encountered most frequently (20, 30, 157). Twisted ribbons are often characterized by their crossover (periodicity) length, that is the distance in which the fibril makes a 180° twist, along its axis. A single sample preparation can contain a population of twisted ribbons with various periodicity lengths (30). Recent theory proposed in 2010, claims that the crossover length is correlated with the fibril width, which corresponds to the number of protofilaments constituting the amyloid fibril (139, 158).

Because of so many factors that can influence the final morphology of the fibrils, systems with amyloids aggregated *in vitro* are extensively used in order to learn more about the polymorphism. The simplicity of these systems allows for the systematic studies with extremely controlled external aggregation conditions. This chapter covers the application of gold nanoparticles as a staining agent for various polymorphic species of amyloid fibrils, with

great emphasis on the twisted ribbons. The polymorphism of synthetic A β_{40} and recombinant R2 amyloid fibrils prepared *in vitro* was studied with the use of MUS:OT and fractionated allMUS nanoparticles. We achieved sufficient decoration of both types of these fibrils which enabled the observation of several different morphologies that were present in the samples such as straight, two- and three-fold symmetry twisted fibrils. This chapter shows how the use of our gold nanomaterial enhances the visualization of amyloid structures, thus allowing the measurement and analysis of the periodicity length and width of twisted fibrils (Figure 4.1). We found direct correlation between these two values, which supports the previously proposed by Adamcik et al. hypothesis that the periodicity length depends on the number of protofilaments constituting the fibril (139).

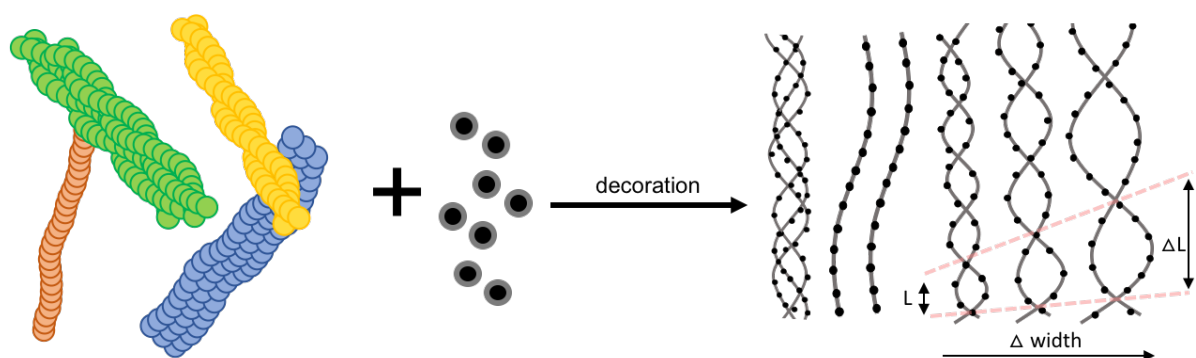


Figure 4.1 Schematic representation of the experimental section of this Chapter, where we label various polymorphic types of amyloid fibrils derived *in vitro* and present the linear dependency between the length (L) and width of the helical twist.

Disclaimer: This chapter is partially derived from a draft of the manuscript, that is now accepted in Proceedings of the National Academy of Sciences (PNAS) entitled “Unraveling the Complexity of Amyloid Polymorphism Using Gold Nanoparticles and Cryo-EM”.

4.1.1 Periodicity of the fibrils as a function of the number of protofilaments

One of the most interesting approaches to study amyloid polymorphism and understand the variances of the periodicity length in the population of fibrils was applied in the work of Adamcik et al. (139). In these studies, the variability of the periodicity length was studied by applying statistical polymer physics analysis to examine different stages of β -lactoglobulin aggregation and periodicity was found to be positively correlated with the height (width) of the fibrils (Figure 4.2) (139, 158).

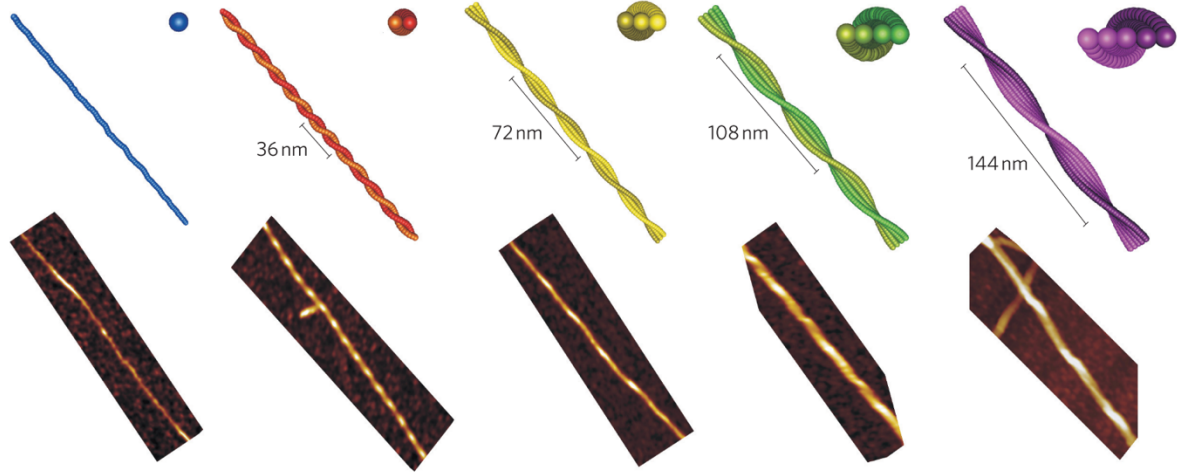


Figure 4.2 Schematic representation of the linear correlation between the periodicity length and number of protofilaments in the amyloid fibril. AFM images of the amyloid fibrils of different height and periodicity length with their coarse-grain molecular dynamic reconstructions show the dependence of the twist length on the protofilament number. Reprinted with permission from (139).

This observation was explained by the hierarchical multistranded self-assembly scheme with the ribbon-like packing scheme. For this, persistence length (l_p) was calculated for each population of different stages of the β -lactoglobulin fibrillation. The calculations were derived from this equation:

$$l_p = EI/k_B T \quad (4.1)$$

Where E is the Young's modulus, I is the area moment of inertia of the polymer cross-section, k_B is the Boltzmann constant and T is the temperature.

Assuming that the fibril is forming a helical ribbon, that consists of n filaments (protofibrils or protofilaments), its height will be equal to $2r_0$ and the width will be equal to $2nr_0$, where r_0 is the radius of the filament. Flattened cross-section of the fibril brings two possible moments of inertia that are corresponding to the possible bending modes of the ribbon and could be calculated in two ways:

$$I \approx r_0 \cdot (nr_0)^3 \quad (4.2)$$

or

$$I \approx (r_0)^3 \cdot nr_0 \quad (4.3)$$

Equation (4.1) shows that l_p is proportional to the energy that is essential for bending the fibril and will follow the lowest energy cost path presented in the equation (4.3), bringing the final l_p formula:

$$l_p \approx nr_0^4 E/k_B T \quad (4.4)$$

The significance of equation (4.4) is evident, since it shows that maximum height (width) and l_p of the amyloid are linearly correlated with the number of the filaments constituting the fibril. Moreover, Adamcik et al., associated the periodicity of the fibril with the number of protofilaments n (139). The filaments are made of smaller building blocks, in this case monomers, that are stacked along the fibril axis and repel each other. Although layers are primary repulsed by each other, they cannot freely rotate to minimize this force because of the elastic energy that favors flat structures. A twisted morphology of the helical ribbon fibril is the result of equilibrium between these two forces that dominate the fibril architecture. The distance with which the proteins in the outside filaments are sheared with respect to each other can be expressed as following:

$$d = (n - 1)(a/2)\theta \quad (4.5)$$

Where a is the center to center distance between the adjacent filaments in the fibril and θ is the angle with which the consecutive layers of monomers on the outside filament are tilted to one another. For the two fibrils constituted of two filaments, θ would be the expressed as:

$$\theta \approx 2(d_{max}/a)/(n - 1) \quad (4.6)$$

Where d_{max} is the threshold distance beyond which the filaments would break.

Each node, that is the distance between the twists in the fibrils, is made of a certain amount of monomer layers m , in the way that

$$\theta m = 2\pi \quad (4.7)$$

Combining equations (4.6) and (4.7) gives the final formula that shows clear correlation between the number of filaments and periodicity:

$$m \approx \pi(a/d_{max})(n - 1) \quad (4.8)$$

For a perfectly relaxed and flat fibril, θ would be equal to 0.

A mature amyloid fibril may be also schematically shown on the chain of beads model, where each bead represents a single monomer (Figure 4.3).

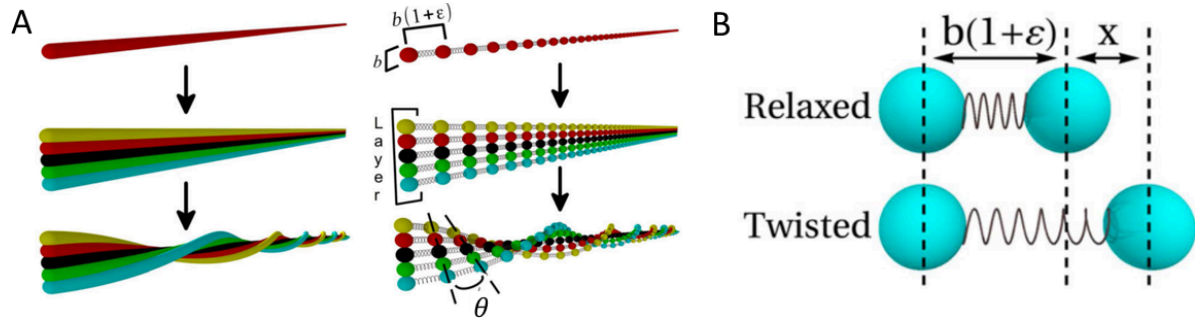


Figure 4.3 A) Steps to the coarse-grained picture of a fibril, where protofilaments are represented by the straight lines that overlap on each other and then twist. B) A single protofilament is represented by the chain of beads. Beads of the protofilaments attached to each other, overlap and create layers m , that later tilts in respect to each other by the angle θ . C) Schematic representation of the distance between the beads in the relaxed fibril where $\theta = 0$ and in twisted fibril, where distance is additionally extended by x . Reprinted and modified with permission from (158).

In this model, beads are distant to each other with a distance $b(1+\varepsilon)$ where b is the diameter of the single filament. The beads are connected with springs which represent the elastic part of the energy. Because of this energy working against the repulsive electrostatic interactions between the beads, two consecutive layers of the fibril will be tilted with respect to each other and the beads of the outer layer would be placed further from each other with distance x (displacement). Given that the displacement distance is expected to be very small when θ angle is assumed to be small, Assenza et al. obtained the formula on the fibril periodicity by calculating how many layers are needed to perform a 180° twist (158):

$$L = b(1 + \varepsilon) \frac{\pi}{A} (3n^2 - 7)^{1/2} \quad (4.9)$$

Where L is the periodicity length, A is a constant that depends on the ionic strength of the solution and n is the number of twisting protofilaments. These calculations show that the crossover distance depends on the number of protofilaments constituting the fibril and our results support this finding.

4.2 Results and discussion

4.2.1 A β ₄₀ analysis

An A β ₄₀ peptide, despite comprising of just 40 amino acids, can self-assemble and form fibrils of different morphologies depending on the aggregation condition. The heterogenous population of the fibrils was also reported in a single sample preparation (26, 30, 74, 78). To investigate the effect of the aggregation conditions on the polymorphic population, the A β ₄₀ fibrils were prepared using two different procedures: with and without agitation. Preliminary negative stain TEM images showed significant difference in the morphology between the two samples as shown in Figure 4.4. Agitated samples contained a lot of short, wide fibrils without clear twist, while samples incubated in the quiescent conditions exhibited long, thin fibrils with a clear periodicity. The same effect was previously observed and described in the literature (74).

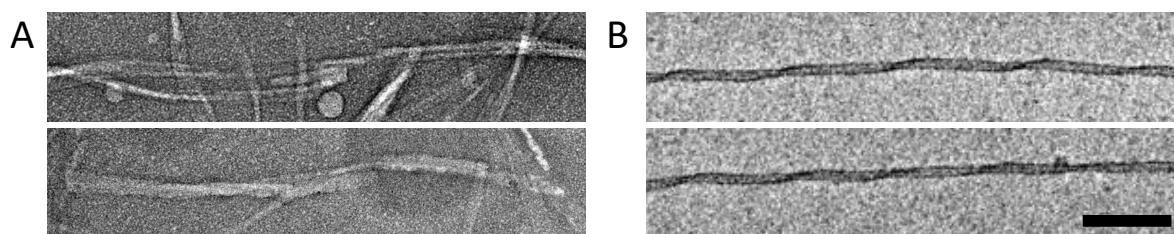


Figure 4.4 Negative stain TEM images of A β ₄₀ amyloid fibrils prepared in the two different ways: A) monomers agitated for 48 h in 37°C fibrillated into short and straight fibrils, while B) monomers that were kept in the quiescent conditions at 37°C for 1 month created long and twisted A β ₄₀ amyloid fibrils. Scale bar is 100 nm.

In order to examine the differences between the two samples under the cryo conditions, an aqueous water solution of MUS:OT nanoparticles was added to each sample and incubated together with the fibrils. The high affinity of the nanoparticles to the fibril edges allows for rapid determination of the differences in the structural polymorph distribution between these two conditions. Cryo TEM images of A β ₄₀ after 72 h of incubation with gold MUS:OT nanoparticles under shaking conditions revealed homogeneously decorated fibrils. Nanoparticles are evenly distributed lining the edges of the fibrils, which increased their contrast under cryo TEM and facilitated their detection on the grid. The fibril edges are easily discerned from the background, allowing for immediate determination of the type of morphological polymorph.

Preferred labeling on the narrow sides of the fibrils can be explained by the mechanism of fibrillation. As proposed by Adamick et al. (139) and shown in the Figure 4.2, the twisted ribbon morphology of the amyloid fibrils is a result of the lateral association of the protofilaments. Ribbon morphology is favored over the cylindrical, due to the interplay

between the hydrophobic and electrostatic interactions. We speculate that the decoration of the edges of twisted amyloid fibrils, is a result of similar mechanism (Figure 4.5).

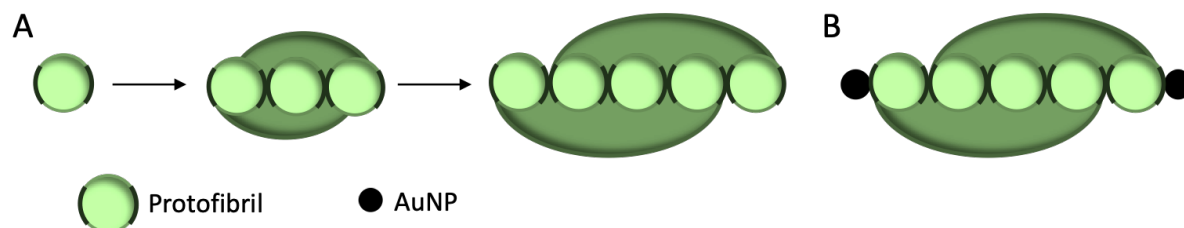


Figure 4.5 Schematic representation of the twisted ribbon fibril cross-sections. A) Lateral association of the protofibrils due to the hydrophobic and electrostatic interactions proposed by Adamcik et al. (139). Black part of the protofibril contour represents region with increased hydrophobicity, which consequently possess higher tendency to self-associate through hydrophobic contact. B) Cross-section of the mature amyloid fibril labelled by the gold nanoparticles through the hydrophobic contact. Not to scale.

We observe that fibrils formed under quiescent conditions are longer and expose a twisted helical symmetry, while those prepared under agitation are shorter and resemble straight ribbons devoid of any visible twist (Figure 4.6 A-B).

Nearest neighbor measurements showed that nanoparticles decorate straight fibrils more closely than twisted fibrils. The mean distance between the centers of adjacent nanoparticles attached to the edge of the straight fibril is equal to 7.8 ± 2.2 nm, while the values for the twisted fibrils were equal to 8.8 ± 3 nm (Figure 4.6 C-D). This result indicates that the distance between two adjacent nanoparticles on the fibril is affected by the geometry of the amyloid.

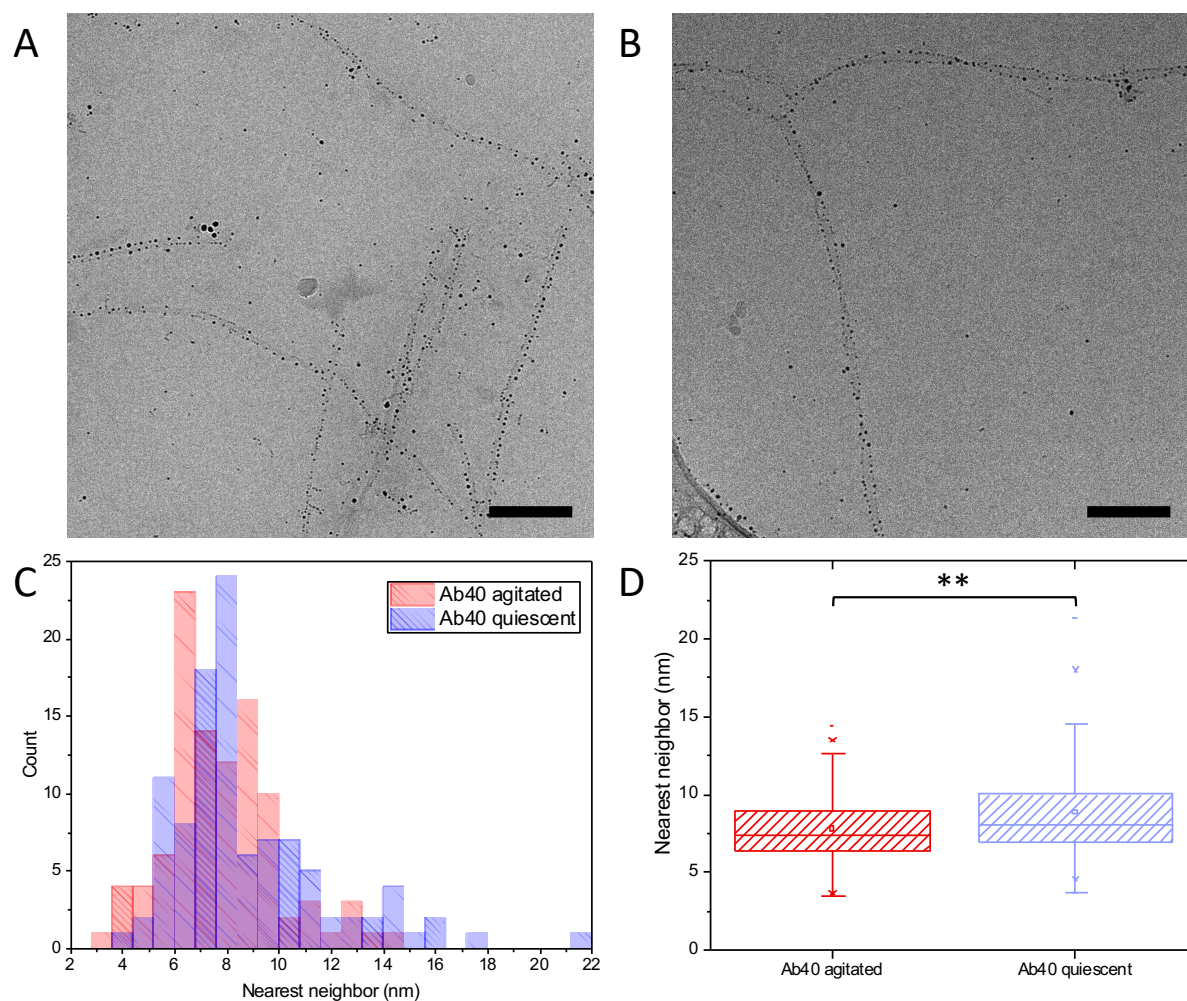


Figure 4.6 Cryo TEM images of Aβ₄₀ amyloid fibrils prepared in two different ways: A) under agitation and B) without shaking. Scale bar is 100 nm. Panels C) and D) depict the nearest neighbor measurement of the nanoparticles labelling the edge of the fibril. C) Histogram with the nearest neighbor distance distribution of the nanoparticles decorating both types of fibrils and D) Statistical analysis of the nearest neighbor results, that show that the difference in the density of the decoration between two types of fibrils is statistically significant.

Moreover, cryo TEM images showed the presence of long and twisted fibrils of different periodicity in the sample containing Aβ₄₀ fibrils aggregated in the quiescent conditions (Figure 4.7 B-C). Nanoparticle labeling facilitated the measurement of the crossover length distribution of the two-fold twisted fibril population, allowing image analysis and quantification of the morphological parameters of the fibrils (Figure 4.7).

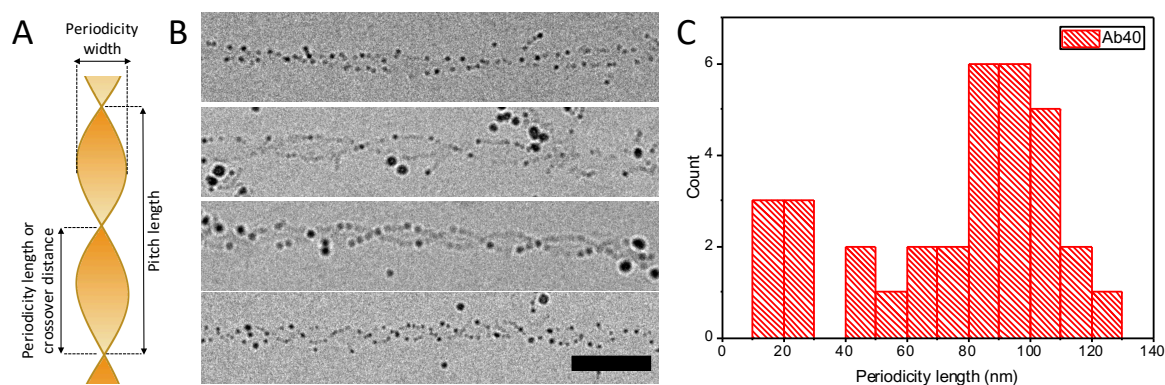


Figure 4.7 Analysis of the periodicity length of the A β ₄₀ fibrils prepared in the quiescent conditions. A) a schematic representation of the fibril characteristics such as periodicity length (crossover distance) and width and pitch length. B) Cryo TEM image of A β ₄₀ fibrils present in the sample with different periodicity length. Scale bar is 50 nm. C) Periodicity length distribution in the analyzed sample.

Comparative studies of recombinant amyloid fibrils between different research groups are challenging, since so many details regarding the aggregation conditions influence greatly the final morphology of the fibrils. However, as in our case, several groups found A β ₄₀ fibrils of different morphologies in the same sample preparation (30, 31). The variability in the periodicity length of A β ₄₀ fibrils was also reported and measured previously as described in the literature. However, due to the great susceptibility of the aggregation process to external factors, results varied considerably between the groups, making it hard to compare them with our own (30, 159, 160).

On very rare occasions, A β ₄₀ three-fold symmetry fibrils were spotted. Alas, their number was not sufficient to perform further analysis and their appearance was difficult to predict or control (Figure 4.8). This kind of extremely rare fibrils were found among predominant fibrils of two-fold symmetry that were first aggregated in the quiescent conditions and then incubated with the fractionated allMUS nanoparticles for 24 h under very strong shaking (1000 rpm). Our results resemble the results obtained by Tycko and coworkers, where a detailed description of A β ₄₀ amyloids, displaying two- and three- fold symmetry of these fibrils, was reported (25).

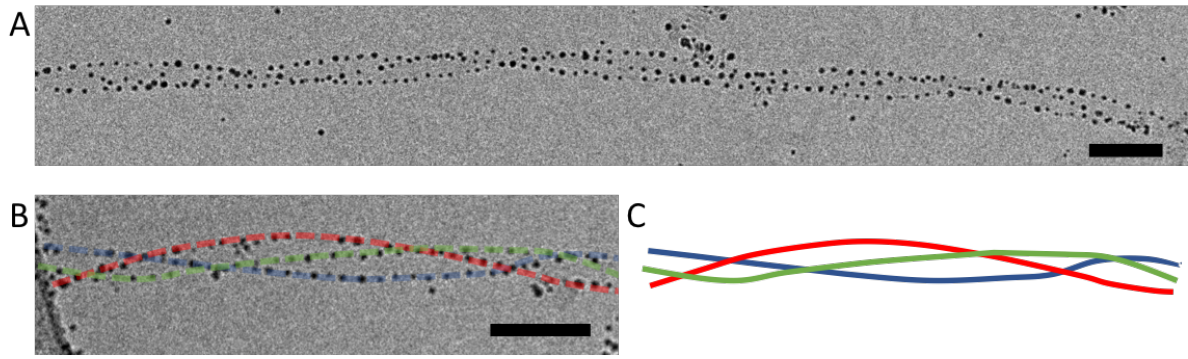


Figure 4.8 A) Rare A β_{40} three-fold symmetry fibrils found among the predominant two-fold symmetry fibrils. B) A β_{40} three-fold symmetry fibril with the lines that follow nanoparticles arrangement on the fibril surface and C) the same lines subtracted from panel B) that show the pattern on the fibril in the more clear way. Scale bars are 50 nm.

4.2.2 R2 analysis

R2 is a small peptide motif localized in the second microtubule binding domain of tau protein and contributes in the β -sheet formation during misfolding of this protein (161). R2 peptide has a remarkable ability to self-assemble into a wide variety of polymorphs (162, 163). Negative stain TEM images showed that R2 fibrils in a single sample preparation can morphologically fall into three major group of polymorphs: (I) straight and thin, (II) thin and curly and (III) wide and twisted (Figure 4.9).

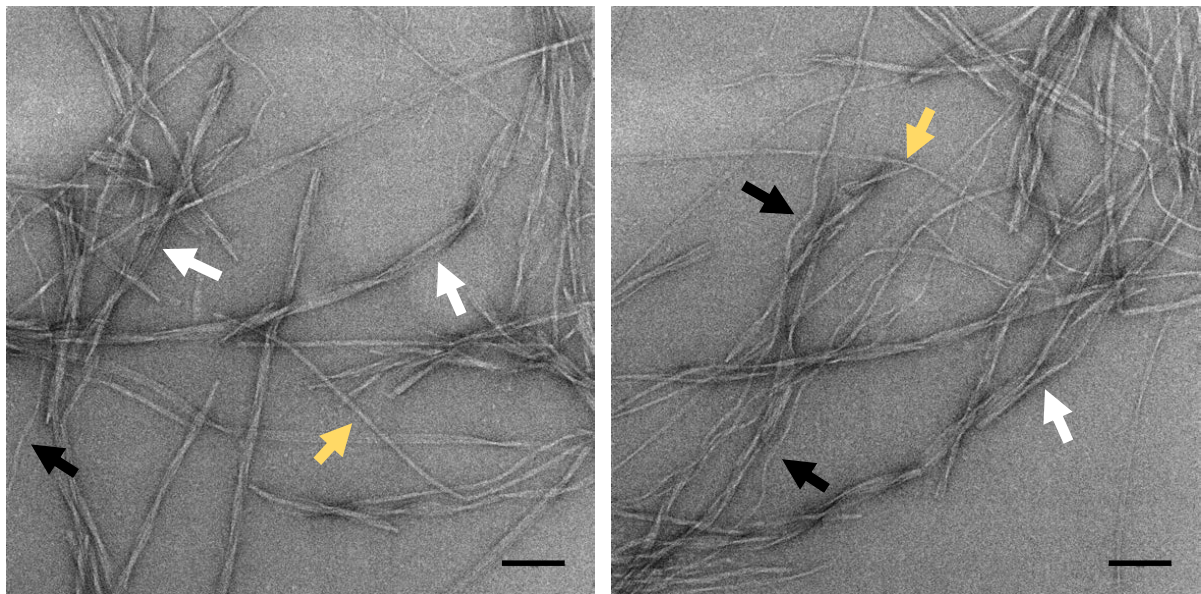


Figure 4.9 Negative stain TEM of mature R2 fibrils of various morphologies. White arrows are pointing on the wide and twisted fibrils, yellow arrows show straight and thin fibrils and black arrows points on the thin and curly fibrils. Scale bars are 100 nm.

To determine if the MUS:OT nanoparticles could bind and label R2 fibrils, we incubated them with fibril solution and performed cryo TEM measurements. MUS:OT nanoparticles adsorbed selectively to the different tau peptide fibril polymorphic types: wide fibrils with a clear twist

were densely decorated, while smooth and thin fibrils were not decorated by the nanoparticles. This manner of labelling did not change even after prolonged incubation times with nanoparticles (Figure 4.10).

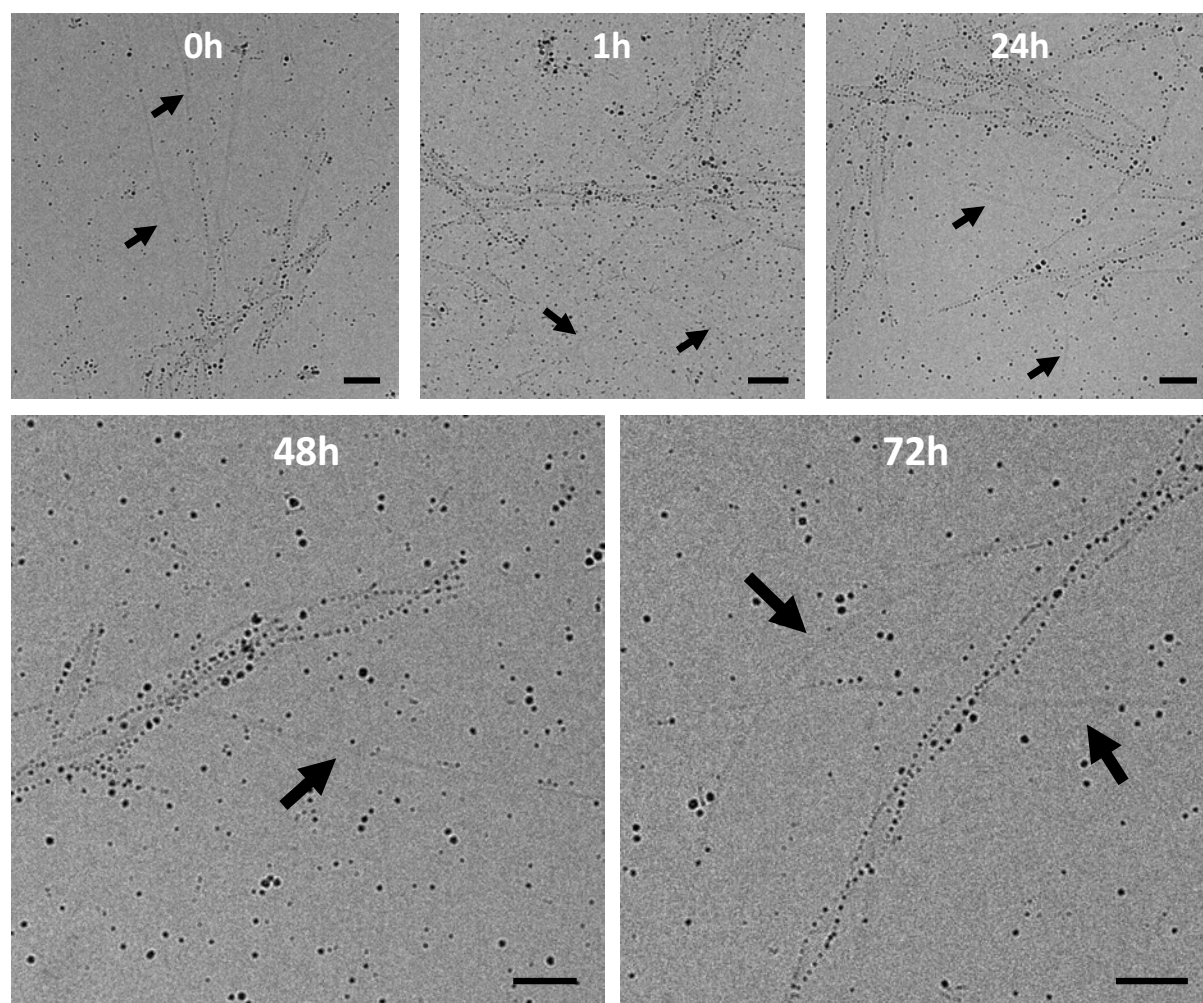


Figure 4.10 Cryo TEM images presenting the time assay of the R2 incubation with MUS:OT nanoparticles. Free and unbound nanoparticles are visible in the ice as well as bare and not decorated fibrils showed by black arrows. Scale bars are 50 nm.

The same effect was observed with higher ratios of MUS:OT (0.2 mg/ml and 0.3 mg/ml in the final solution from initial concentration of 0.1 mg/ml) and fractionated allMUS (0.4 mg/ml and 0.6 mg/ml in the final solution from initial concentration of 0.2 mg/ml) nanoparticles to fibrils. Bare amyloids and free and unbound nanoparticles were visible in the glassy ice, indicating that the distinct labeling patterns correlate with the different fibril surface properties rather than the incubation conditions (Figure 4.11). The lack of decoration of certain polymorphic species, may elucidate the surface propensities of fibrils that remain undecorated. For example, this kind of polymorphs could be folded in a different way, which exposes less attractive domains for the nanoparticles on the outside and buries more attractive regions inside the fibril.

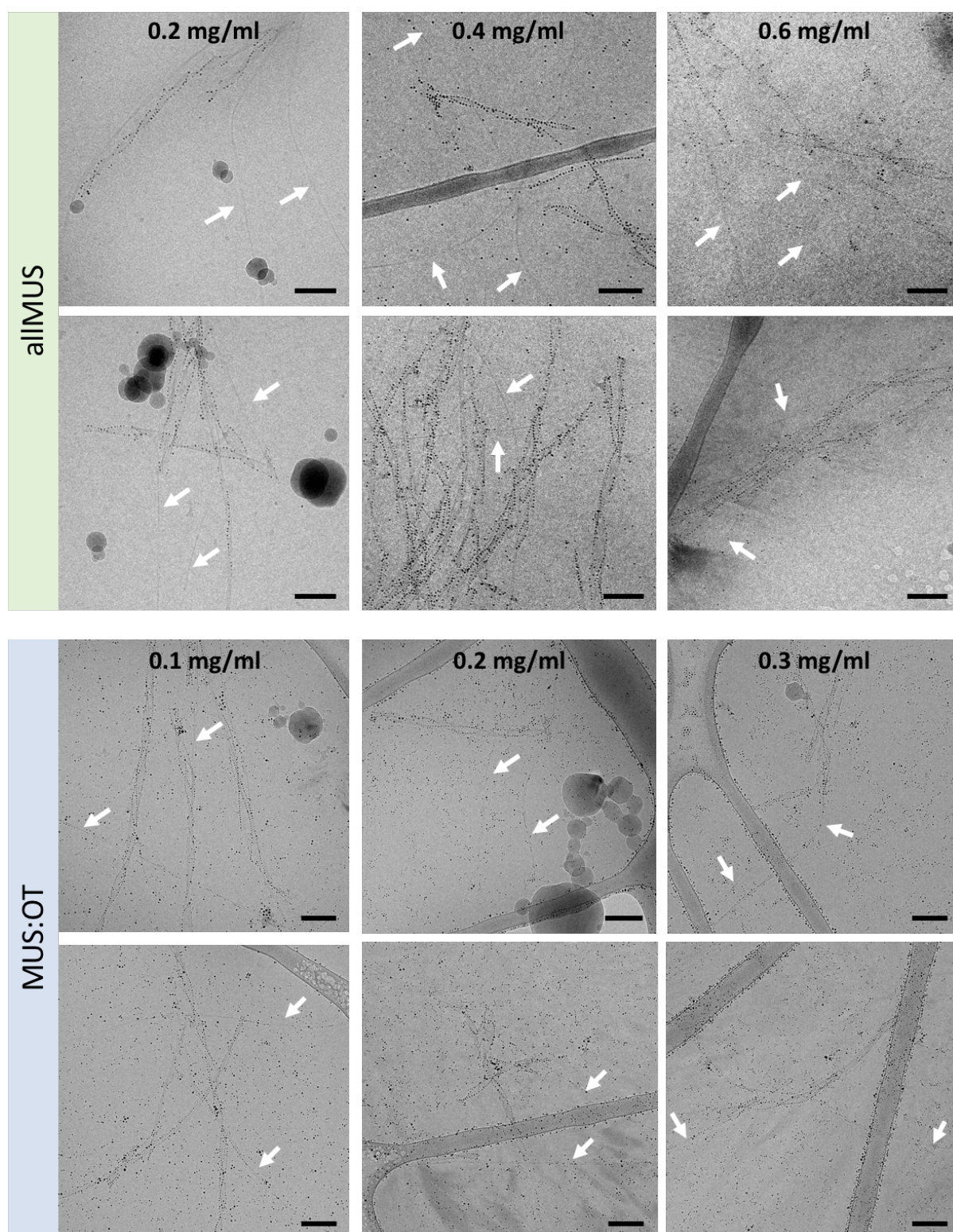


Figure 4.11 Cryo TEM images depicting results from the concentration assay of R2 fibrils incubated with MUS:OT and allMUS nanoparticles. The numbers indicate final concentration of the nanoparticles in the sample, White arrows are pointing on the fibrils that remained bare after 48 h of incubation with nanomaterial. Scale bars are 100 nm.

Furthermore, within the labeled amyloid fraction, many polymorphs could be differentiated: (I) straight, (II) clear three-fold symmetric structures and (III) a whole range of two-fold twisted fibrils with different periodicity (Figure 4.12 A-B).

Nearest neighbor measurement showed similar results as obtained for A β ₄₀ fibrils. The twisted fibrils were decorated more loosely than straight fibrils. In the case of the twisted R2 fibrils the average center to center distance between the nanoparticles attached to the edge of the fibril was equal to 5.9 ± 1.6 nm. These values for the twisted fibrils were 6.3 ± 1.6 nm. (Figure 4.12 D-E). The measurement was performed on the same sample solution, which contained both analyzed populations. This ensured the same conditions between the analyzed species.

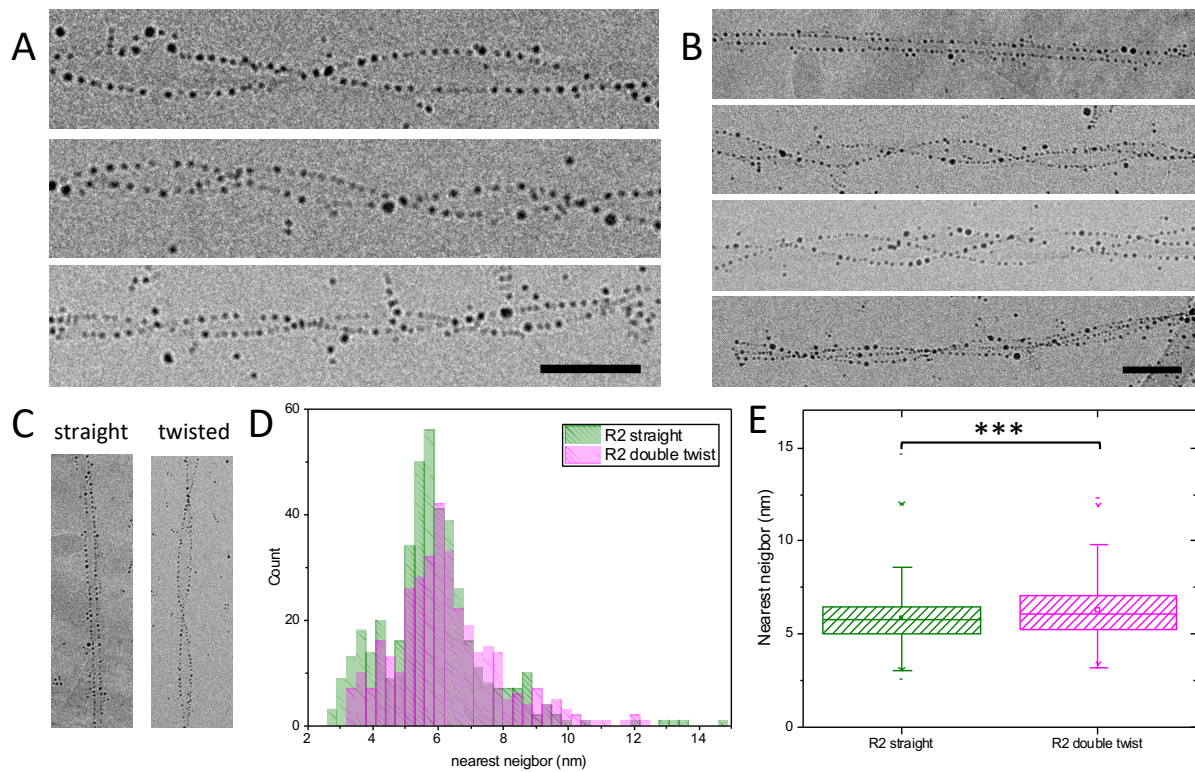


Figure 4.12 Cryo TEM images of the cropped R2 fibrils that presented various morphology and nearest neighbor measurements of decorating nanoparticles. A) Two-fold symmetry fibrils of different pitch length, B) overview on the polymorphic forms present in the studied sample that ranged from simple straight fibrils to more complex three-fold symmetry fibrils. Scale bars are 50 nm. C) Magnified fibrils that represent two separate populations of R2 polymorphs that were analyzed by nearest neighbor measurements. D) Histogram with nearest neighbor distances between the nanoparticles decorating straight and twisted R2 fibrils. E) Statistical analysis of the nearest neighbor distance results, that show that the difference in the density of the decoration between two types of fibril is statistically significant.

Both of the fibrils, A β ₄₀ and R2, demonstrated a correlation between the length of the pitch and the thickness of the fibril (Figure 4.13). This is in agreement with the previous hypothesis of the correlation between the number of protofilaments in the amyloid fibril and the pitch length (158).

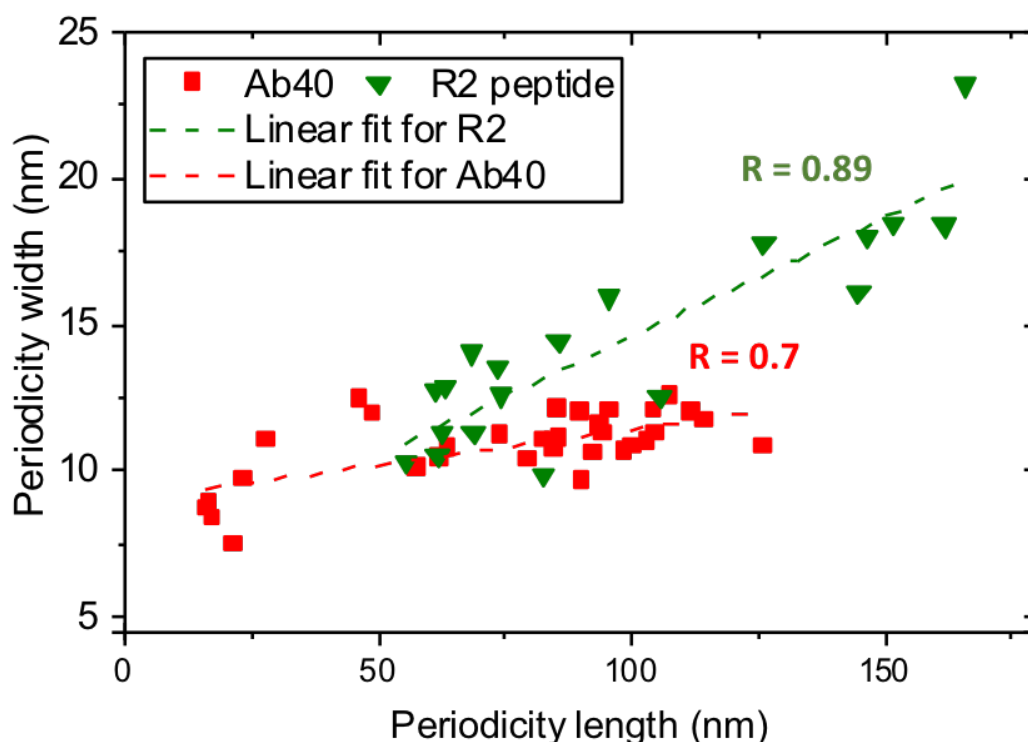


Figure 4.13 Plot showing correlation between the periodicity length and periodicity width of A β ₄₀ and R2 fibrils. One dot represents the mean values obtained for one fibril.

Moreover, we observed that the time of labelling strongly depends on the amyloid type (e.g. amyloids made from the R2 protein are getting decorated much faster than A β ₄₀). Shaking of the sample enabled continuous movement of all of the elements in the sample and gave momentum to the nanoparticles, that greatly improved the decoration. We determined that the optimal shaking speed is in the range of 300 rpm - 600 rpm. Slower rotation was not efficient and higher speed would imperil the breaking of the fibrils.

4.3 Conclusion

The use of nanoparticles alleviates the challenges that derive from common cryo TEM sample defects, such as thick or not perfectly vitreous ice. The particles have shown to be effective in labelling polymorphic parts in the case of the studied fibrils. Several different populations of morphological polymorphs, present in the same sample, were detected. Among straight fibrils that were decorated only at the edges, which pronounced their ribbon like structure, two-fold twisted fibrils with various pitch lengths were observed. We also show, how density of the nanoparticle decoration depends on the geometry of the fibril. Nearest neighbor measurement showed that nanoparticles have a tendency to sit closer to each other on the straight fibril than on the twisted one. Moreover, nanoparticle decoration enabled also visualization of a few, very

rare A β ₄₀ three-fold symmetry fibrils. In the case of R2 amyloids, several thin fibrils that did not seem to be decorated at all were observed even with increased time of incubation and nanoparticle concentration. We were also able to easily assess the differences between the A β ₄₀ fibrils aggregated under different conditions such as agitated and quiescent. With regard to both of the tested nanoparticle types, MUS:OT and fractionated allMUS, we were able to successfully decorate the majority of the amyloid fibrils. The results enabled the analysis of the pitch and width of the fibrils that seem to support the theory proposed by De Los Rios (158), which assumes that the periodicity of the fibril is closely correlated with the width of the amyloid.

4.4 Materials and methods

Nanoparticles

Nanoparticles were prepared and characterized in the same way as described in Chapter 3.

A β_{40} fibrils

A β_{40} samples were prepared according to the previously reported protocol (164). A β_{40} was purchased from ChinaPeptides. The lyophilized material was dissolved in a 1:1 mixture of 0.1% NH₄OH and 100 mM Tris buffer (with 0.02% NaN₃ and at pH 7.4) at approximately 1 mg/ml. The solutions were ultracentrifuged for 1 h at 366941 RCF (g) at 4°C in a Beckman ultracentrifuge. The upper half of the supernatant was collected, and the peptide concentration was determined using its extinction coefficient at 280 nm (1490 M⁻¹cm⁻¹). A Perkin Elmer UV-Vis was used to perform these measurements. The supernatant was then diluted to 50 μ M concentration with PBS (pH = 7.4 and 137mM NaCl). Fibrils used for the periodicity length analysis were grown inside 1.5 ml Polypropylene Eppendorf tubes in quiescent conditions at 37°C while the rest of the A β_{40} fibrils were grown under 600 rpm shaking.

R2 peptide

The tau-derived R2 peptide 275 – VQIINKKLDLSNVQSKCGSKDNIKHV – 300, (numbering according to human tau isoform 2) was purchased from CisBio. R2 amyloid fibrils were prepared by incubating 100 μ M of the R2 peptide in the presence of 1:4 (mol:mol) of heparin in 10 mM phosphate buffer pH 7.4, 50 mM NaF and 0.5 mM freshly dissolved DTT at 37°C under quiescent conditions for at least 12 h. Fibrils were prepared by Dr. Nadine Ait - Bouziad.

Incubation of the amyloid fibrils with nanoparticles

Mature amyloid fibrils, prepared as described above, were dispersed in their corresponding buffer and incubated at 37°C in a thermomixer with a water solution of NPs. The samples were incubated for the period of 24 h to 72 h under shaking speed in the range of 300 rpm-600 rpm. At the end of the incubation, samples were gently resuspended using a pipette to generate some agitation immediately prior to cryo grid preparation.

Cryo electron microscopy of amyloid and nanoparticle samples

For cryo TEM microscopy, a 3 μ l droplet of sample containing amyloids and nanoparticles suspended in buffer was deposited onto a lacey carbon film (Electron Microscopy Sciences) and blotted to a thin (100-300 nm) layer of liquid that was flash frozen in liquid ethane using an FEI Vitrobot Mark IV. Imaging was performed using a Gatan single tilt cryo holder operated on an FEI Tecnai Spirit BioTWIN 80 kV transmission electron microscope in LowDose Mode to visualize the samples at an average exposure of 1-3 electrons/ \AA^2 on a Ceta camera.

Nearest neighbor measurement

Nearest neighbor measurements were performed as described in the 4th Chapter.

Test T

Test T was performed in Microsoft Excel software with use of two -sample equal variance T.TEST function of two tailed distribution.

Fibril crossover distance and width analysis

Micrographs of the amyloids decorated with NPs were analyzed using ImageJ software, where the crossover distance of the fibril was measured manually. For each fibril, the average crossover distance and width were calculated and plotted in the graphs using OriginPro software. In the case of the human-derived samples, 73 AL amyloid fibrils were evaluated from 40 acquired images, and 18 nPHF fibrils were measured on 18 micrographs. Recombinant sample data were obtained from 20 R2 fibrils spotted on 16 micrographs and 33 A β_{40} amyloids visible on 26 images.

Chapter 5

Morphological analysis of human derived amyloids

5.1 Introduction

Chapter 4 showed how gold nanoparticles can facilitate morphological studies of amyloid aggregates formed *in vitro*. These simplified systems are of great use, not only for studying how the various conditions influence the morphology of the fibrils, but also to study different propensities of specific polymorphs. Despite the great versatility of the *in vitro* generated systems, they often lack medical relevance and usually only mimic some of the physiological conditions, such as temperature or pH, of the growing amyloid fibrils' environment.

Contrary to these systems, amyloid formation *in vivo* is guided by complex interactions and conditions that are defined by the cellular or extracellular milieu (82) and are difficult to replicate in cell-free systems. The interior of a cell, as well as extracellular matrix, is crowded with macromolecules that leave little available space. Moreover, living systems are equipped with chaperones and clearance mechanisms. Apart of that, there are also several other subtle features in the living tissues, such as specific pH or presence of specific ions, that can affect the amyloid formation process (165). Recent studies show, that A β amyloids derived from the brain of patients affected with AD, differ significantly from the same fibrils obtained *in vitro* (36, 166). Results obtained by Kollmer et al., showed that fibrils derived from human tissue fell into three major polymorphic populations, but each of them had different peptide fold and handedness from their *in vitro* analogue (166). Comparable results were presented in 2013 by Lu et al., where not only differences between *in vivo* and *in vitro* prepared A β fibrils were reported, but also polymorphic differences in the fibrils between patients and their clinical course of AD (36). Similar observations were made with protein tau. Tau filaments prepared *in vitro* with the use of the conventional method, that involves the use of heparin, were dissimilar from brain-derived filaments (167). These results suggest, that the principles of amyloid fibrils occurrence in the tissue and their final morphology are different from the ones present in simplified *in vitro* systems. This highlights the importance of studying *ex vivo*, rather than *in vitro* derived amyloid fibrils, for deeply investigating the link between disease outcome and amyloids.

We sought to determine whether our nanoparticles could be effective as a contrast agent for human-derived samples under cryo TEM. To achieve this goal, we used protein tau native paired helical filaments (PHFs) from brain of a patient affected by AD, amyloid fibrils of an immunoglobulin λ light chain from the heart of a patient suffering from AL amyloidosis and two types of TTR protein with V30M mutation, derived from patients suffering from transthyretin amyloidosis (ATTR). We incubated PHFs and immunoglobulin λ light chain fibrils with MUS:OT nanoparticles. The TTR amyloids were decorated with fractionated allMUS nanoparticles in order to reduce aggregation of the fibrils. All of the three types of the studied proteins were found to create polymorphs, which makes them perfect candidates to test our nanomaterial as an amyloid morphology marker for *ex vivo* obtained material (28, 33, 168). This chapter shows that MUS:OT and fractionated allMUS nanoparticles efficiently label *ex vivo* amyloid fibrils with an image quality comparable to that achieved for amyloids obtained *in vitro*. The second part of this chapter focuses on the morphological comparison between the *ex vivo* and *in vitro* obtained fibrils shown in Chapter 4 (Figure 5.1). Our findings are consistent with emerging data pointing to the physiological milieu as the key determinant of amyloid fibril strains.

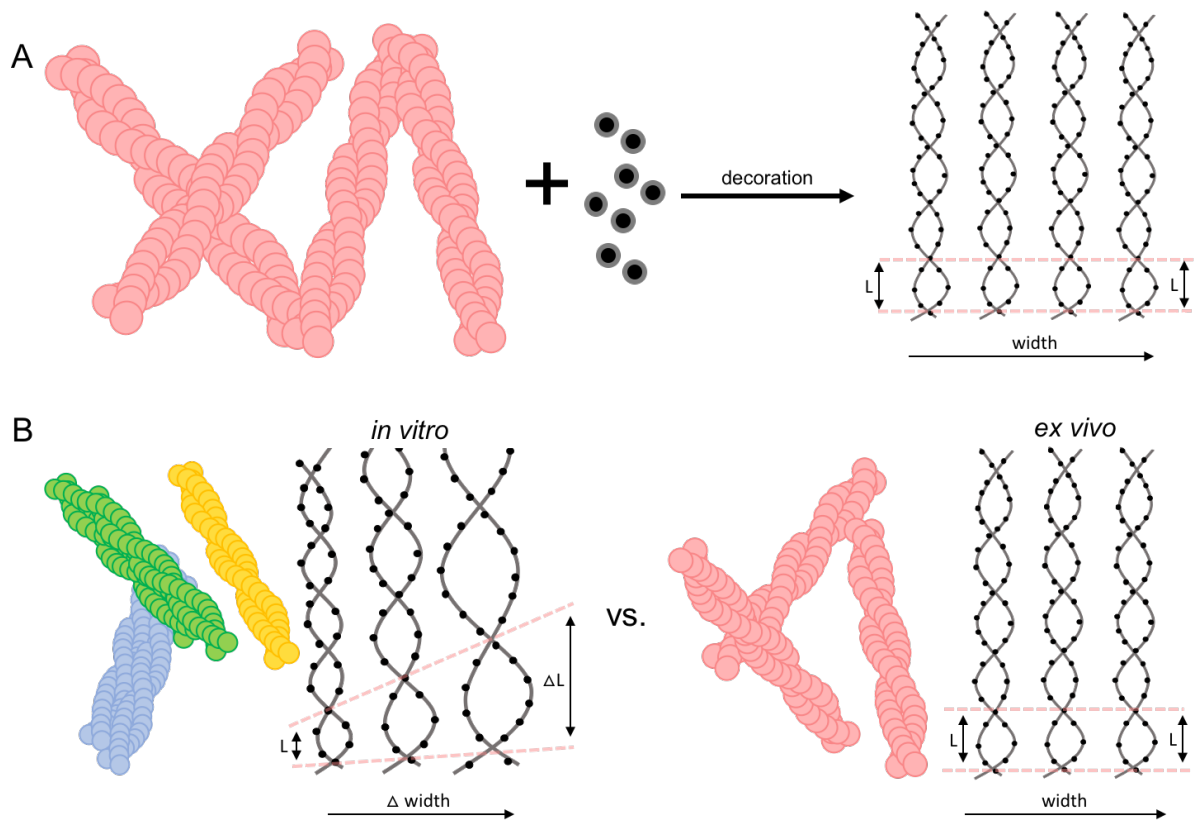


Figure 5.1 Schematic representation of the experimental part of this Chapter, which (A) demonstrates morphological uniformity of the examined fibrils derived *ex vivo* and (B) compares the morphology (length and width of the twist) between the *in vitro* and *ex vivo* obtained fibrils.

Disclaimer: This chapter is partially derived from a draft of the manuscript, that is now accepted in Proceedings of the National Academy of Sciences (PNAS) entitled “Unraveling the Complexity of Amyloid Polymorphism Using Gold Nanoparticles and Cryo-EM”.

5.2 Results and discussion

Tau protein may exist in six isoforms in the human brain and is natively unfolded, however one of the key markers of AD are filaments of this protein (169). Tau filaments are found in two types of inclusions – paired helical filaments (PHFs) or straight filaments. It was shown, that the purified tau from both of these inclusions, had different structure even when it was derived from a single AD suffering patient. These dissimilarities stem from the different interactions between the protofilaments that compose the final fibril (28, 32). Tau filaments also assume different conformations in two different dementia related disorders – AD and Pick’s disease, where different isoforms are found to be involved in the inclusions found in each disease (28).

We incubated enriched PHFs samples derived from an AD post-mortem brain with MUS:OT gold nanoparticles. It is important to note that this sample still contained other non-amyloidogenic elements such as cell debris, proteins and other biological contaminants. Cryo TEM images indeed revealed the presence of many biological structures (Figure 5.2) that were entangled with MUS:OT nanoparticles.

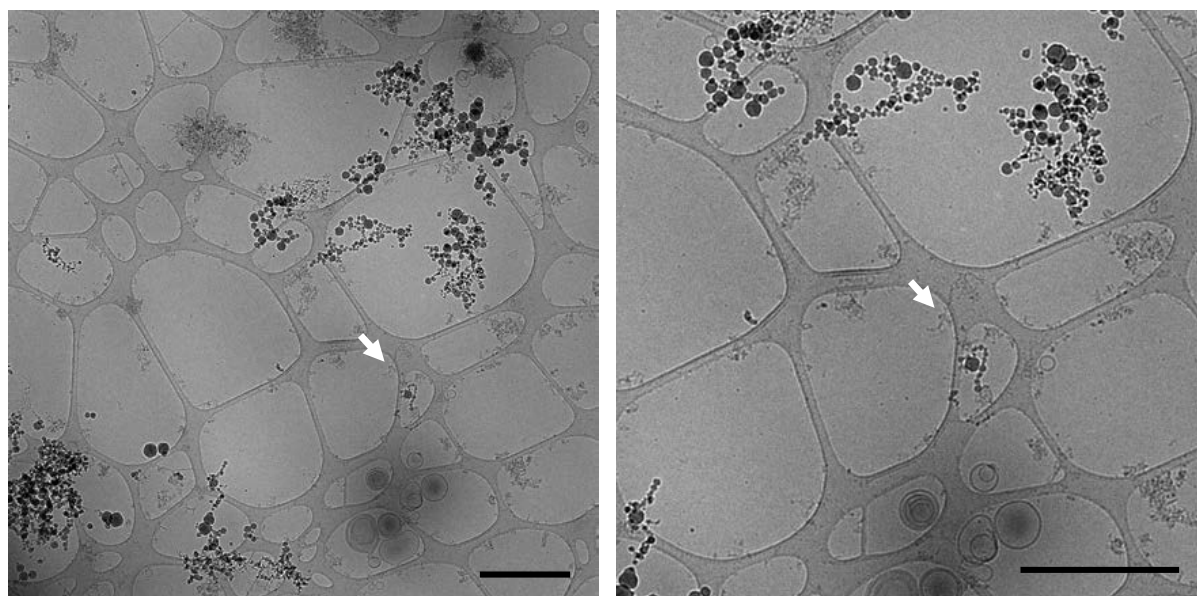


Figure 5.2 Cryo TEM images of the PHFs sample with various cell impurities. White arrows are pointing at the PHFs fibril decorated with MUS:OT nanoparticles. Scale bars are 1 μm .

PHFs were readily distinguishable from contaminants, due to the contrast provided by the nanoparticles explicitly highlighting their characteristic fibrillar shape – a rather uniform and twisted fibrils, that were no longer than 500 nm (Figure 5.3).

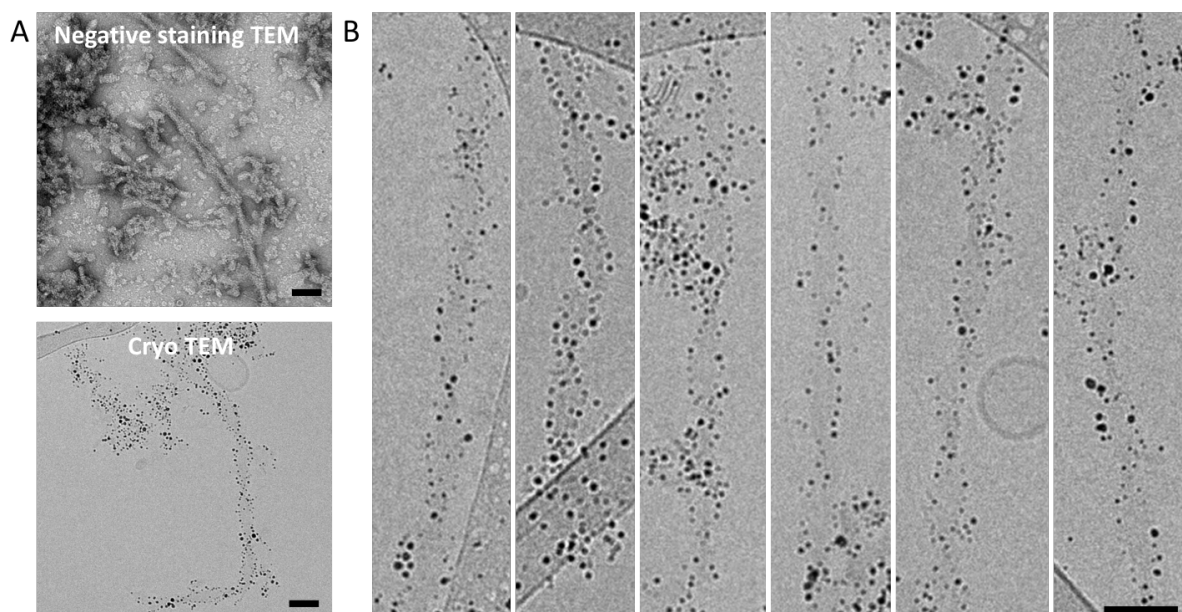


Figure 5.3 Nanoparticle decoration of PHFs fibrils. A) Comparison between negative stain TEM image of bare PHFs and cryo TEM images of PHFs amyloids decorated with the MUS:OT nanoparticles. B) Compilation of the magnified *ex vivo* derived PHFs fibrils labeled with MUS:OT nanoparticles. Scale bars are 50 nm.

Similar data were obtained from the investigation of immunoglobulin λ light chain amyloids. The amyloids were isolated from the heart of a patient suffering from systemic AL amyloidosis. This disease is characterized by extracellular deposition of amyloids in various tissues (55). AL amyloidosis is a nonneuropathic systemic amyloidosis that occurs as a result of abnormally high levels of immunoglobulin light chains not complexed with the heavy chains in the blood (170). Previously published results showed that AL fibrils can fall into more than one morphological group in a single patient and their structure can slightly differ between patients (33). It was also found that AL amyloid fibrils display similar morphology in the same patient regardless of the extraction tissue area (168).

Cryo TEM images depict rather uniform and densely decorated amyloid fibrils, with undoubtedly visible fibril twists. This feature was specifically pronounced by the presence of nanoparticles, since on the negative stain TEM imaging or cryo TEM images of bare λ light chain amyloids, the crossover was not as evident (Figure 5.4).

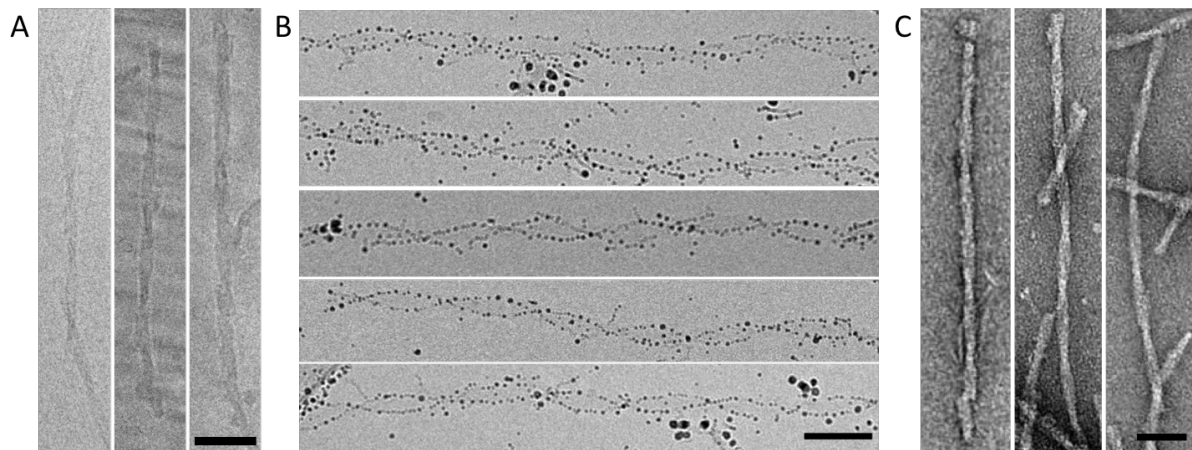


Figure 5.4 Nanoparticle decoration of AL fibrils. A) Compilation of cryo TEM images of bare AL amyloid fibrils. B) Compilation of cryo TEM images of AL amyloid fibrils labeled with MUS:OT nanoparticles. C) Magnified bare AL fibrils imaged by negative stain TEM. All scale bars are 50 nm.

For both samples, nanoparticles demonstrated a striking specificity towards the edges of the amyloid fibrils and highlighted their delimitation, which allowed for a more detailed observation of their morphology and fibrillar characteristics.

Another type of the studied *ex vivo* derived protein, was transthyretin (TTR). TTR is linked with several systemic amyloidogenic diseases that can be sporadic or hereditary. There are more than 100 mutations of this protein, which could lead to misfolding intermediates. The substitution of methionine with valine at position 30 (V30M) is the most globally frequent (19, 171). Studies made on *ex vivo* extracted TTR amyloids, have shown that one patient can develop more than one morphological type of these fibrils in the heart tissue (33).

For the purpose of our analysis two types of TTR amyloid fibrils were examined: type A and type B. Both of these types were carrying a V30M mutation but they displayed different morphology while studied under the negative stain TEM. Type A fibrils were short, with uniform fibril width of ~10 nm and presented lack of a clear twist, type B fibrils were long and devoid of any visible twist (Figure 5.5).

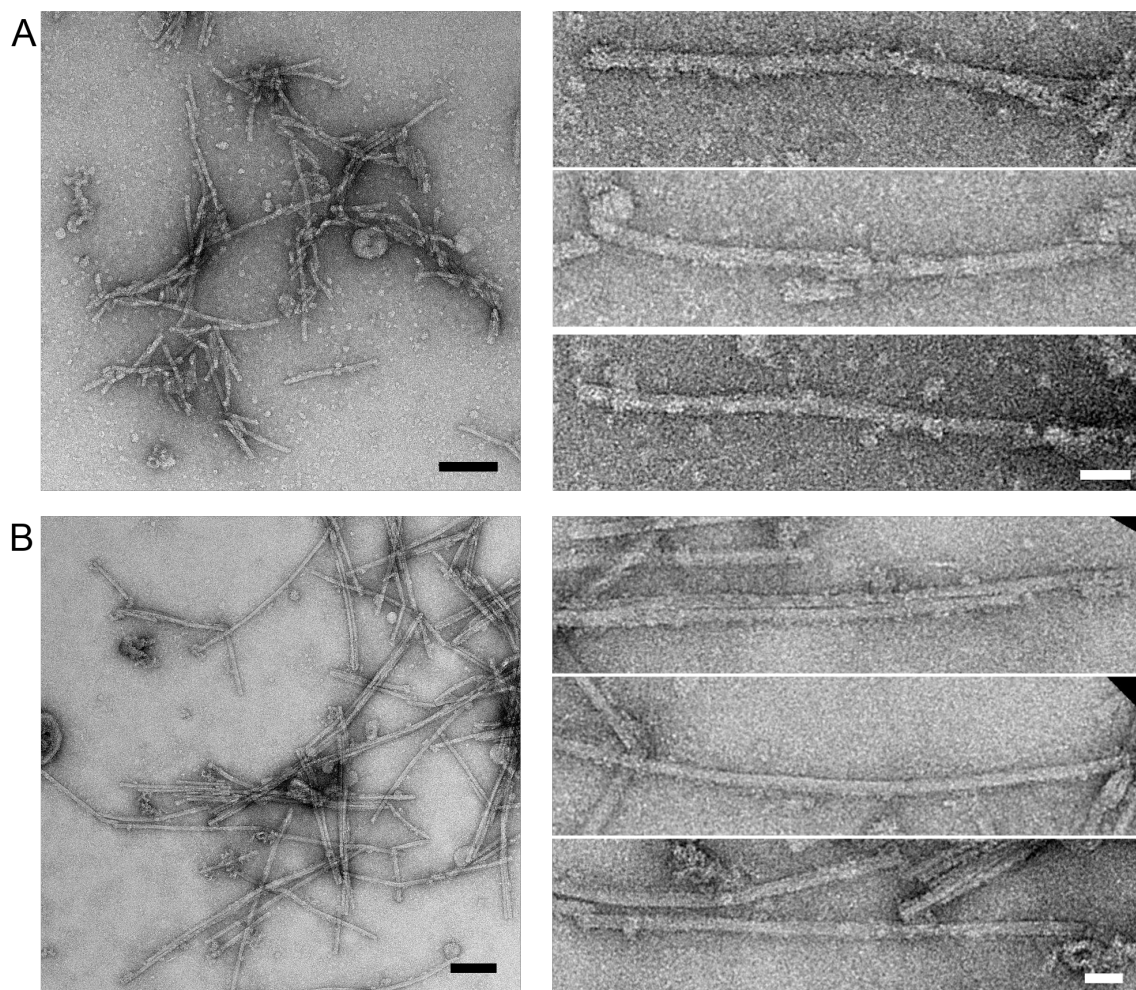


Figure 5.5 Negative stain TEM images showing A) type A TTR fibrils and B) type B TTR fibrils. The right panels show compilations of magnified fibrils of corresponding type. Black scale bars are 100 nm and white scale bars are 25 nm.

Both types of TTR amyloid fibrils created aggregates after incubation with MUS:OT nanoparticles. This occurrence prevented the analysis of their morphological structure. This effect was obviated by the use of fractionated allMUS nanoparticles. Cryo TEM images of both types of labelled fibrils confirmed morphological features visible on the negative stain TEM images. Fractionated allMUS nanoparticles decorated the edges of the TTR type A and type B fibrils pronouncing the twist of the first ones and highlight the straight structure of the latter. Nanoparticles emphasize the twisted morphology of the type A TTR fibrils in comparison with the negative staining images. The curvature of the fibrils was easily followed by the nanoparticles delineating the helical contour (Figure 5.6 A). TTR fibrils of A type were mostly labelled only on one edge, due to their thinness with respect to the average nanoparticle diameter. However few fully labelled nodes, with the width value that was corresponding to the width that was observed on the negative stain TEM images, were identified. We refer to them as single fibrils with thin node (I). On sporadic occasions, wide nodes of TTR fibrils A were noticed. Their width corresponds to the doubled width of single fibrils, therefore we

assume that these are assemblies of two intertwining single fibrils labelled from one side. We refer to them as double assemblies with wide node (II) (Figure 5.6 C).

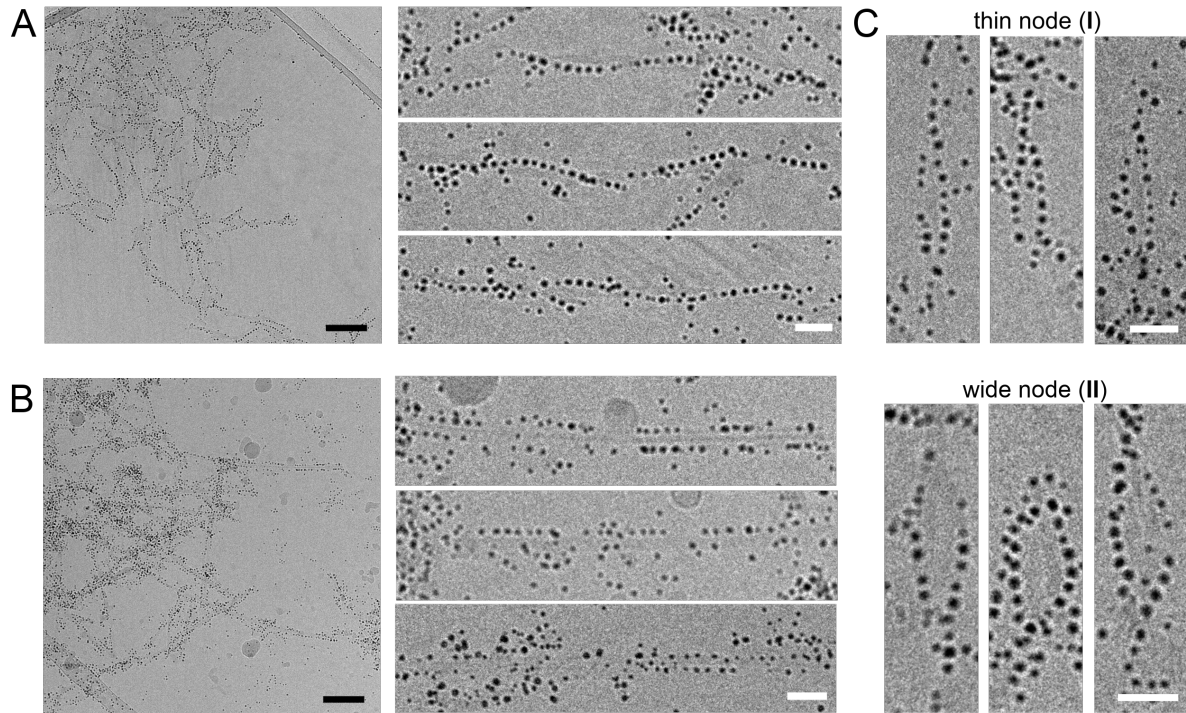


Figure 5.6 Cryo TEM images of the TTR type A and B fibrils labeled with fractionated allMUS nanoparticles. A) Cryo TEM images of TTR type A fibrils. Right panel shows a compilation of magnified fibrils labelled from one side with nanoparticles that unravel their twisted morphology. B) Cryo TEM images TTR type B fibrils. Right panel shows a compilation of magnified TTR type B fibrils decorated with allMUS nanoparticles that pronounces their straight morphology. C) Magnification of two types of nodes found in TTR type A fibrils. Black scale bars are 100 nm, white scale bars are 25 nm.

Efficient labelling of the fibrils with the nanoparticles allowed for the measurements of periodicity length and width of each *ex vivo* obtained sample (Figure 5.7). Standard deviation of the λ light chain amyloids periodicity length is significantly smaller than the standard deviation of the same feature of nPHF and TTR type A fibrils. λ light chain fibrils are longer and the number of twists that contributed to the average value was the highest among all the three types of studied *ex vivo* derived fibrils. The large standard deviation of the periodicity length in the case of TTR type A fibrils is also a result of the existence of two types of nodes that were taken into account during the analysis. Periodicity length distribution was rather smooth and it was not possible to separate the values in two distinct groups, which affected the final result of the analysis. However, measurements of the periodicity width of the TTR type A fibrils showed distinctly two populations of single fibrils with the thin node (I) and higher assemblies of fibrils (II). The average width of the nodes I was 12 nm and the average width of the nodes II was 21 nm, which roughly corresponds to the doubled width of nodes I. Apart from that, TTR type A fibrils are very short and only one twist per fibril was available for the measurements. This precluded the calculation of the average values, which was done for the

two previous *ex vivo* derived amyloids and pronounced possible measurement errors, that could stem from e.g. slanting orientation of the fibrils in the ice. The TTR type B fibrils were omitted in this analysis due to the lack of nodes and their flat ribbon morphology. The width of this kind of structure can easily be miscalculated due to possible rotation along their axis, which affects the observed width. Whereas helical structures will always present maximum width, regardless of its orientation in the ice. λ light chain amyloids presented similar width to the TTR type A fibrils with the node I, but unlike most of the latter, they were decorated on both edges. This could be due to the MUS:OT nanoparticles that were used for the decoration. Presence of OT in the NP ligand shell probably alleviated the repelling effect between nanoparticles and allowed them for the tighter decoration. Previously published analysis of λ light chain fibrils, obtained from two patients, showed that the fibrils formed two morphologically distinct aggregates that differed in width and periodicity length (33). Moreover, the two human-derived samples presented distinct fibrillar characteristics, where one type of fibril revealed a width of approximately 11 nm and a pitch length distance of approximately 163 nm (33). The dimensions of these fibrils partially correspond to those of the λ light chain fibrils that we analyzed. Our sample, however, revealed fibrils that were slightly wider and had a shorter pitch length. These differences may stem from the different methods used to obtain the micrographs, that is negative stain TEM versus cryo TEM. It may also be caused by the fact that each patient develops fibrils of a different morphology.

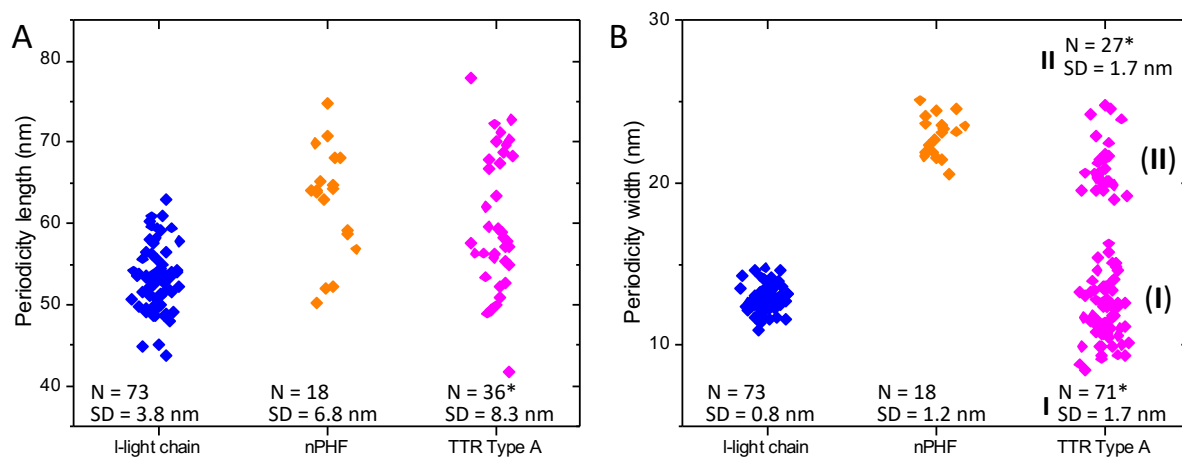


Figure 5.7 Plots showing the fibril A) length and B) width distribution among all studied *ex vivo* derived fibrils. Plot B) also shows the sharp differences in the two types of nodes observed in TTR type fibrils. Each dot represents an averaged value for a single analyzed fibril except *, where only one twist per fibril was analyzed.

The obtained length and width were plotted against each other. Figure 5.8 shows the lack of any correlation for λ light chain and nPHF fibrils due to the rather homogenous distribution of these values. In addition, the plot demonstrates two separate populations of different nodes

present in TTR type A fibrils. The majority of the nodes II also exhibit longer periodicity than nodes I, which is in agreement with the described Chapter 4 theory of positive correlation between the periodicity width and length (139, 158).

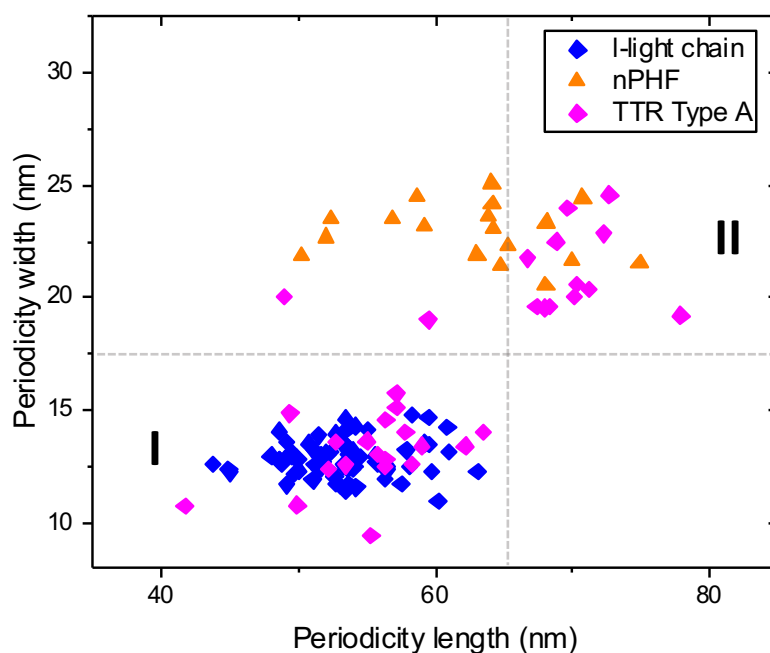


Figure 5.8 A plot showing distribution of width of the all three types of studied *ex vivo* derived fibrils due to the periodicity length. Only 33 twists of TTR type A amyloids, that were eligible for measurement of both corresponding values were found. The plot also shows the two populations of measured nodes of TTR type A fibrils, where nodes II were roughly twice as thick as nodes I and the majority of them presented longer periodicity length than nodes I.

To test the reproducibility of nanoparticles utilization in the amyloid fibril twist analysis, the measurements of the pitch length and width were run by a second operator. For these measurements, λ light chain amyloids were chosen due to their abundance and the smallest standard deviation of periodicity length and width. Figure 5.9 A shows an overlap between the measurements performed by two independent operators. The differences on the values are assigned to the different method of manual measurement but are consistent and both measurements show no correlation between length and width of the fibrils. To address possible differences between the measurements done on the negative stain TEM images, we compared our data obtained on λ light chain amyloids shown in Figure 5.8 with the measurements performed on the negative stain TEM images of the bare fibrils. Figure 5.9 B shows that the distribution of these values, measured with the use of cryo TEM complemented with nanoparticles, is narrower and includes fibrils of smaller periodicity length. Moreover, fibrils of periodicity lengths larger than 65 nm were not observed with use of cryo TEM. This can be due to the surface influence on the fibril morphology, staining artefacts or lateral association of the fibrils caused by the drying step during the sample preparation.

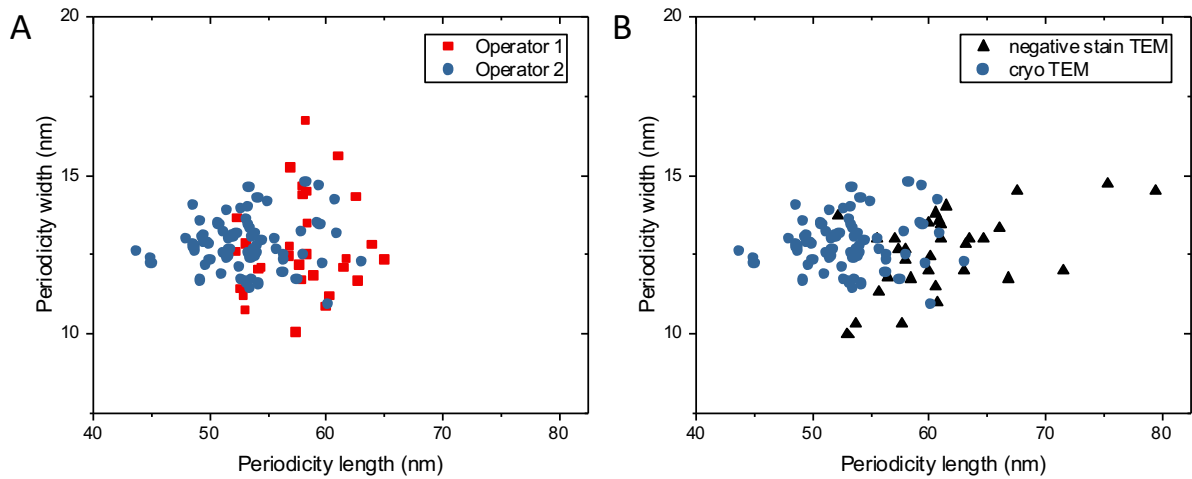


Figure 5.9 Plots showing the results of comparative analysis of our method. A) Plot showing the results of the analysis of λ light chain amyloids periodicity length and width done by two independent operators. B) Plot showing different results obtained via two different methods. The same analysis done on the bare λ light chain amyloids visualized by negative stain TEM and λ light chain amyloids labelled with the MUS:OT nanoparticles visualized by cryo TEM.

Furthermore, decoration with gold nanoparticles of *ex vivo* derived fibrils, enabled the morphological comparison with the *in vitro* obtained amyloid fibrils described in Chapter 4.

5.2.1 Comparison between *ex vivo* and *in vitro* obtained fibrils

We found, that all studied by us *ex vivo* samples show strikingly narrow periodicity length range when compared to the previously measured synthetic $A\beta_{40}$ and recombinant R2 fibrils (Figure 5.10 A). The mean periodicity of the λ light chain amyloids was equal to approximately 53.2 nm, with a standard deviation of 3.8 nm (N=73). The PHF fibrils, derived from the brain of a patient, had an average periodicity equal to 62.8 nm, with a standard deviation of 6.8 nm (N=18). The measurements for TTR type A fibrils, that were done on two types of assemblies of the fibrils, also show a rather narrow distribution of this value with average equal to 60 ± 8.3 nm. This result contradicts the values obtained for the *in vitro* samples, which showed much higher standard deviations: 31.9 nm for $A\beta_{40}$ fibrils (N=33) and 38.6 nm for R2 fibrils (N=20), with an average periodicity length of 76 nm for $A\beta_{40}$ and 95.8 nm for R2 amyloids. These differences are not that obvious for the periodicity width, where no correlation between this value and origin of the amyloids was found (Figure 5.10 B). An interesting observation was also made for $A\beta_{40}$ fibrils where a narrow distribution of periodicity width (standard deviation of 1.2 nm) was correlated with significantly big range of periodicity length. These values are also different to that of many other studied $A\beta_{40}$ fibrils prepared *in vitro* (30, 159, 172). As in our case, the characteristic feature of these $A\beta_{40}$ fibrils is a considerably big distribution of periodicity length and width. This result differs slightly from the recently described data on the

A β_{40} fibrils purified from the brain tissue of AD affected patients. In this case, majority of the described fibrils, fell into three uniform populations, with the small fraction of the amyloids, which exhibited other morphology (166). The big distribution of periodicity length and width in *in vitro* prepared fibrils was also reported for other amyloids such as β -lactoglobulin, human islet amyloid polypeptide, A β_{42} or α -synuclein (139, 156, 173, 174). Nevertheless, *ex vivo* derived samples studied by us showed a more homogeneous fibril population in comparison with *in vitro* obtained fibrils described in the Chapter 4.

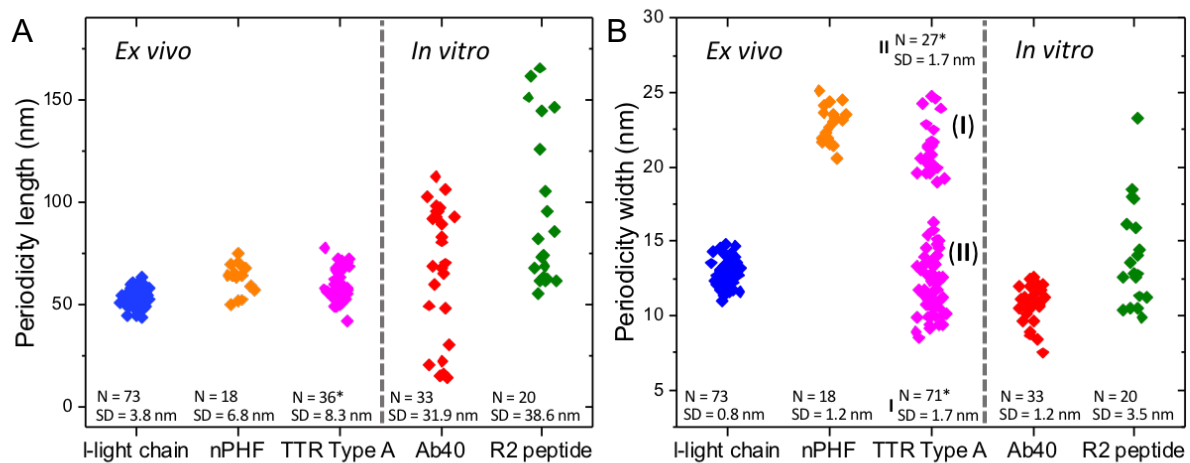


Figure 5.10 Plots showing the distribution of periodicity A) length and B) width for all analyzed types of amyloid fibrils.

This contrast shows, that the populations of fibrils present in each measured sample differ in morphology depending on the origin of the sample and demonstrates that the studied human-derived amyloids are much more uniform than fibrils generated *in vitro*. Further analysis of the periodicity showed that the length and width of the periodicity are positively correlated in the case of the fibrils produced *in vitro* as demonstrated in Chapter 4. Unlike in the case of TTR type A fibrils, no distinct populations were observed and a smooth periodicity length distribution was present in case of A β_{40} and R2 fibrils. Amyloids derived from human tissue indicated a significant homogeneity of the periodicity width and no correlation between this value and the fibril length, except the two types of nodes observed in TTR type A fibrils. However, in this case, the correlation is a result of higher assemblies of the mature fibrils rather than various numbers of protofilaments in the mature amyloid fibril (Figure 5.11).

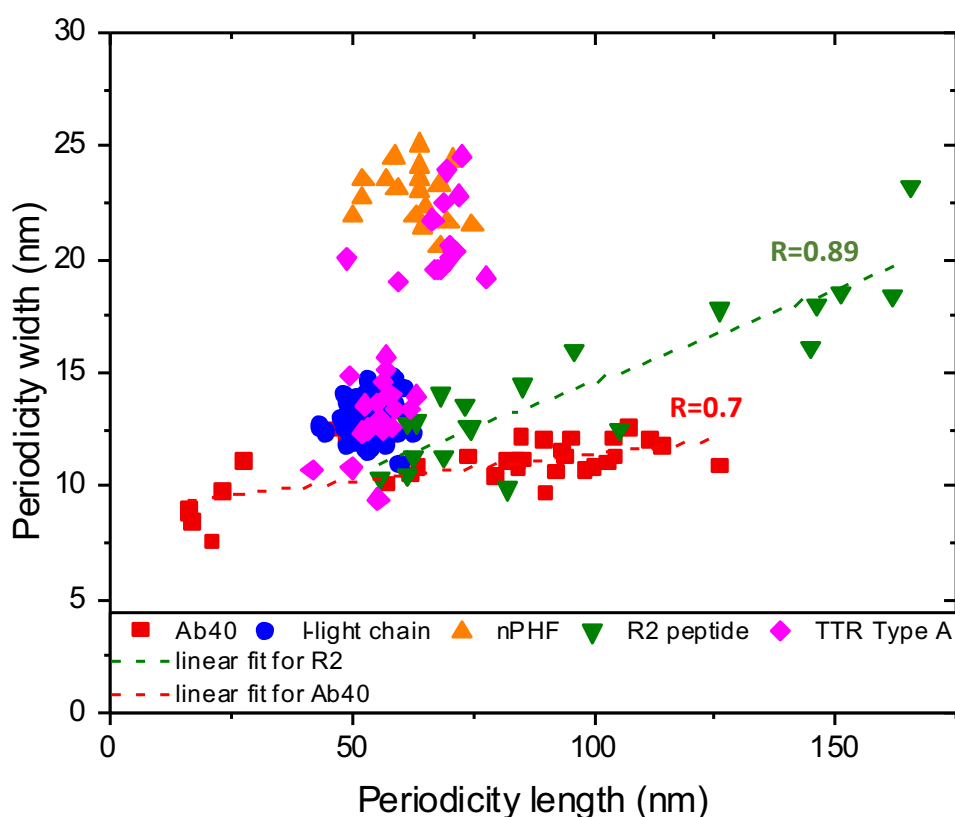


Figure 5.11 Plot showing the difference in the correlation between the periodicity length and width between *in vitro* and *ex vivo* derived amyloids.

Moreover, the analysis of recombinant and synthetic samples showed a wide range of structural polymorphs, that is straight structural polymorphs or more complex fibrils, such those presenting three-fold symmetry. Figure 5.11 shows an analysis that correlates the periodicity length and width for synthetic A β ₄₀ and recombinant R2 fibrils. This is in agreement with the theory proposed by De los Rios (158), which assumes that the periodicity of the fibril depends on the number of protofilaments constituting the fibril. This theory is explained in detail in Chapter 4. Correlation shown in Figure 5.11 suggests the linear dependence of the width of the fibril and periodicity length in the analyzed amyloids aggregated *in vitro*. On the contrary, analyzed *ex vivo* samples were composed of a rather homogenous fibril population, suggesting uniform protofibril number per mature amyloid. Indeed, we observed a narrow distribution of the periodicity width and length in the λ light chain amyloids and PHFs amyloids, that showed twisted ribbons with remarkably conserved periodicity length and width. It was also noticed in the two types of nodes in TTR type A fibrils, that within each population no correlation between length and width of the periodicity was displayed. This uniformness of the *ex vivo* fibrils contrasts to the amyloids derived from recombinant or synthetic proteins in cell-free systems.

Our findings suggest that the mechanisms of amyloid formation *in vitro* vary greatly from those occurring *in vivo*.

5.3 Conclusions

Compared to existing methods, the coupling of MUS:OT and fractionated allMUS nanoparticles with cryo TEM allows for a straightforward examination of the entire population of fibrillar polymorphs. It can be also successfully used for complex biological mixtures, requiring only a few microliters of a sample. Moreover, a sample does not need to be extensively processed beforehand, as the fibrils bound to nanoparticles are easily distinguished from other tissue components. Therefore, this method permits the image analysis on minute amounts of sample of relatively low purity.

The analysis of the fibril morphology with the use of our method varies slightly between operators, which is the case for every technique that requires manual measurement of the images. The general outcome of the analysis obtained by both operators is comparable and strengthens the result. However, the results vary when compared to negative stain TEM images, which is expected, since two different methods are compared.

In vitro obtained samples studied by us showed clear correlation between the periodicity length and width. In contrast, the *ex vivo* samples analyzed here were composed of a rather homogenous fibril populations, indicating uniform protofibril number per mature amyloid. This uniformness of the described here *ex vivo* fibrils differs from the amyloids derived from recombinant or synthetic proteins in cell-free systems. This supports the hypothesis of the immense influence of the tissue milieu on the amyloid formation.

Our method does not require elaborate enrichment, seeding, or any other form of extensive sample processing: the native fibril is directly observable in its solvated state. We believe that our nanoparticles can be used as a complementary tool in studying the polymorphic distribution of amyloid fibrils. This can be done by facilitating and accelerating sample screening, data acquisition and processing while requiring only minute amounts of sample. Moreover, the ability of nanoparticles to variously decorate polymorphic species opens new doors in diagnostic strategies. It will allow the detailed characterization of fibril polymorphism in biological samples such as plasma, cerebrospinal fluid, postmortem brains or tissue biopsies.

5.4 Materials and methods

Nanoparticles

Nanoparticles were prepared and characterized in the same way as presented in the Chapter 3.

AL amyloid fibrils

Heart tissue was collected at the University Clinic Heidelberg, Germany, from a 51-year-old male patient who had to undergo a heart transplantation due to systemic AL amyloidosis with severe cardiac involvement. The method for fibril extraction from human tissue was based on a previously established protocol(33), making use of the water solubility of fibrils, with small amendments. A total of 250 mg of frozen heart tissue was kept on ice shortly and then diced into fine pieces using a scalpel. Next, 0.5 ml of trisaminomethane (Tris) calcium buffer (20 mM Tris, 138 mM NaCl, 2 mM CaCl₂, 0.1% NaN₃, storing condition 4°C, pH 8.0) was added to the diced tissue material. The sample was mixed using a Kontes pellet pestle for 10 s in a pulsating manner (1 s on, 1 s off) and centrifuged (6000 rpm, 5 min, 4°C). The supernatant was stored. This cycle of resuspension, mixing, centrifuging and storing was repeated 5 times, and a clear supernatant was obtained. After the last centrifugation step, the pellet was resuspended in 1 ml of freshly prepared 5 mg ml⁻¹ *Clostridium histolyticum* collagenase (Sigma) and ethylenediaminetetraacetic acid (EDTA)-free protease inhibitor (Roche) (1 tablet in 7 ml of Tris calcium buffer) in Tris calcium buffer and incubated for 17 h at 37°C under constant agitation (1100 /min, horizontal position of the tube). Afterwards, the sample was centrifuged (6000 rpm, 20°C, 30 min). The supernatant was stored, and the pellet was washed 10 times by the addition of 0.5 ml of ice-cold Tris EDTA buffer (20 mM Tris, 140 mM NaCl, 10 mM EDTA, 0.1% NaN₃, storing condition 4°C, pH 8.0), followed by mixing with the Kontes pellet pestle and centrifugation (6000 rpm, 5 min, 4°C). For each step, the supernatant was stored. The same washing procedure was repeated with MilliQ water instead of Tris EDTA buffer for 10 steps. The collection of human material was conducted under the approval of the ethical committee at Heidelberg University, while the extraction of fibrils from the tissue was approved by the ethical committee of Ulm University. These fibrils were a gift from prof. Marcus Faendrich, Ulm University.

Native PHFs fibrils

Native PHFs fibrils were a generous gift of AC Immune SA.

TTR amyloid fibrils

Both types of TTR amyloid fibrils were received as a gift from prof. Marcus Faendrich, Ulm University.

Incubation of the amyloid fibrils with nanoparticles

To limit any unwanted biological activity (e.g., from enzymes), the *ex vivo* samples were incubated at low temperatures (20°C overnight) with a final concentration of NPs ranging from 0.1 mg/ml to 0.5 mg/ml. The nature of the sample (i.e., still containing other proteins and biological structures) required a higher concentration of NPs. During the incubation, agitation was applied (300 rpm). Incubation was performed for 24 h-48 h until sufficient coverage of the fibrils with NPs was obtained.

In the case of the PHFs, a dark sediment was observed at the bottom of the Eppendorf tube, suggesting strong adsorption of our nanomaterial to structures present in the sample. The sample was gently resuspended using a pipette to generate some agitation immediately prior to cryo grid preparation.

Cryo electron microscopy of amyloid and nanoparticle samples

For cryo TEM microscopy, a 3 μ l droplet of sample containing amyloids and nanoparticles suspended in buffer was deposited onto a lacey carbon film (Electron Microscopy Sciences) and blotted to a thin (100-300 nm) layer of liquid that was flash frozen in liquid ethane using an FEI Vitrobot Mark IV. Imaging was performed using a Gatan single tilt cryo holder operated on an FEI Tecnai Spirit BioTWIN 80 kV transmission electron microscope in LowDose Mode to visualize the samples at an average exposure of 1-3 electrons/ \AA^2 on a Ceta camera.

Fibril crossover distance and width analysis

Micrographs of the amyloids decorated with NPs were analyzed using ImageJ software, where the crossover distance of the fibril was measured manually. For each fibril, the average crossover distance and width were calculated and plotted in the graphs using OriginPro software. 73 AL amyloid fibrils were evaluated from 40 acquired images, and 18 nPHF fibrils were measured on 18 micrographs.

Chapter 6

Stability of the decoration and labelling in complex solutions

6.1 Introduction

Specific morphology of the fibril can be achieved by manipulating the aggregation process conditions. Tuning the pH, ionic strength or temperature of the fibrillation may favor occurrence of certain polymorphic species (26, 27). An ideal contrast marker for amyloid morphology studies would therefore be equally efficient in various conditions present in the sample. It would also have to be resistant to often extreme environment, such as strongly acidic pH or high ionic strength of the solution. Moreover, after reaching the plateau of growth, mature amyloid fibrils are frequently subjected to further treatments. One of them is increasing their concentration by long and intense centrifugation prior to further experimental steps, such as mass spectrometry or Fourier transform infrared spectroscopy (ATR-FTIR) (156). Another very commonly used processing is sonication of the fibrils. This step is necessary to obtain seeds, needed for the consecutive aggregation of the daughter fibrils (26, 175). It is important, that this harsh treatment would not destroy or negatively affect the contrast marker that facilitates the morphology studies.

In the first part of this chapter we show that our gold nanoparticles are equally effective as labelling agents for fibrils prepared and stored in various buffers. We also demonstrate, that substantial drop of the buffer pH, does not significantly affect the labelling quality. Moreover, we show that our gold nanoparticles remain attached on the fibrils after dilution, sonication, addition of other biomolecules and strong centrifugation (Figure 6.1 A).

The second part of this chapter focuses on the amyloid labelling in complex biological solutions. To reflect the physiological milieu of amyloid affected tissue, amyloid fibrils can be produced *in vivo* in cell-based or animal models (176–178). These systems present a big advantage over *in vitro* systems in reproducing physiological conditions. However, further processing frequently requires extensive treatment in order to preform subsequent experiments with *in vivo* obtained samples (179, 180). Cerebrospinal fluid (CSF) can give an insight into the central nervous system state, since 20% of protein that is present in CSF is brain derived (181). Among them, mutant huntingtin, α -synuclein and A β were detected in various yet small quantities (181–183). Here we exhibit, that we are capable to label amyloid fibrils mixed

directly with CSF and freshly obtained cell debris. This labelling allowed for visualization and detection of decorated amyloid fibrils present in solutions of high concentration of other biomolecules under TEM (Figure 6.1 B).

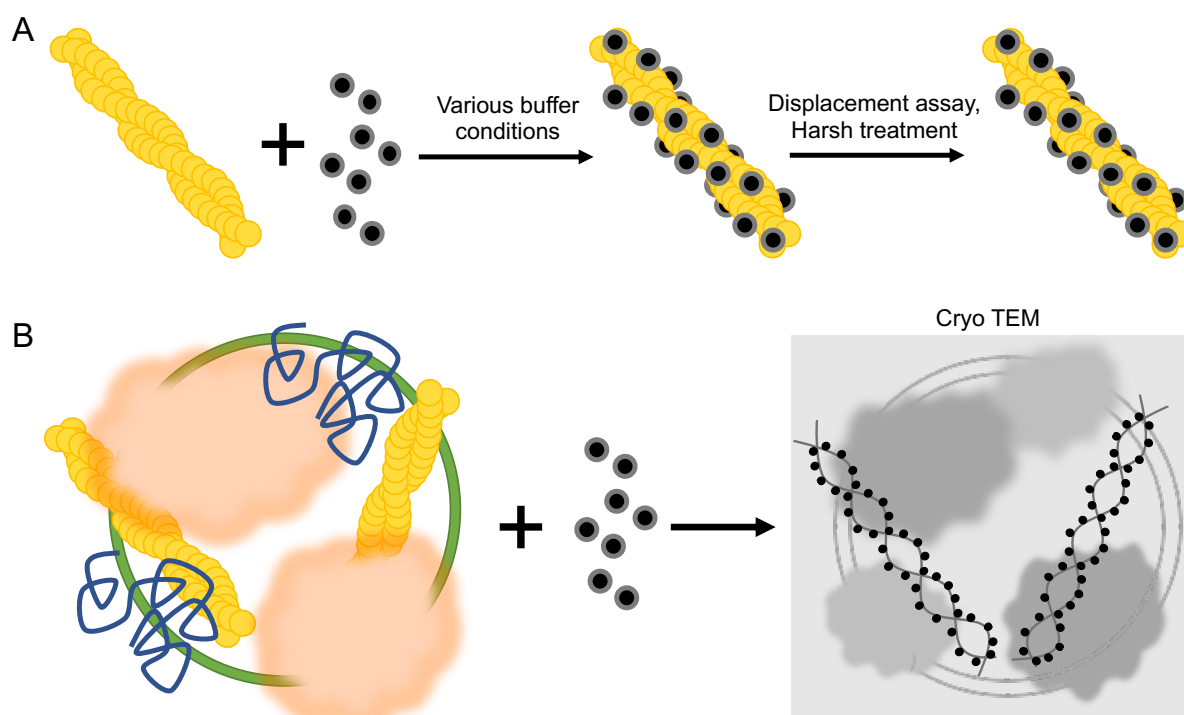


Figure 6.1 Schematic representation of this Chapter's experimental section. A) In the first part of this Chapter we focus on testing the stability of the decoration under various conditions. B) Second part of this Chapter presents the data obtained on the amyloid labelling in the presence of strongly bio-contaminated milieu.

In summary, this chapter focuses on possible challenges that could be encountered during *in vivo* and *in vitro* amyloid decoration with our gold nanoparticles. We demonstrate that these challenges are overcome, which puts our gold nanomaterial as a versatile contrast marker for amyloid studies, that can be used under various conditions and heavily bio contaminated samples.

6.2 Results and discussion

6.2.1 Stability of decoration with the nanoparticles

We tested how properties of preparation and storage solutions, used for amyloids obtained *in vitro*, influence the decoration of amyloid fibrils. In order to address that, we investigated two important attributes of buffers: pH and ionic strength. Mature α -synuclein fibrils were used to test how changes of the pH influence the decoration of the amyloid fibrils. To minimize hydrophobic interactions between nanoparticles and the fibril surface we used fractionated allMUS nanoparticles that lack the hydrophobic OT ligand. After the decoration took place in

the standard buffer of pH 7.4, the pH of the solution was modified by dropwise addition of 0.1M hydrochloric acid (HCl). The isoelectric point (pI) value of α -synuclein is predicted to be at pH 4.7 (184). To test how minimizing the net charge of the amyloid fibrils influence the decoration, first adjustment of the solution with decorated α -synuclein fibrils was aiming to reach the pI value. It has been reported that low pH promotes the aggregation of several amyloid fibrils (185–188). To test labelling resistance to the acidic environment, the second adjustment of the solution pH with labelled fibrils was aiming on remarkably low pH. Cryo TEM images had shown labelled α -synuclein fibrils in all three tested pH conditions (Figure 6.2 A). Persistent decoration, visible at pH 4.61, suggests that the complete removal of the charge from the amyloid fibril is more complex due to the folding of the primary structure (189, 190) and highlights the role of the aliphatic chain (11 carbons) of the MUS molecule. The effect of this chain is especially pronounced at pH 1, where we still observe decorated α -synuclein fibrils. We speculate that after the first contact via the charged sulphonic groups, the attached ligands deform to shield the hydrophobic alkane backbone and decorate the fibril surface via hydrophobic interactions. Similar behavior of MUS:OT nanoparticles was already proposed upon interactions with lipid bilayers (191). The estimation based on the pK_a values of each residue consisting α -synuclein protein, assumes that the net charge of α -synuclein stored in pH 7.4 is around -9 (192). Below pH 4.7, the net charge of α -synuclein fibrils will turn positive, which is a significant change in comparison with the fibrils stored at pH 7.4. Even at such a low pH, we still observe remained decoration (Figure 6.2 A). This result shows that the labelling of the amyloid fibrils is very robust and not affected by the subsequent drop of the solution's pH. Previous results show, that gold nanomaterial can be prepared and stored in acidic environment (193–195), therefore low pH itself should not affect significantly the gold core of our nanomaterial².

The ionic strength is another important factor that influences the fibrillation process (188, 196). We examined the efficiency of the gold nanoparticles labelling in solutions with different ionic strengths. For this we used MUS:OT nanoparticles and A β ₄₀ amyloid fibrils prepared in buffers with different NaCl content. The first solution contained 25 mM of NaCl and the second one 125 mM of NaCl. Cryo TEM images shown that the decoration of amyloid fibrils was achieved in both samples (Figure 6.2 B).

² However, gold nanoparticles are dissolved in *aqua regia*, which is a mixture of hydrochloric acid and nitric acid.

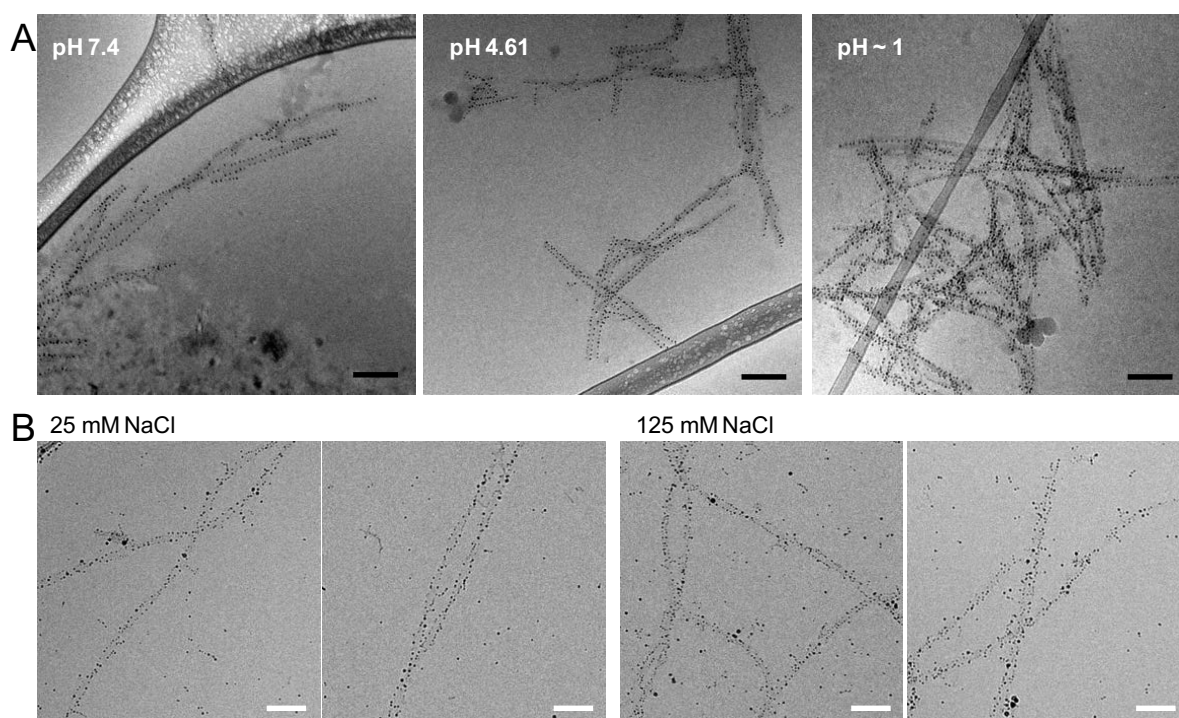


Figure 6.2 Cryo TEM images of amyloid fibrils decoration tested in various conditions. A) pH assay of α -synuclein fibrils labelled with fractionated allMUS nanoparticles shows that the decoration of the amyloid fibrils is resistant to the lower ranges of pH. B) $A\beta_{40}$ fibrils grown in buffers of different ionic strengths are prone to decoration with MUS:OT nanoparticles, regardless of the NaCl content. Black scale bars are 100 nm and white scale bars are 50 nm.

Due to the enhanced ionic strength, fibrils were more abundant in the second solution. The concentration of the nanoparticles was the same in both samples. Despite that, the decoration of the more crowded second sample was comparable with the amyloids grown in the presence of 25 mM NaCl. This experiment shows that our labelling system should be compatible with buffers of different composition and features.

Mature amyloid fibrils are often a subject to various treatments. Some may be considered mild, such as dilution, whereas other can be considered harsh, like sonication. Prior to test the resistance of the amyloid decoration to some of these procedures, we prepared MUS:OT decorated FL Httex1 43Q fibrils.

We performed washing assay to test, whether our nanomaterial detaches from the already labelled fibril upon the extensive exchange of buffer. That could happen due to the changes in the ratio between free and attached nanoparticles present in the solution. Labelled amyloids were centrifuged for 30 minutes under 14 000 rpm, after which 50% of supernatant, containing unbound nanoparticles, was discarded and replaced with fresh PBS buffer. The procedure was repeated 3 times in 24 hours intervals in order to increase the time of possible detachment of nanoparticles from the fibrils. Cryo TEM images of the sample before and after the washing procedure depicted labelled amyloid fibrils (Figure 6.3 A). The control sample, imaged before

the procedure, contained bigger aggregates of longer fibrils. Applied strong centrifugation affected the morphology of the fibrils, which became visibly shorter and well dispersed in the ice. Despite this significant interference in the sample morphology, the labelling seemed to be unaffected.

Sonication of amyloid fibrils is a common procedure performed before the seeding. Seeding is a process of nucleation where already misfolded structures serve as a template for promoting polymerization (51). We tested the resistance of the labelling to sonication of A β ₄₀ amyloids decorated with MUS:OT. Prior to the sonication, the control sample was diluted 4 times with water to also test the effect of dilution on the nanoparticles decoration. Cryo TEM images show that A β ₄₀ fibrils become shorter after 30 seconds of sonication. After 1 minute mostly short fibrils, no longer than 300 nm on average, were observed. Despite this harsh treatment and significant dilution of the sample, no difference between the quality of labelling was noticed (Figure 6.3 B).

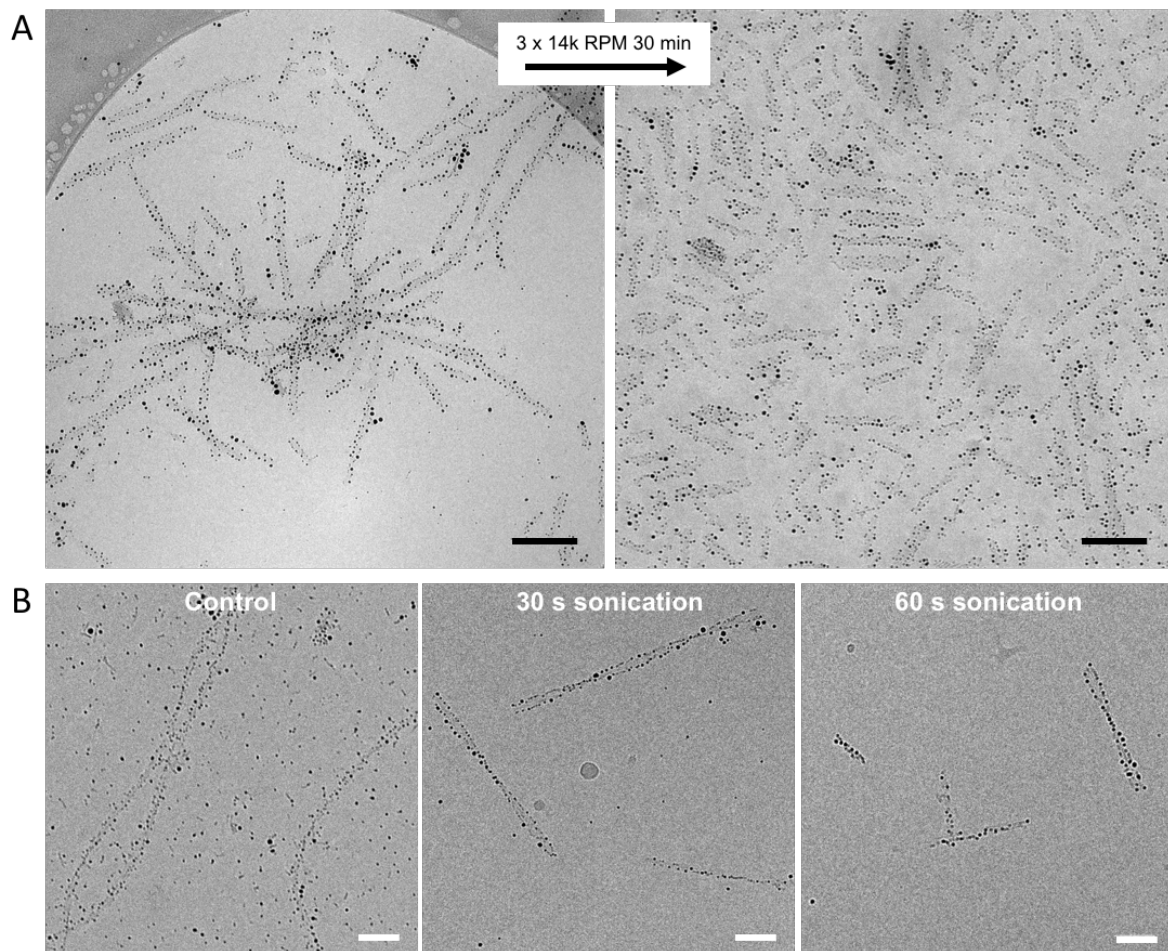


Figure 6.3 Cryo TEM images of MUS:OT labelled fibrils subjected to various treatments. A) Despite the significant interference in the morphology, FL Httex1 43Q fibrils exhibit the same level of decoration after washing and centrifuging several times. B) Cryo TEM images of A β ₄₀ fibrils decorated with MUS:OT nanoparticles diluted 4 times and sonicated for 30 and 60 seconds. Black scale bars are 100 nm and white scale bars are 50 nm.

These experiments clearly indicate that labeling of the amyloid fibrils is resistant to various procedures, such as strong centrifugation, sonication, washing, changing the buffer properties and dilution.

Amyloid fibrils are often tested on cells in order to evaluate their toxicity or interactions with other biomolecules (22, 74, 115). We addressed the possible detachment of nanoparticles from the amyloid fibrils upon the preferential binding with other molecules. Prior the experiment, we prepared well labelled with our nanoparticles FL Httex1 43Q and A β ₄₀ fibrils. Decorated fibrils were then subsequently mixed with more complex biological solutions. MUS:OT and fractionated allMUS decorated FL Httex1 43Q fibrils were co-incubated with 5 μ M Bovine Serum Albumin (BSA), which is a substantial element of most of the cell media. MUS:OT labelled A β ₄₀ amyloids were mixed with freshly obtained cell debris. Decorated FL Httex1 43Q fibrils were incubated with BSA for 24 and 72 hours in order to evaluate the time influence on the possible detachment of nanoparticles. Negative stain TEM images of FL Httex1 43Q fibrils incubated with BSA, show nanoparticles interacting in a similar manner with amyloid fibrils as in the control sample (Figure 6.4). This propensity does not change in time and does not depend on the type of the nanoparticles. Beside fibrils with nanoparticles on the surface, negative stain TEM images displayed small structures with sporadically attached nanoparticles. Previously obtained results show, that BSA molecules interact with gold nanoparticles protected with MUS and MUS:OT ligands (197, 198). We suspect, that these structures are seemingly BSA molecules, which captured unbounded nanoparticles present in the solution.

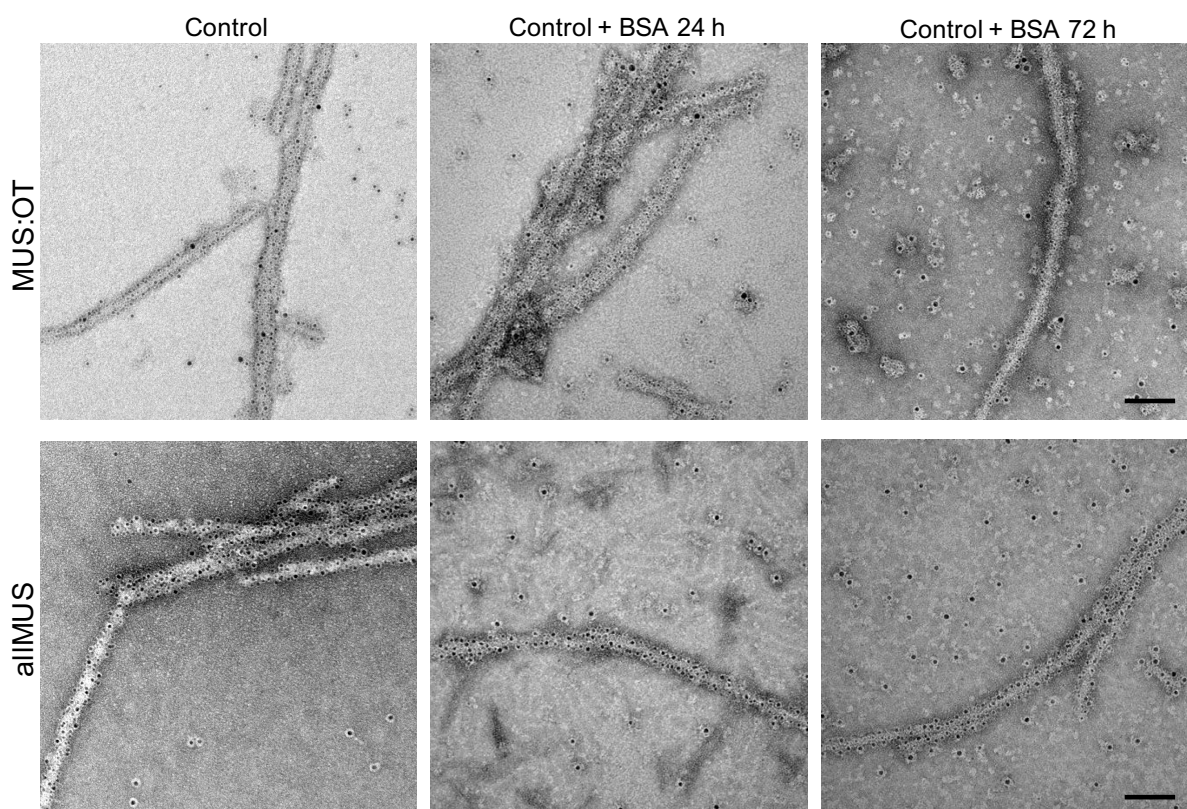


Figure 6.4 Negative stain TEM images showing the time assay of co-incubation of labelled FL Httex1 43Q fibrils with BSA. Fibrils decorated by both: MUS:OT and fractionated allMUS nanoparticles seem to remain labelled on the same level as the control sample after co-incubation with BSA for 24 and 72 hours. Scale bars are 50 nm.

A β_{40} amyloids labelled with MUS:OT were mixed with cell debris in order to test the resistance of the labelling in an even more crowded and complex environment. Cell debris was obtained via disruption of cells by centrifugal force without addition of any lysis buffers. Lysis buffers could potentially influence the behavior of nanoparticles and biomolecules present in the sample. Negative stain TEM of decorated fibrils mixed with the cell debris, shown assemblies of fibrils with other structures. However, fibrils were still discerned from the rest of biomolecules due to their characteristic shape. Staining agent (1% water solution of uranyl acetate) highlighted the presence of all biomolecules, which hindered slightly the identification of amyloid fibrils (Figure 6.5 A). However, preparation of the same sample without the use of staining agent, revealed the presence of seemingly very well decorated A β_{40} amyloids that were immediately visible on the grid. By omitting the use of uranyl acetate, we detected only the presence of labelled A β_{40} amyloids in this sample (Figure 6.5 B).

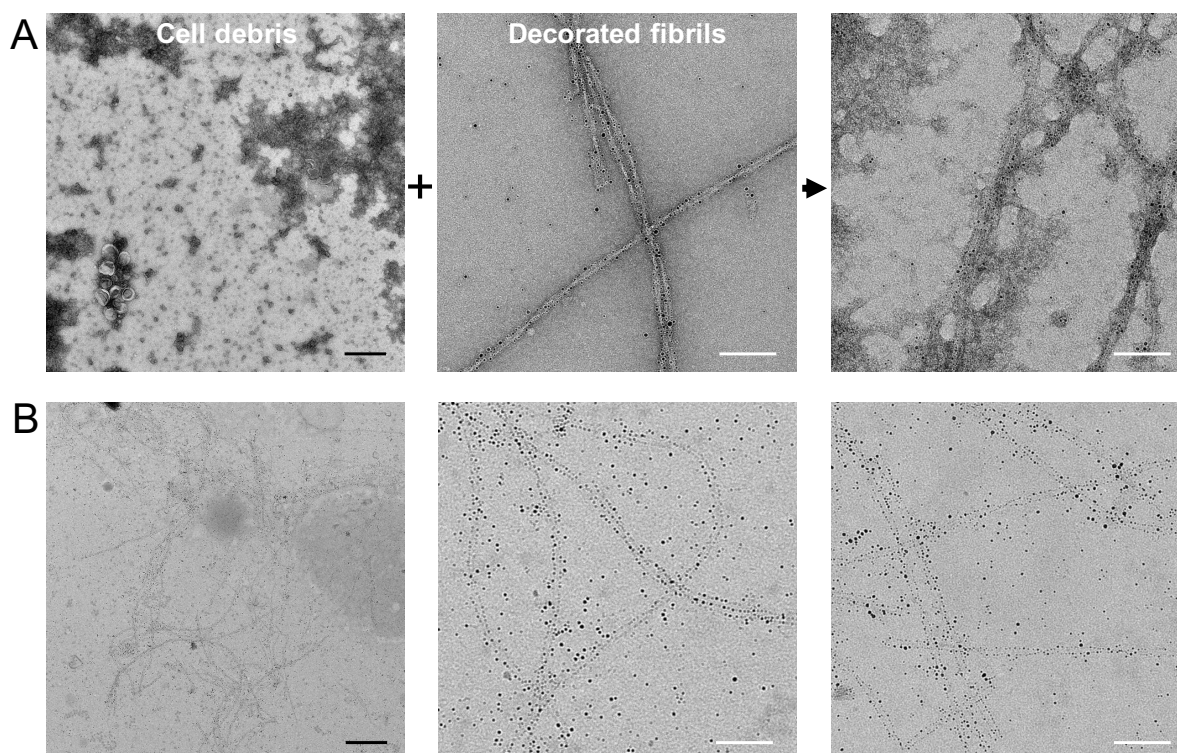


Figure 6.5 A β_{40} fibrils labelled with MUS:OT nanoparticles and mixed with cell debris. A) Negative stain TEM images of the mixing procedure, where cell debris were mixed with decorated A β_{40} and imaged with the use of negative stain. B) TEM images of sample containing cell debris and labelled A β_{40} . Sample was prepared without the use of uranyl acetate. Black scale bars are 400 nm and white scale bars are 100 nm.

TEM micrographs shown in the Figure 6.5 B suggest also, that our nanomaterial can be used as selective contrast marker for detecting amyloid fibrils in the crowded and complex environment. Moreover, we proved, that the extent of decoration of the fibrils does not change upon the presence of other biomolecules. Our gold nanoparticles could be potentially used to label and detect amyloid fibrils directly in complex solutions.

6.2.2 Labelling of amyloid fibrils in complex solutions

We established that decoration with our gold nanoparticles is resistant to various manipulations, including co-incubation with a high concentration of many other biomolecules. This paved the way for more challenging experiments. In order to test the efficiency of labelling taking place in a crowded environment, we incubated bare FL Httex1 43Q and A β_{40} amyloid fibrils with gold nanoparticles in solutions containing BSA, cell media and cell debris.

As seen from Figure 6.4, the addition of BSA to already labelled FL Httex1 43Q fibrils, does not change the overall decoration of amyloids. To test the decoration competition between amyloids and BSA, we incubated both of these structures with nanoparticles at the same time. Both MUS:OT and fractionated allMUS nanoparticles were used in two series of samples.

Negative stain TEM of fibrils co-incubated with BSA and nanoparticles depict very similar results to the one shown in Figure 6.4 were the decoration with nanomaterial and addition of BSA took place at different steps. FL Httex1 43Q fibrils co-incubated with BSA and nanoparticles at the same time, present similar coverage as the control sample (Figure 6.6). Similarly to Figure 6.4, some small structures (supposedly BSA) with sporadic nanoparticles on the surface were observed. The significant difference in the coverage of FL Httex1 43Q with nanoparticles was observed upon the co-incubation with serum-free cell media (Neurobasal™ medium). For both types of tested nanomaterial, visible decrease of the fibril coverage in comparison with the control sample, was observed. This could be explained by the presence of other media components, that would capture some of the free nanoparticles. This reduction of available nanomaterial in the solution would result in a weaker amyloid decoration. Despite that, some coverage of amyloids with the nanoparticles was seen (Figure 6.6).

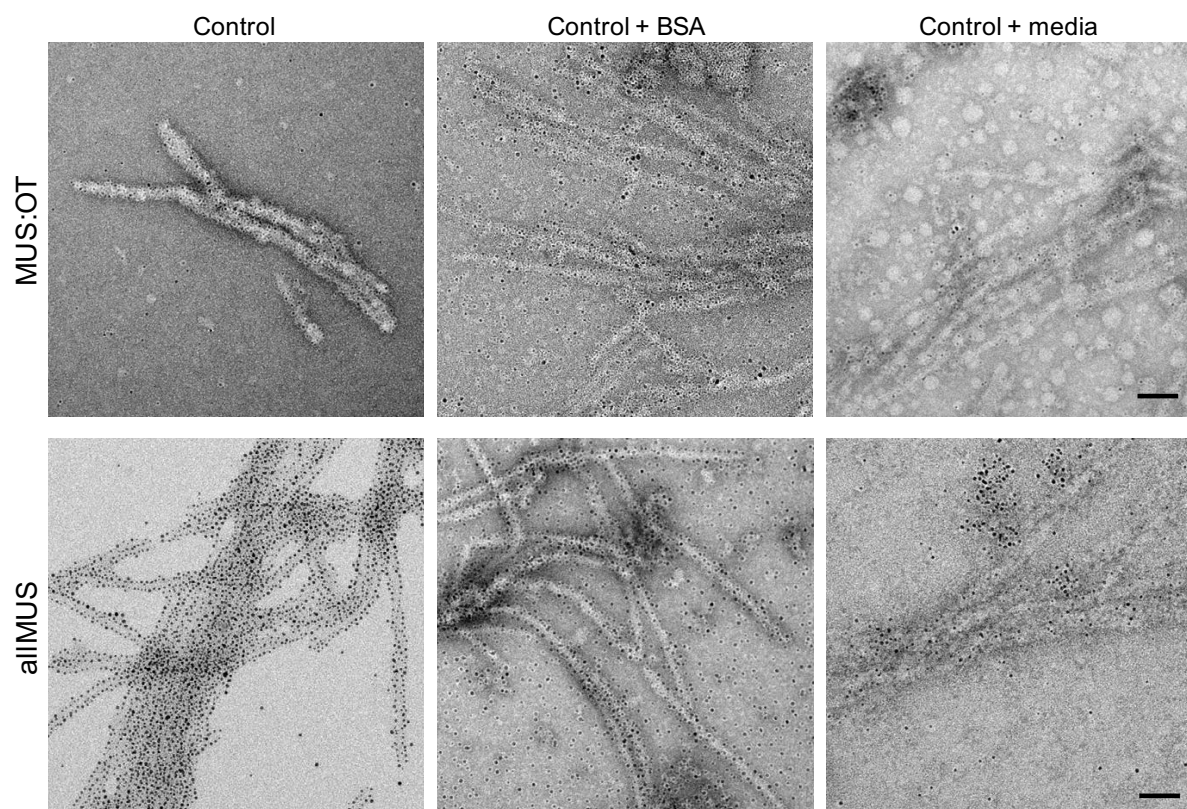


Figure 6.6 Negative stain TEM images of FL Httex1 43Q fibrils decorated with MUS:OT and fractionated allMUS nanoparticles in presence of BSA and media. Scale bars are 50 nm.

The attempt of labelling the amyloid fibrils in a complex solution was repeated with the use of A β ₄₀ amyloid fibrils and cell debris. First, to address the issue of capturing the free nanoparticles, a concentration assay was performed. We prepared three solutions containing A β ₄₀ fibrils, cell debris and MUS:OT nanoparticles. All solutions differed in ratios between

nanomaterial and A β ₄₀ concentration. In order to conceal the background with various cell components and debris, we omitted the staining step in preparation of TEM grid. TEM images illustrate the presence of elongated structures in each sample. Magnification on these structures showed nanoparticles delineating characteristic contour of amyloid fibrils (Figure 6.7). The delineation of the amyloid fibrils was more visible in the solutions with the higher concentration of nanoparticles.

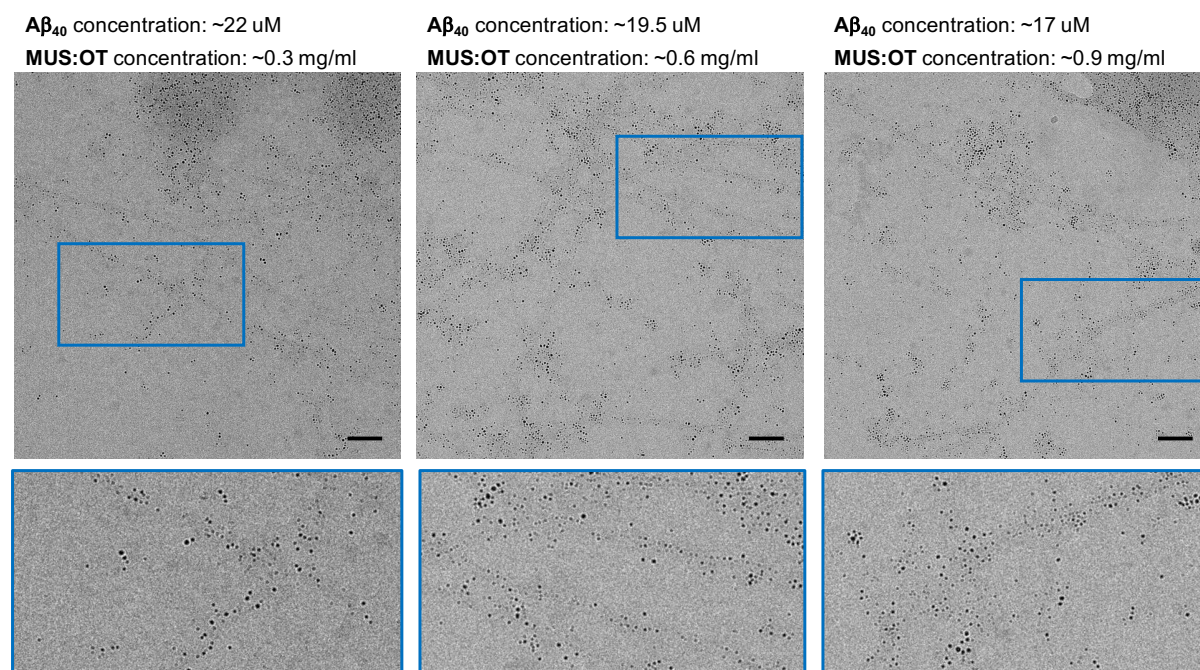


Figure 6.7 TEM images of concentration assay of A β ₄₀ fibrils decorated with MUS:OT nanoparticles in the presence of cell debris. Bottom panel shows the magnified area within the blue box depicted on the corresponding TEM image in the upper panel. Scale bars are 100 nm.

To exclude possible drying artefacts, explained in detail in Chapter 3, we performed cryo TEM on the samples containing higher concentration of nanoparticles. Cryo TEM images of these samples indicate the presence of cell debris material such as vesicles and big aggregates of biomolecules (Figure 6.8). Cell debris was also mixed with other types of amyloids, such as FL Httex1 43Q and α -synuclein. In each case we could observe decorated amyloid fibrils, which suggests that various types of amyloid fibrils can be labelled by our nanomaterial in the contaminated environment.

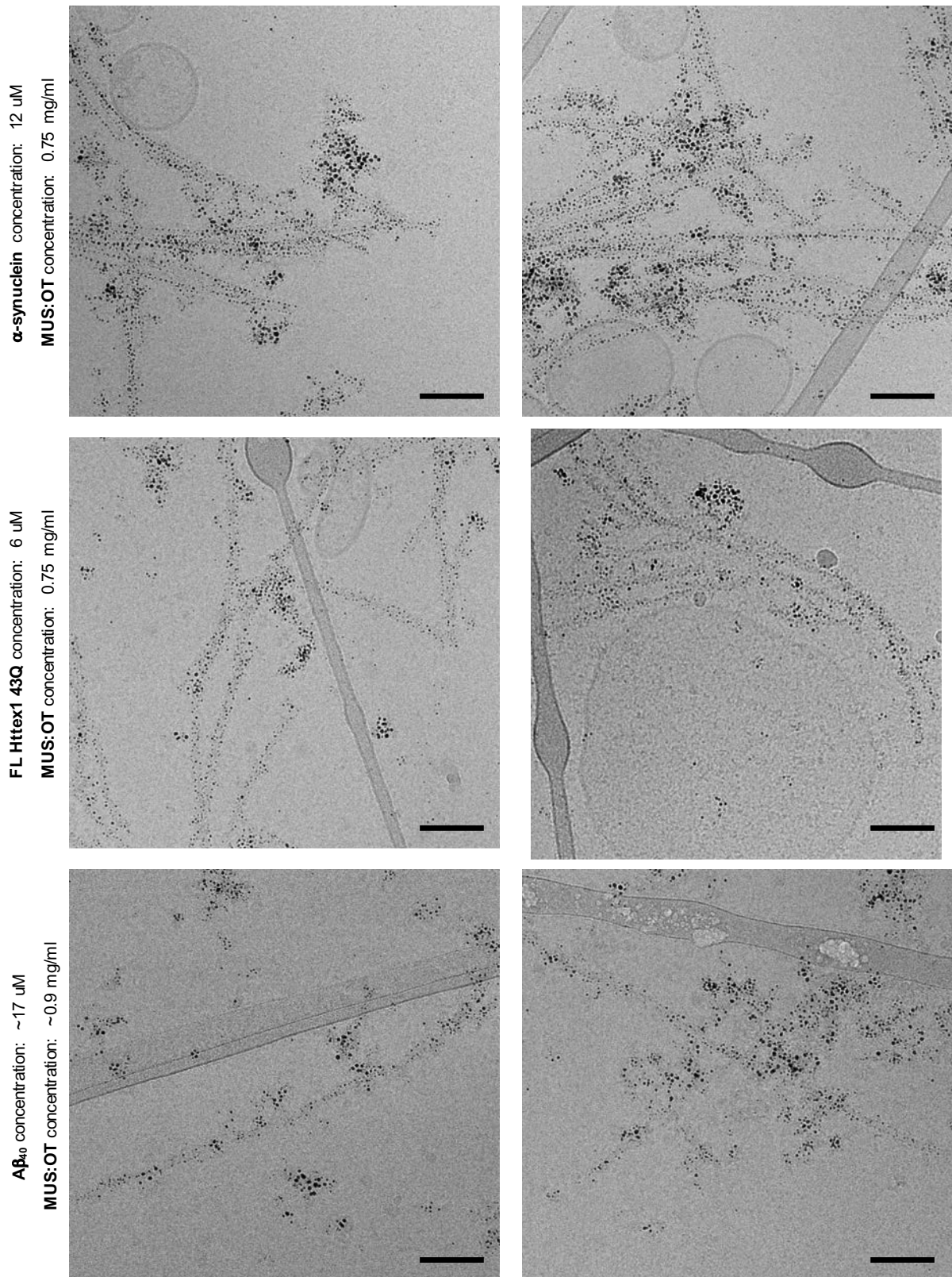


Figure 6.8 Cryo TEM images of A β_{40} fibrils decorated with the MUS:OT nanoparticles in the presence of cell debris. Scale bars are 100 nm.

We also tested the labelling efficiency of amyloid fibrils co-incubated with MUS:OT nanoparticles in the presence of cerebrospinal fluid (CSF). Negative stain TEM images of CSF

showed presence of various structures. Their size ranged from 10 nm diameter for seemingly single structures, to larger than 200 nm assemblies of biomolecules. These elements present in CSF could potentially bind nanoparticles introduced to the solution (Figure 6.9). To address possible issues of free nanoparticles available for the amyloid decoration, a concentration assay was performed with various amounts of amyloid fibrils and nanomaterial.

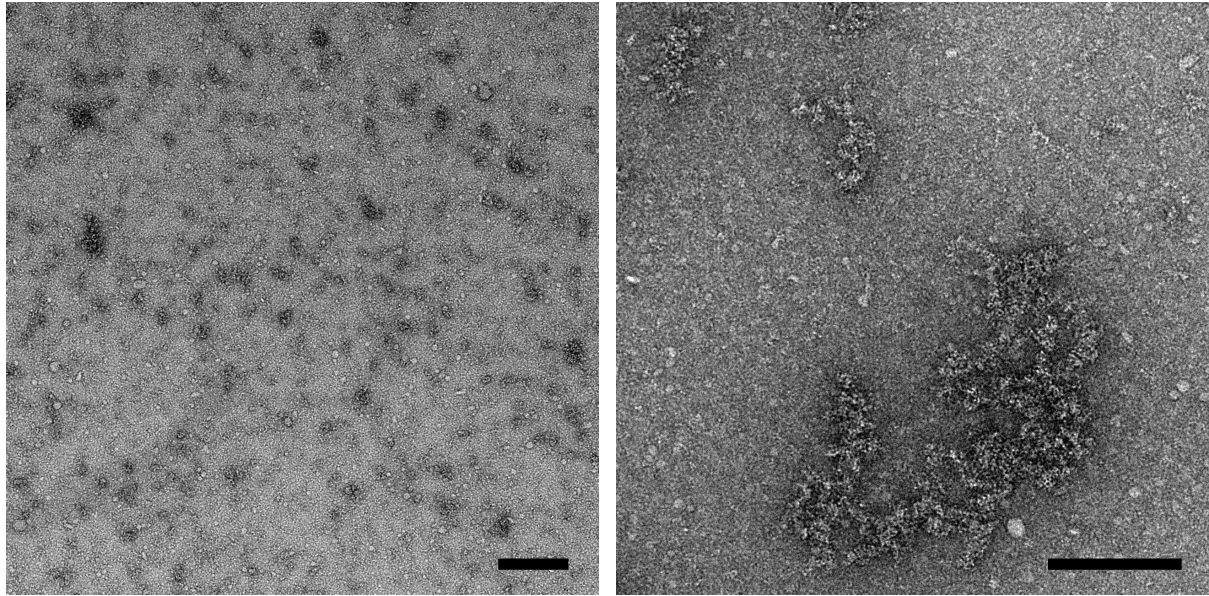


Figure 6.9 Negative stain TEM images of CSF. Scale bars are 200 nm.

Solutions of amyloid fibrils and MUS:OT nanoparticles were mixed with CSF in a way that in each case CSF was constituting 60% of the total volume in each sample. Cryo TEM images show that FL Httex1 43Q and A β ₄₀ fibrils are getting decorated in the presence of CSF, however this decoration is slightly impaired with the use of less concentrated nanomaterial. Despite that, amyloids were quickly detected in the ice due to the decoration with MUS:OT nanoparticles that enhanced their contrast (Figure 6.10).

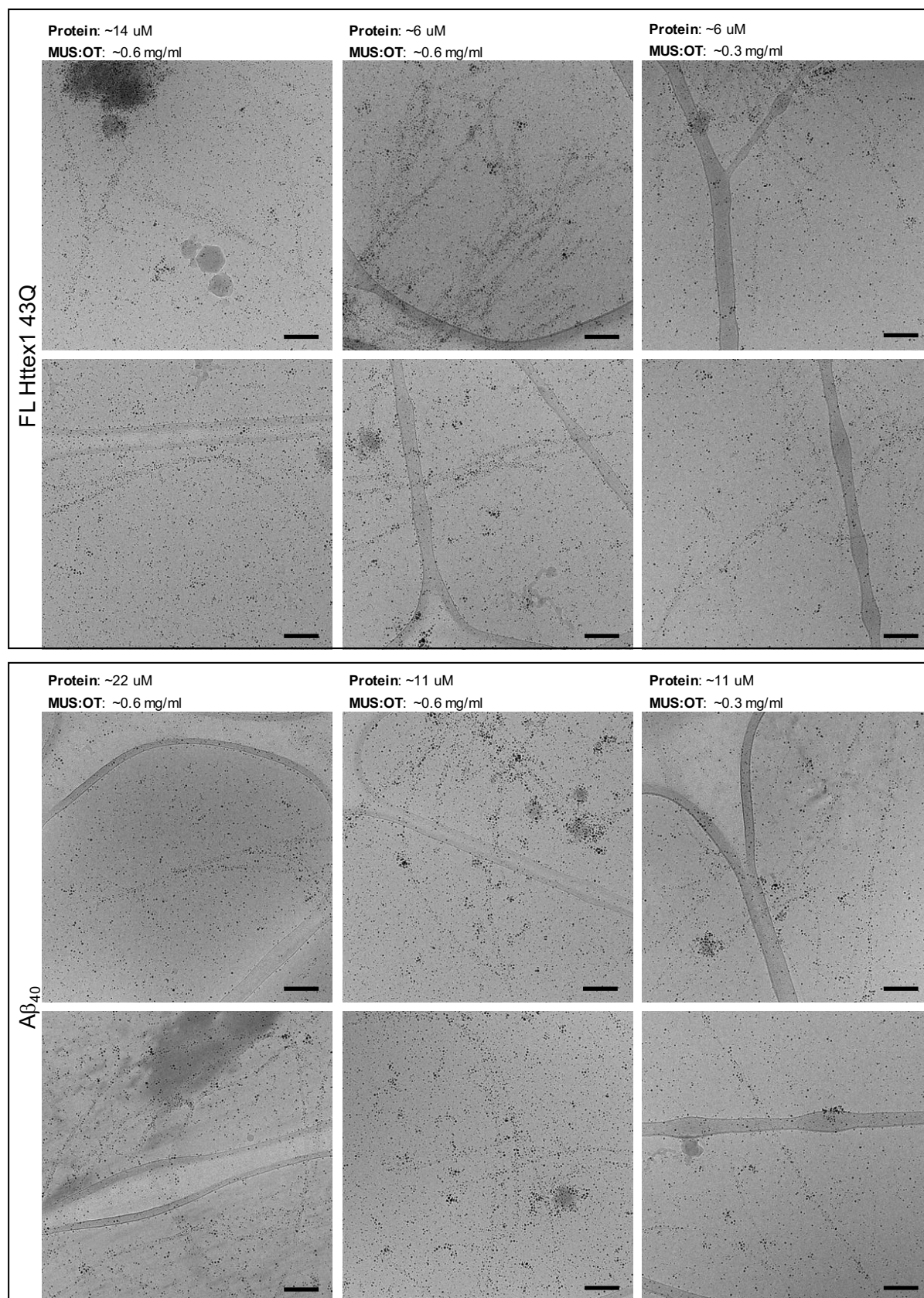


Figure 6.10 Cryo TEM images presenting the concentration assay of labelling FL Httex1 43Q and Aβ₄₀ fibrils with MUS:OT nanoparticles in the presence of CSF. Scale bars are 100 nm.

The same procedure was repeated for α -synuclein fibrils, which were mixed with CSF in the same ratio as FL Httex1 43Q and A β ₄₀ fibrils. Co-incubation of α -synuclein, MUS:OT and CSF resulted in visible precipitation in the vial. Despite that, cryo TEM images showed easily discernible in the ice, densely decorated amyloid fibrils (Figure 6.11). α -synuclein fibrils unlike FL Httex1 43Q and A β ₄₀ amyloids, shown in the Figure 6.10, are surrounded with little contamination and free nanoparticles. This behavior can be explained by the different buffer used for storage of the fibrils. Both FL Httex1 43Q and A β ₄₀ fibrils were stored and diluted in PBS buffer, whereas α -synuclein was diluted with TBS buffer. Both of these buffers contain different buffering agents. PBS contains phosphates (disodium phosphate and monopotassium phosphate). TBS is based on tris(hydroxymethyl)aminomethane, which contains an amine group. These slight differences in the buffer composition may affect the behavior of the sample mixed with CSF and nanoparticles. Regardless the difference in the buffers, we still obtained labeling of α -synuclein fibrils, of quality comparable with the labelling obtained without other biomolecules in the sample and shown in Chapter 3.

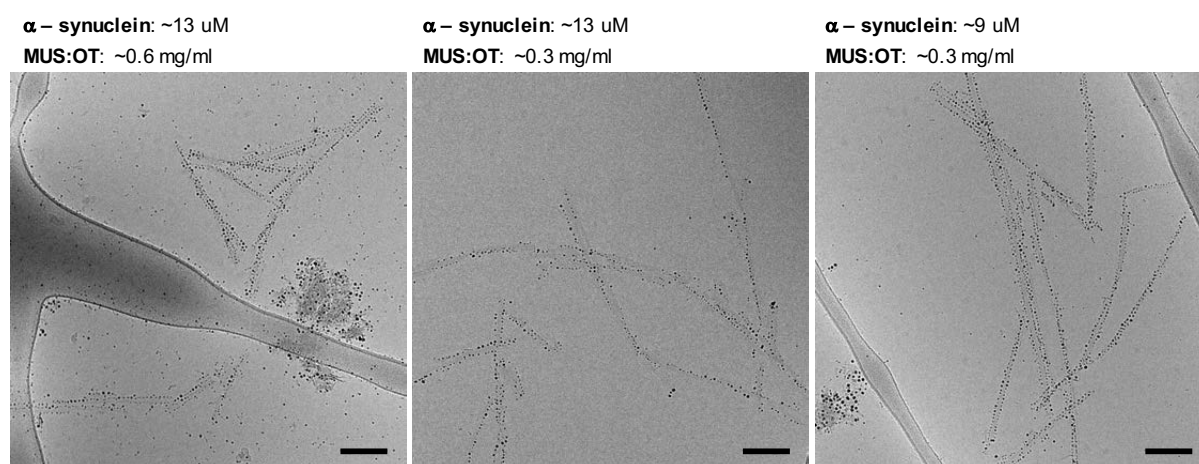


Figure 6.11 Cryo TEM images of concentration assay of α -synuclein fibrils decorated with MUS:OT nanoparticles in the presence of CSF. Scale bars are 100 nm.

We obtained labelling of each type of the amyloid fibrils mixed with CSF, that allowed for easy detection of these fibrils in the solution. The quality of the decoration was strongly depended on the ratio between the nanoparticles and amount of the amyloid fibrils. Despite that, we were able to visualize fibrils decorated with nanoparticles in every case. This shows that our nanomaterial can be used with success for labelling various amyloid fibrils in more challenging and biologically complex solutions.

6.3 Conclusions

Decoration of amyloid fibrils with our nanomaterial is resistant to various changes of the environment and harsh treatments, such as pH modification, dilution, centrifugation and sonication. Labelling of the fibrils can also be conducted in buffers with not only various NaCl concentrations, but different components, as shown in the case of PBS and TBS buffer. Moreover, labeling with our gold nanoparticles is not prone to changes upon addition of other biomolecules, such as BSA or cell debris. We also found out, that gold nanoparticles may serve as a selective contrast marker for detecting amyloid fibrils in a crowded biological solution. Omitting the negative staining step, eliminated the dark background that is composed of various stained cell components, leaves only amyloid fibrils decorated with nanomaterial to be easily discernable on the grid.

This makes MUS:OT and fractionated allMUS nanoparticles a good candidate for amyloid labelling material, which can be used in complex solutions. The experiments we performed, included tests in media, cell debris and CSF. In each case we observed labelled amyloid fibrils, however the efficiency and quality of this labelling was strongly depended on the concentration of nanomaterial. This is the result of various biomolecules present in the solution, that are able to capture and immobilize free nanoparticles minimizing their number in the solution and availability for the amyloid decoration.

Results presented in this chapter certainly show, that labeling with our gold nanomaterial is durable to various sample treatments and can be used in complex biological solutions. This makes it a potential tool for direct visualization and detection of the amyloid fibrils formed in an entire variety of *in vitro* conditions and biologically complex *in vivo* systems.

6.4 Materials and methods

Nanoparticles

Nanoparticles were prepared, characterized and fractionated as described in the Chapter 3.

Huntingtin exon 1 (Httex 1)

Both fibril types: N-truncated 43Q (with the first 17 amino acids removed) and full length 43Q Httex1 were prepared according to a previously reported protocol (152) and described in Chapter 3.

Wild type α -synuclein

Wild type α -synuclein fibrils were obtained as described in Chapter 3.

A β ₄₀ fibrils

A β ₄₀ samples were prepared according to the previously reported protocol (164) and described in Chapter 3.

Pre-decoration with nanoparticles of the amyloid fibrils for detachment tests

Mature amyloid fibrils, prepared as described above, were dispersed in their corresponding buffer and incubated at 37°C in a thermomixer with a water solution of nanoparticles. The samples were incubated for a period of 24 h to 72 h under the shaking speed in the range 300 rpm - 600 rpm. At the end of incubation, samples were gently resuspended using a pipette to generate some agitation immediately prior to cryo grid preparation.

Cell debris

Cell debris was obtained with use of VERO cells (African green monkey kidney). Cells were propagated in Dulbecco's modified Eagles medium (DMEM) supplemented with heat-inactivated 10% fetal bovine serum (FBS) and 1% penicillin/streptomycin (P/S) at 37°C in an atmosphere of 5 % of CO₂. Cells were passaged every 2-3 days using trypsin to detach from the flask and re-dispersed in same media. Cells were a gift from Matteo Gasbarri. Prior the experiment, cells were harvested from the single flask and centrifuged for 45 minutes under 5k rpm in order to break the membranes and obtain the pellet. Only the volume of the supernatant corresponding with the size of the pellet was kept, the rest of the supernatant was discarded. Usually 5 ml of harvested cell solution in the media yielded in around 100 μ l pellet size, that

was later resuspended in the 100 μ l of the remaining supernatant. This concentrated cell debris was later used in the experiments.

Cerebrospinal fluid

CSF was a generous gift from prof. Hilal Lashuel.

Decoration with nanoparticles of the amyloid fibrils in the complex solutions

Mature amyloid fibrils were mixed with the cell debris or CSF in order to achieve the desirable concentration. On top of that, water solution of highly concentrated nanoparticles (5 mg/ml - 10 mg/ml) was added and incubated at 20°C in a thermomixer for the period of 48h under the 450 rpm shaking. At the end of the incubation, samples were gently resuspended using a pipette to generate some agitation immediately prior to cryo grid preparation.

Negative stain TEM of amyloids

Recombinant samples were deposited onto glow-discharged 400-mesh carbon-supported copper grids for 1.5 min at room temperature. The grids were then blotted with filter paper, washed once with MilliQ water and stained with a 1% w/v uranyl acetate solution for 30 s. The blotted grids were air-dried and imaged using an FEI TALOS electron microscope at an acceleration voltage of 200 kV and equipped with a Ceta CCD camera or FEI Tecnai F20 electron microscope operated at 80 kV and equipped with Ceta CCD camera.

Cryo electron microscopy of amyloid and nanoparticle samples

For cryo TEM microscopy, a 3 μ l droplet of sample containing amyloids and nanoparticles suspended in buffer was deposited onto a lacey carbon film (Electron Microscopy Sciences) and blotted to a thin (100-300 nm) layer of liquid that was flash frozen in liquid ethane using an FEI Vitrobot Mark IV. Imaging was performed using a Gatan single tilt cryo holder operated on an FEI Tecnai F20 80 kV transmission electron microscope in LowDose Mode to visualize the samples at an average exposure of 1-3 electrons/ \AA^2 on a Ceta camera.

Chapter 7

Conclusions and outlook

7.1 Summary and conclusions

Small gold nanoparticles coated with suitable ligands are capable of adsorption to several types of amyloid fibrils, resulting in a strong increase of their contrast during Cryo TEM measurements. This contrast allows for the rapid determination of the polymorphic forms in a single image without extensive data processing. We found that MUS:OT nanoparticles label amyloid fibrils in a similar manner to fractionated allMUS fibrils, however they tend to decorate fibrils more densely. This propensity may originate from the presence of hydrophobic OT in the ligand shell and highlights the importance of the hydrophobic interactions between the fibrils and the gold label. We found out, that the adsorption of these nanoparticles onto the amyloid fibrils is resistant to various sample treatments, such as centrifugation, sonication, dilution or changes in the pH. This makes our nanomaterial a reliable contrast marker, which can be used in diverse conditions.

With the use of these two types of nanoparticles we were able to decorate amyloid fibrils in a specific manner. Our nanomaterial labelled them at the edges, in most of the cases. Among tested amyloids, NT Httex1 43Q was the least efficiently decorated, probably due to the removal of positively charged N17 terminus. This suggests its significant influence on the Httex1 43Q amyloid surface. We could also identify a difference in the labelling between amyloids prepared from the wild type and the modified α – synuclein protein. This indicates that MUS:OT and fractionated allMUS nanoparticles can be used as a probing and diagnostic tool for various types of amyloids.

Our gold nanoparticles enabled rapid assessment of the morphological details, such as the presence of a twist or periodicity length, for A β ₄₀ and R2 fibrils obtained *in vitro*. These differences in fibrils may be connected with specific polymorphic types present in the sample. Despite the good labelling of both of these amyloids, a specific fibril polymorph existing in the R2 sample could not be decorated, even when increasing the concentration of nanoparticles. This may stem from the different surface properties between different polymorphs. Indeed,

different amino acids may be exposed at the polymorphs' surfaces, resulting in different interaction with the nanoparticles. This selectivity could potentially be used in the differentiation and separation of the certain polymorphic species present in the same sample.

Moreover, analysis of the labelled amyloid fibrils prepared *in vitro*, showed strict correlation between the length of the periodicity and fibril width. This observation was previously reported and described by Adamcik et al., who correlated the geometry of the twist with the number of protofibrils constituting a mature fibril (139). Our procedure was also used to assess the morphology and polymorphism of *ex vivo* derived samples, as demonstrated with the amyloids made of (I) native PHFs obtained from the human brain, (II) a fragment of the lambda light chain derived from a patient's heart and (III) two types of transthyretin amyloids. In most of the cases, the image quality is strikingly similar to the images of *in vitro* amyloids. In the case of *ex vivo* derived amyloids however, all measured amyloids exhibited remarkable uniformness. This finding highlights the influence of the milieu on amyloid aggregation, which may be linked with the existence of only one amyloid fibril type.

Ex vivo derived material is usually contaminated by other proteins and macromolecular structures, such as exosomes and cell debris. Our system proved to be robust despite the contamination, as the fibrils could be selectively highlighted from the contaminants due to the decoration with nanoparticles. Moreover, we tested our nanoparticles in a more complex solutions and we managed to get labelling of the fibrils mixed with the concentrated cell debris and cerebrospinal fluid. This finding suggests, that our gold nanoparticles can be potentially used for rapid decoration of fibrils directly derived *ex vivo*.

We have developed a very effective, easy and fast tool to differentiate between various amyloid types, even in the presence of contamination. We could label amyloids fibrils prepared *in vitro* as well as derived from patients. We believe that this method could represent a breakthrough in the determination of morphological polymorphism for amyloid fibrils. Cryo TEM remains a sophisticated technique, that requires highly developed infrastructure and qualified personnel. However, with the use of our nanomaterial, some of the limitations, such as extensive time of the measurement and number of required images, can be alleviated. Importantly, our method does not require enrichment, seeding, or any other forms of purification. These nanoparticles could become a key labelling tool for biopsies of patients.

7.2 Outlook

This thesis showed how the work initiated by Dr. Paulo H. Jacob Silva was further expanded and systematized. Possible applications of our gold nanoparticles in the amyloid studies are not yet depleted. Gold nanoparticles can be applied in other approaches that could help in the understanding of amyloid morphological polymorphism, dynamics and possible connection of specific amyloid strains with the pathological states in the organism. Here we present three promising directions of research, in which our gold nanoparticles could be successfully applied in the future.

7.2.1 Amyloid growth and behavior monitoring with the use of liquid cell TEM

Cryo TEM technique offers a good preservation of the biological samples by snap freezing sensitive specimens in a thin layer of vitreous ice. Sample prepared in this way is more protected from the high vacuum inside the electron microscope and from the damage caused by the electron beam (96, 199). These advantages placed cryo TEM technique among the most often used techniques for studying numerous biological structures. However, due to the immobilization in ice, studying dynamic interactions and processes of these structures in real time is not possible with use of cryo TEM.

Liquid cell TEM technique can address this limitation. In this technique, the sample is confined in a small chamber of electron transparent walls (window), which can endure high differences of pressure between the inside and outside of the chamber (Figure 7.1). This technique allows for controlling the sample temperature and measurement in the static or flowing liquid (200). Liquid cell TEM technique already found successful applications in electrochemistry, nanoparticles research, studies of liquids and in life sciences (201). Measurement of whole cells and small biostructures were reported with the use of liquid cell TEM (200, 202).

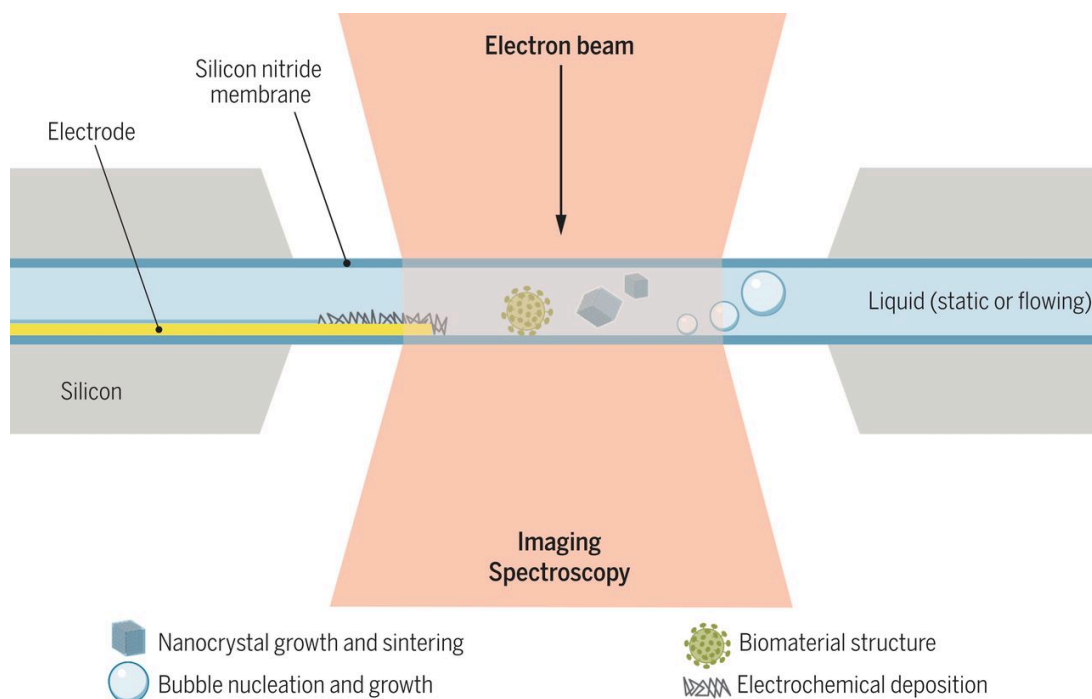


Figure 7.1 Schematic representation of liquid cell TEM measurement and its possible applications. Reprinted with the permission from (200).

Alas, cell building material and the solution present inside limit resolution of the liquid TEM. Moreover, due to the difference in the pressure, the walls of the liquid TEM cell very often bulge outward, which results in a thicker layer of the liquid in the middle of the cell window, where also more material tends to aggregate. Another drawback is the radiation of the liquid sample under the electron beam, which can lead to hydrogen gas production. These limitations are proportional to the dose rate or illuminated area (200, 202, 203). Application of our gold nanoparticles can address these issues by increasing the contrast of the measured structure, that would limit the dose and speed up the screening process.

Preliminary data obtained on FL Httex1 43Q labelled with MUS:OT nanoparticles imaged via liquid cell Scanning Transmission Electron Microscopy (STEM) were very promising. We were able to capture multiple images of the sample in short time and record a movie of freely floating fibrils and bigger aggregates decorated with the gold nanoparticles (Figure 7.2).

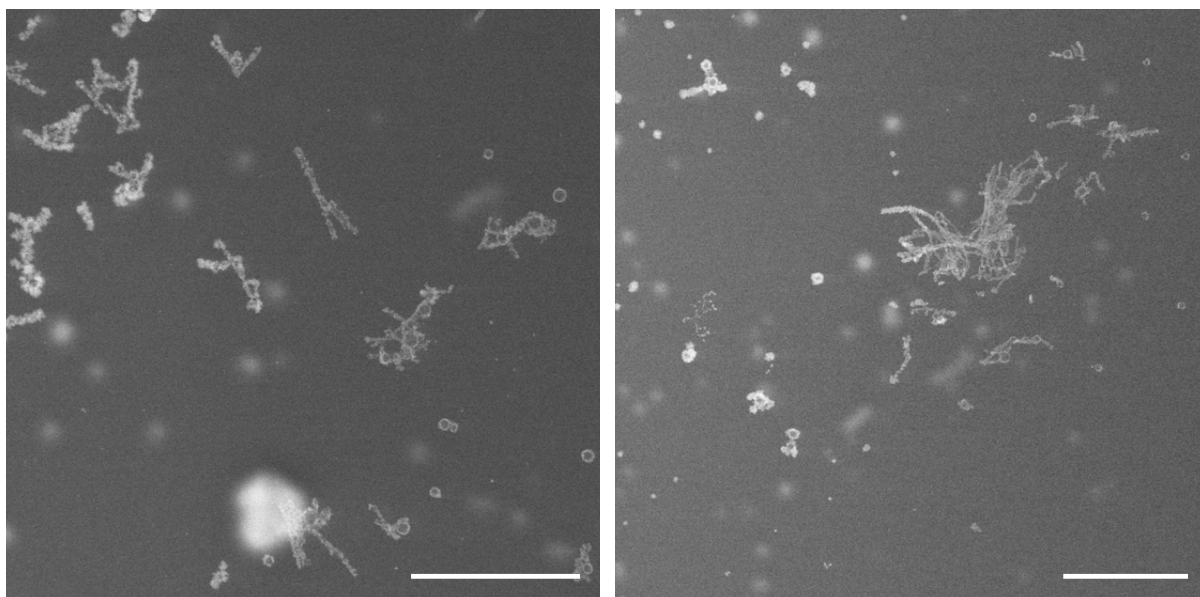


Figure 7.2 Liquid cell STEM images of MUS:OT labelled FL Httex1 43Q fibrils. Fibrils with the higher sharpness are in the focal plane, while blurred fibrils are out of focus which highlights their spatial 3D orientation and free movement in the liquid. Scale bars are 1 μm .

Proteinaceous structures are not apparent with the use of liquid cell STEM technique and the electron dense gold core provided excellent visibility of these structures. This result suggests that application of our gold nanoparticles in liquid cell TEM could possibly allow for the real-time observation of the aggregates formation of various amyloidogenic proteins. Moreover, these observations could be potentially expanded on the observation of degradation, kinetics or dynamics of the amyloid fibrils under various conditions.

7.2.2 Separation of amyloid polymorphic species with use of nanoparticles

In the course of this thesis we have shown how our gold nanoparticles decorate various amyloid fibrils. On the example of Httex1 43Q and α – synuclein we have shown how our nanomaterial labelled differently various types of amyloid fibrils generated from the same protein. Moreover, we obtained various level of labelling within the population of amyloids generated from the same peptide due to the morphology, as shown on the example of R2 fibrils.

This potential of selective decoration of amyloid fibrils can be used for the separation of certain polymorphs from the whole population present in an amyloid sample. This separation could be achieved by using the different mechanical properties of the fibrils decorated with gold nanoparticles, such as overall density or flow rate (204). Labelled fibrils could also be separated from the bare fibrils with use of the different chemical properties of gold nanoparticles, such as limited solubility in certain solvents (Figure 7.3).

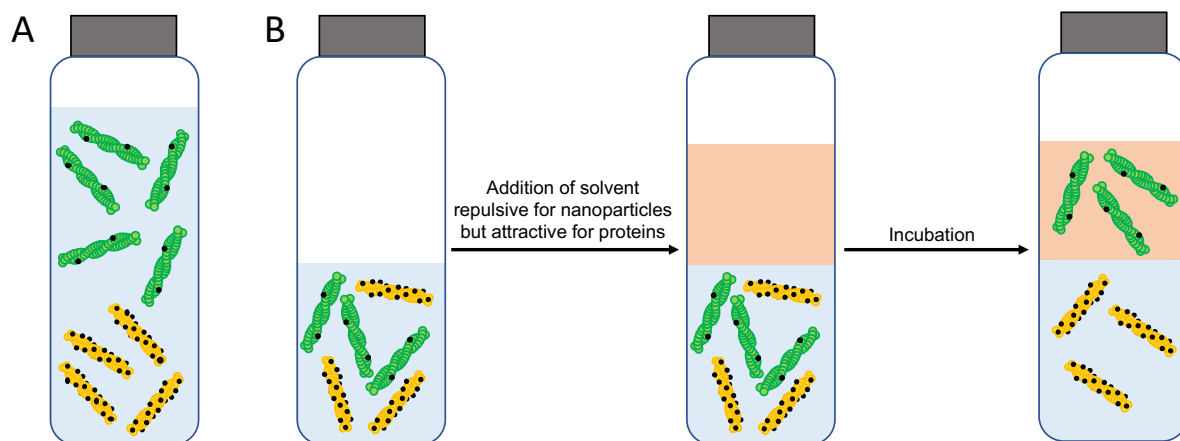


Figure 7.3 Schematic cartoons showing possible way of separating amyloid fibrils due to their decoration or lack of thereof. A) Separation due to the different density of the fibrils, where heavier gold labelled fibrils would sediment faster than bare fibrils. B) Separation due to the solubility difference between bare amyloids and amyloids decorated with gold nanoparticles with specific ligand composition.

Modification of the gold nanoparticles, such as functionalization with ligands that could potentially stick to the flushed surface, would allow for another way of bare amyloid fibrils separate from the decorated ones. For example, nanoparticles coupled with biotin, what would attach to the amyloid fibrils, interact with the streptavidin present in the column or elsewhere, and could immobilize only labelled fibrils. Apart from the ligand shell, the core of nanoparticles could also be modified in order to assist and perform the separation. One of the possible modifications would be to introduce magnetic properties to the nanoparticles and further immobilize labelled amyloids with the application of a magnetic field (Figure 7.4).

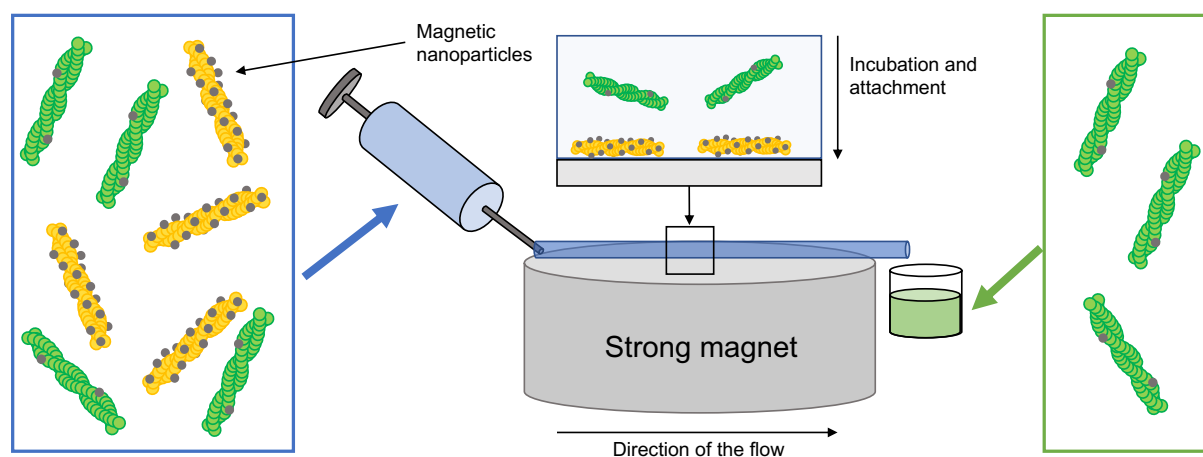


Figure 7.4 Schematic cartoon representing ideal separation of amyloid fibrils due to the magnetic properties of nanoparticles.

The separation of amyloid fibrils from the solution with use of magnetic nanoparticles was previously reported, however these approaches were not polymorphism specific and were focused on the removal of the overall population of the amyloid fibrils from the sample (119, 120).

Preliminary results shown that amyloid fibrils were successfully decorated with allMUS and MUS:OT nanoparticles of a gold core doped with iron atoms (Au/Fe) (Figure 7.5).

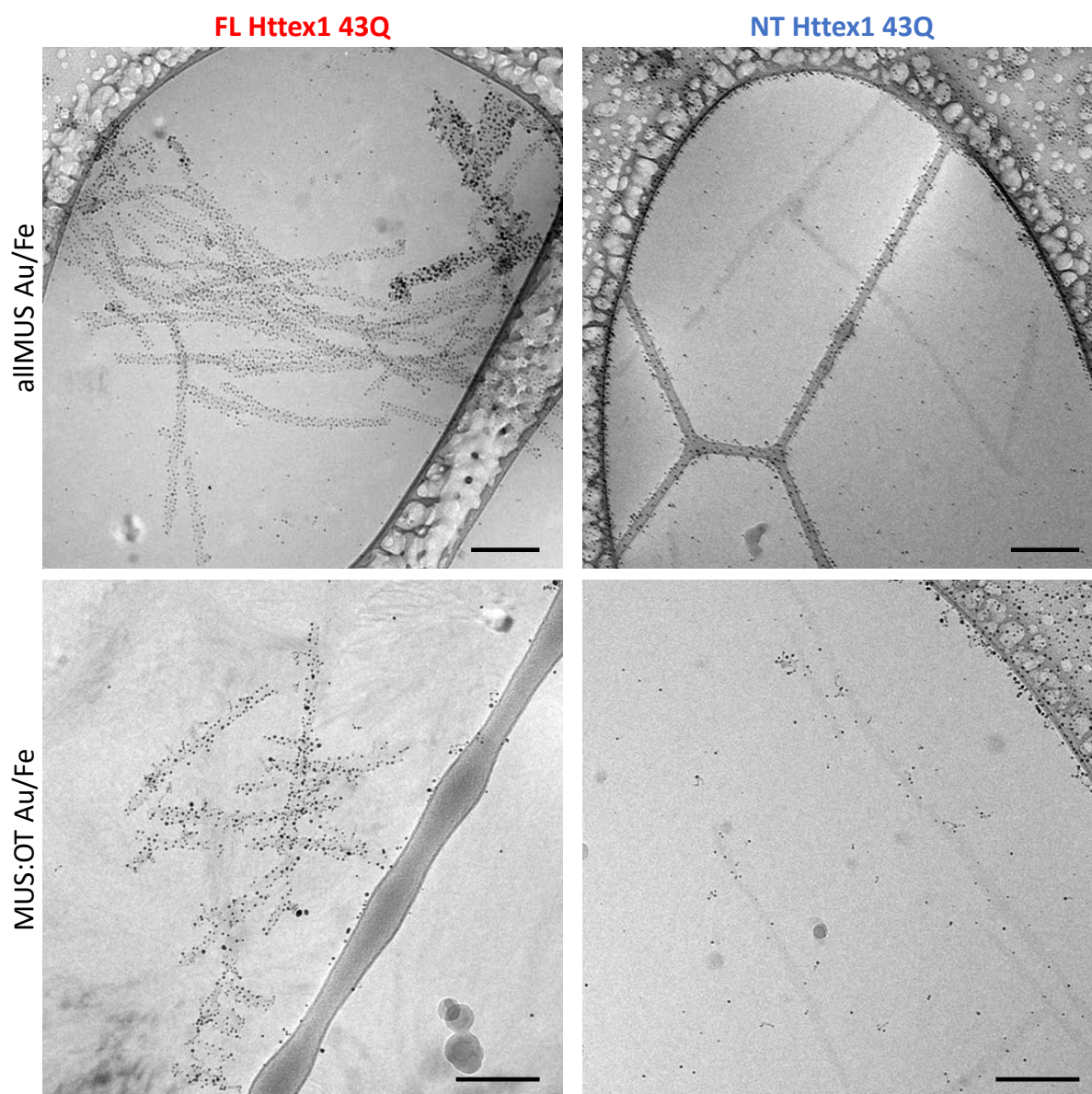


Figure 7.5 Cryo TEM images of Httex 43Q fibrils decorated with the nanoparticles of the gold core doped with iron atoms. Ligand shell composition of AuFe nanoparticles was corresponding to the ligands of nanoparticles showed in the Chapter 4. The mode of labelling with AuFe nanoparticles resembled the results showed in Chapter 4. Scale bars are 100 nm.

This suggests, that the composition of the core does not play significant role in the fibril decoration and the selectivity of our nanoparticles may mostly depend from their size and ligand composition. Magnetic properties of Au/Fe nanoparticles were too weak to perform successful separation of the fibrils. Possible modification of these nanoparticles would have to employ nanoparticles with a strongly magnetic core while still keeping the gold coated surface, which would allow the attachment of the thiolated ligands. To ensure more selective binding, the average size of the nanoparticles would have to not exceed the 5 nm diameter (205).

Successful separation of the specific polymorphic species would allow for further studies, such as cytotoxicity, kinetics or stability assays of one specific polymorphic type of the fibrils, instead of the whole population. This possibility would be of a great relevance in the process of understanding the influence of the specific polymorphic types on the disease onset.

7.2.3 Facilitating microscopy studies of *ex vivo* derived amyloids and *in vivo* studies of aggregates

Our gold nanomaterial can be successfully used for studying human derived amyloids. As shown in Chapter 6, MUS:OT and fractionated allMUS nanoparticles attach to the surface of human derived amyloids in a selective fashion delineating their contour. Moreover, we could obtain this effect even for samples contaminated with cell debris. Our gold nanomaterial is binding selectively to the amyloids and can be used for imaging unpurified samples containing fibrils. This introduces the possibility of a quick imaging of freshly obtained samples without the need of storage and extensive treatment prior to the microscopy procedure, which limits the introduction of artefacts or modification of the fibrils during the process. The simplicity of our system and compatibility with simple cryo TEM setups, enables for the quick sample screening prior to more complicated measurements.

As shown in the Chapter 3, MUS:OT nanoparticles can label amyloid fibrils in the presence of all, highly concentrated cell components. This could allow for the immediate labelling of the amyloid fibrils accumulated in the cell (Figure 7.6).

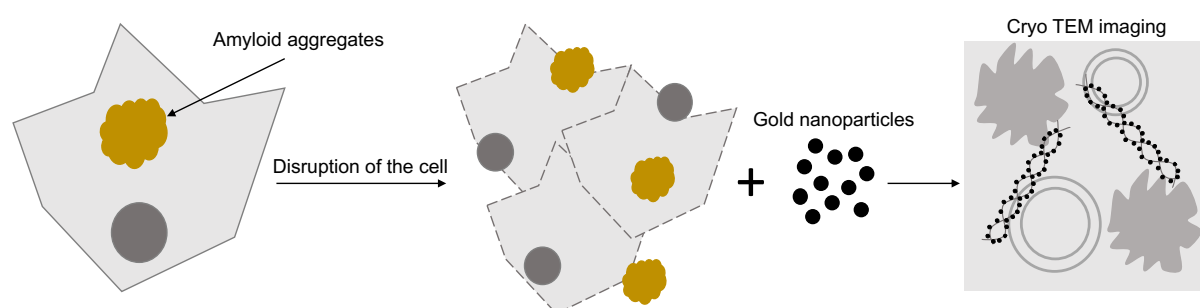


Figure 7.6 Schematic cartoon showing labelling with gold nanoparticles amyloid fibrils directly derived from the cell inside.

Previous studies shown that our gold nanoparticles can be internalized by cells without membrane disruption and with minimal toxicity. Moreover, these nanoparticles can be labelled with thiolated BODIPY dye, which enables their tracking and visualization with the use of fluorescent microscope (206). This propensity can be used for detecting and visualizing amyloid aggregates inside the cells.

7.2.4 Materials and methods

Preparation of Httex1 43Q fibrils

FL Httex1 43Q fibrils amyloid fibrils were prepared by Dr. Sophie Vieweg as previously described in the Chapter 4. Mature amyloids were diluted to the concentration 5 μ M and mixed with 1 mg/ml concentrated nanoparticles in the ratio 9:1. Incubation was conducted for 24 hours in 37°C and with 450 rpm agitation.

Experimental conditions for amyloid characterization in liquid cell TEM

FL Httex 43Q sample was measured on the TEM liquid – electrochemical holder (Hummingbird Scientific, Lacey, WA, USA) for characterization in TEM. In order to remove big aggregates and long fibrils that could block the outlets and inlets of the liquid cell, the sample was sonicated for 5 seconds before the experiment. Next, 60 μ l of sonicated solution was pipetted and dropped on a 2 μ m spacer before closing the liquid cell with a chip. The 50 nm SiNx windows on both the spacer and the chip were overlapped for having the liquid chamber electron transparent. Diluted buffer or water was introduced into the sealed liquid chamber by a syringe through the microfluidic tube in the holder during imaging.

JEOL-2200FS 200kV field emission gun (FEG) (scanning) transmission electron microscope (S)TEM was used for imaging the assembly and dynamics of amyloid fibrils decorated with gold nanoparticles. The low dose TEM video was collected by the direct electron detection camera (DE-16). Measurement was performed by Jing Hou.

Synthesis of AuFe nanopartciles

Synthesis of AuFe nanoparticles was conducted by Dr. Paulo H. Jacob Silva according to the protocol described in (207).

References

1. T. Richel, Will Human Life Expectancy Quadruple in the Next Hundred Years? Sixty Gerontologists Say Public Debate on Life Extension Is Necessary. *J. Anti. Aging. Med.* **6**, 309–314 (2003).
2. R. Holliday, Aging is No Longer an Unsolved Problem in Biology. *Ann. N. Y. Acad. Sci.* **1067**, 1–505 (2006).
3. N. R. Sahyoun, H. Lentzner, D. Hoyert, K. N. Robinson, Trends in causes of death among the elderly. *Aging Trends*, 1–10 (2001).
4. S. E. Tom, *et al.*, Characterization of dementia and Alzheimer's disease in an older population: Updated incidence and life expectancy with and without dementia. *Am. J. Public Health* **105**, 408–413 (2015).
5. S. T. Read, C. Toye, D. Wynaden, Experiences and expectations of living with dementia: A qualitative study. *Collegian* **24**, 427–432 (2016).
6. F. O. Walker, Huntington's disease. *Lancet* **369**, 218–228 (2007).
7. B. Winblad, *et al.*, Defeating Alzheimer's disease and other dementias: A priority for European science and society. *Lancet Neurol.* **15**, 455–532 (2016).
8. A. Wimo, *et al.*, The economic impact of dementia in Europe in 2008-cost estimates from the Eurocode project. *Int. J. Geriatr. Psychiatry* **26**, 825–832 (2011).
9. S. Pillemer, J. Davis, G. Tremont, Gender effects on components of burden and depression among dementia caregivers. *Aging Ment. Health* **0**, 1–6 (2017).
10. G. Quaglio, H. Brand, C. Dario, Fighting dementia in Europe: The time to act is now. *Lancet Neurol.* **15**, 452–454 (2016).
11. Alzheimer's Association, 2015 Alzheimer's disease facts and figures. *Alzheimers. Dement.* **11**, 332–84 (2015).
12. S. Treusch, D. M. Cyr, S. Lindquist, Amyloid deposits : Protection against toxic protein species? **4101** (2009).
13. J. T. Bendor, T. P. Logan, R. H. Edwards, The function of α -synuclein. *Neuron* **79**, 1044–1066 (2013).
14. J. Greenwald, R. Riek, Biology of amyloid: Structure, function, and regulation. *Structure* **18**, 1244–1260 (2010).
15. R. Khurana, V. N. Uversky, L. Nielsen, A. L. Fink, Is Congo Red an Amyloid-specific Dye? *J. Biol. Chem.* **276**, 22715–22721 (2001).
16. M. Biancalana, S. Koide, Molecular mechanism of Thioflavin-T binding to amyloid

- fibrils. *Biochim. Biophys. Acta - Proteins Proteomics* **1804**, 1405–1412 (2010).
17. F. Chiti, C. M. Dobson, Protein Misfolding, Functional Amyloid, and Human Disease. *Annu. Rev. Biochem.* **75**, 333–366 (2006).
 18. T. P. J. Knowles, M. Vendruscolo, C. M. Dobson, The amyloid state and its association with protein misfolding diseases. *Nat. Rev. Mol. Cell Biol.* **15**, 384–96 (2014).
 19. F. Chiti, C. M. Dobson, Protein Misfolding , Amyloid Formation , and Human Disease : A Summary of Progress Over the Last Decade. *Annu. Rev. Biochem.* **86**, 27–68 (2017).
 20. J. Adamcik, R. Mezzenga, Amyloid Polymorphism in the Protein Folding and Aggregation Energy Landscape. *Angew. Chemie - Int. Ed.* **57**, 8370–8382 (2018).
 21. R. Tycko, Amyloid Polymorphism: Structural Basis and Neurobiological Relevance. *Neuron* **86**, 632–645 (2015).
 22. J. Gath, *et al.*, Unlike twins: An NMR comparison of two α -synuclein polymorphs featuring different toxicity. *PLoS One* **9**, 1–11 (2014).
 23. I. Usov, R. Mezzenga, Correlation between nanomechanics and polymorphic conformations in amyloid fibrils. *ACS Nano* **8**, 11035–11041 (2014).
 24. W. Qiang, K. Kelley, R. Tycko, Polymorph-specific kinetics and thermodynamics of β -amyloid fibril growth. *J. Am. Chem. Soc.* **135**, 6860–6871 (2013).
 25. A. K. Paravastu, R. D. Leapman, W. Yau, R. Tycko, Molecular structural basis for polymorphism in Alzheimer ' s β -amyloid fibrils. *Proc. Natl. Acad. Sci. U. S. A.* **105**, 18349–18354 (2008).
 26. R. Kodali, A. D. Williams, S. Chemuru, R. Wetzel, A β (1-40) forms five distinct amyloid structures whose b-sheet contents and fibril stabilities are correlated. *J. Mol. Biol.* **401**, 503–517 (2010).
 27. L. Bousset, *et al.*, Structural and functional characterization of two alpha-synuclein strains. *Nat. Commun.* **4**:2575 (2013).
 28. A. G. Murzin, *et al.*, Heparin-induced tau filaments are polymorphic and differ from those in Alzheimer's and Pick's diseases. *Elife* **8**, 1–24 (2019).
 29. X. Ni, R. P. McGlinchey, J. Jiang, J. C. Lee, Structural Insights into α -Synuclein Fibril Polymorphism: Effects of Parkinson's Disease-Related C-Terminal Truncations. *J. Mol. Biol.* **431**, 3913–3919 (2019).
 30. J. Meinhardt, C. Sachse, P. Hortschansky, N. Grigorieff, M. Fändrich, A β (1-40) Fibril Polymorphism Implies Diverse Interaction Patterns in Amyloid Fibrils. *J. Mol. Biol.* **386**, 869–877 (2009).
 31. C. S. Goldsbury, G. J. S. Cooper, K. N. Goldie, S. A. Mu, Polymorphic Fibrillar

- Assembly of Human Amylin. **27**, 17–27 (1997).
32. A. W. P. Fitzpatrick, *et al.*, Cryo-EM structures of tau filaments from Alzheimer's disease. *Nature* **547**, 185–190 (2017).
 33. K. Annamalai, *et al.*, Polymorphism of Amyloid Fibrils in Vivo. *Angew. Chemie - Int. Ed.* **55**, 4822–4825 (2016).
 34. M. L. Cohen, *et al.*, Rapidly progressive Alzheimer's disease features distinct structures of amyloid- β . *Brain* **138**, 1009–1022 (2015).
 35. W. Qiang, W.-M. Yau, J.-X. Lu, J. Collinge, R. Tycko, Structural variation in amyloid- β fibrils from Alzheimer's disease clinical subtypes. *Nature* **541**, 217–221 (2017).
 36. J.-X. Lu, *et al.*, Molecular Structure of β -Amyloid Fibrils in Alzheimer's Disease Brain Tissue. *Cell* **154**, 1257–1268 (2013).
 37. J. S. Jeong, A. Ansaloni, R. Mezzenga, H. a. Lashuel, G. Dietler, Novel mechanistic insight into the molecular basis of amyloid polymorphism and secondary nucleation during amyloid formation. *J. Mol. Biol.* **425**, 1765–1781 (2013).
 38. B. Li, *et al.*, Cryo-EM of full-length α -synuclein reveals fibril polymorphs with a common structural kernel. *Nat. Commun.* **9**, 3609 (2018).
 39. D. Whitford, *Proteins Structure and Function* (John Wiley & Sons Ltd, 2005).
 40. C. M. Dobson, A. Šali, M. Karplus, Protein folding: A perspective from theory and experiment. *Angew. Chemie - Int. Ed.* **37**, 868–893 (1998).
 41. C. M. Dobson, Protein folding and misfolding. *Nature* **426**, 884–890 (2003).
 42. C. M. Dobson, Principles of protein folding, misfolding and aggregation. *Semin. Cell Dev. Biol.* **15**, 3–16 (2004).
 43. A. R. Dinner, A. Sali, L. J. Smith, C. M. Dobson, Understanding protein folding via free-energy surfaces from theory and experiment. *Trends Biochem. Sci.* **107**, 355–371 (2000).
 44. P. G. Wolynes, J. N. Onuchic, D. Thirumalai, Navigating the Folding Routes. *Science (80-.)*. **267** (1995).
 45. D. Balchin, M. Hayer-Hartl, F. U. Hartl, In vivo aspects of protein folding and quality control. *Science (80-.)*. **353** (2016).
 46. I. Moreno-Gonzalez, C. Soto, Misfolded protein aggregates: Mechanisms, structures and potential for disease transmission. *Semin. Cell Dev. Biol.* **22**, 482–487 (2011).
 47. R. Sarroukh, E. Goormaghtigh, J.-M. Ruysschaert, V. Raussens, ATR-FTIR: A “rejuvenated” tool to investigate amyloid proteins. *Biochim. Biophys. Acta - Biomembr.* **1828**, 2328–2338 (2013).

48. C. Lonescu-Zanetti, *et al.*, Monitoring the assembly of Ig light-chain amyloid fibrils by atomic force microscopy. *Proc. Natl. Acad. Sci. U. S. A.* **96**, 13175–13179 (1999).
49. R. Khurana, *et al.*, A general model for amyloid fibril assembly based on morphological studies using atomic force microscopy. *Biophys. J.* **85**, 1135–1144 (2003).
50. A. M. Morris, M. A. Watzky, R. G. Finke, Protein aggregation kinetics, mechanism, and curve-fitting: A review of the literature. *Biochim. Biophys. Acta - Proteins Proteomics* **1794**, 375–397 (2009).
51. R. Morales, I. Moreno-gonzalez, C. Soto, Cross-Seeding of Misfolded Proteins : Implications for Etiology and Pathogenesis of Protein Misfolding Diseases. **9**, 1–4 (2013).
52. T. Eichner, S. E. Radford, A Diversity of Assembly Mechanisms of a Generic Amyloid Fold. *Mol. Cell* **43**, 8–18 (2011).
53. Q. Shu, *et al.*, Solution NMR structure of CsgE: Structural insights into a chaperone and regulator protein important for functional amyloid formation. *Proc. Natl. Acad. Sci.* **113**, 201607222 (2016).
54. D. Eisenberg, M. Jucker, The Amyloid State of Proteins in Human Diseases. *Cell* **148**, 1188–1203 (2012).
55. A. D. Wechalekar, J. D. Gillmore, P. N. Hawkins, Systemic amyloidosis. *Lancet* **387**, 2641–2654 (2016).
56. S. Sadigh-Eteghad, *et al.*, Amyloid-beta: A crucial factor in Alzheimer's disease. *Med. Princ. Pract.* **24**, 1–10 (2015).
57. B. De Strooper, E. Karran, The Cellular Phase of Alzheimer's Disease. *Cell* **164**, 603–615 (2016).
58. D. J. Selkoe, J. Hardy, The amyloid hypothesis of Alzheimer's disease at 25 years. *EMBO Mol. Med.* **8**, 595–608 (2016).
59. W. Peelaerts, L. Bousset, V. Baekelandt, R. Melki, α -Synuclein strains and seeding in Parkinson's disease, incidental Lewy body disease, dementia with Lewy bodies and multiple system atrophy: similarities and differences. *Cell Tissue Res.* **373**, 195–212 (2018).
60. D. J. Irwin, V. M.-Y. Lee, J. Q. Trojanowski, Parkinson's disease dementia: convergence of α -synuclein, tau and amyloid- β pathologies. *Nat. Rev. Neurosci.* **14**, 626–636 (2013).
61. A. D. Cohen, R. L. Comenzo, Systemic Light-Chain Amyloidosis : Advances in Diagnosis , Prognosis , and Therapy Introduction : A Proteotoxic Clonal Plasma Cell.

- Hematology*, 287–294 (2010).
62. K. Sivakumar, M. C. Dalakas, Inclusion body myositis and myopathies. *Curr. Opin. Neurol.* **10**, 413–420 (1997).
 63. L. Obici, V. Perfetti, G. Palladini, R. Moratti, G. Merlini, Clinical aspects of systemic amyloid diseases. *Biochim. Biophys. Acta - Proteins Proteomics* **1753**, 11–22 (2005).
 64. J. A. Vrana, *et al.*, Classification of amyloidosis by laser microdissection and mass spectrometry-based proteomic analysis in clinical biopsy specimens. *Blood* **114**, 4957–4959 (2009).
 65. C. L. Murphy, S. Wang, T. Williams, D. T. Weiss, A. Solomon, Characterization of Systemic Amyloid Deposits by Mass Spectrometry. *Methods Enzymol.* **412**, 48–62 (2006).
 66. A. Drzezga, Amyloid-plaque imaging in early and differential diagnosis of dementia. *Ann. Nucl. Med.* **24**, 55–66 (2010).
 67. D. Azria, S. Blanquer, J.-M. Verdier, E. Belamie, Nanoparticles as contrast agents for brain Nuclear Magnetic Resonance Imaging in Alzheimer Disease diagnosis. *J. Mater. Chem. B* (2017) <https://doi.org/10.1039/C7TB01599B>.
 68. S. Palmqvist, *et al.*, Accuracy of brain amyloid detection in clinical practice using cerebrospinal fluid β -Amyloid 42: A cross-validation study against amyloid positron emission tomography. *JAMA Neurol.* **71**, 1282–1289 (2014).
 69. O. El-Agnaf, S. Nagala, B. Patel, B. Austen, Non-fibrillar oligomeric species of the amyloid ABri peptide, implicated in familial British dementia, are more potent at inducing apoptotic cell death than protofibrils or mature fibrils. *J. Mol. Biol.* **310**, 157–168 (2001).
 70. C. S. Goldsberry, *et al.*, Studies on the in vitro assembly of A β 1-40: Implications for the search for A β fibril formation inhibitors. *J. Struct. Biol.* **130**, 217–231 (2000).
 71. C. Duran-Aniotz, R. Morales, I. Moreno-Gonzalez, P. P. Hu, C. Soto, Brains from non-Alzheimer's individuals containing amyloid deposits accelerate A β deposition in vivo. *Acta Neuropathol. Commun.* **2**, 1–11 (2014).
 72. G. Yoon, M. Lee, J. I. Kim, S. Na, K. Eom, Role of sequence and structural polymorphism on the mechanical properties of amyloid fibrils. *PLoS One* **9**, 1–13 (2014).
 73. W. Qiang, K. Kelley, R. Tycko, Polymorph-Specific Kinetics and Thermodynamics of β - Amyloid Fibril Growth (2013) <https://doi.org/10.1021/ja311963f>.
 74. A. T. Petkova, *et al.*, Self-Propagating , Molecular-Level Polymorphism in Alzheimer '

- s β -Amyloid Fibrils. *Science* (80-.). **307**, 261–265 (2005).
75. G. Heilbronner, *et al.*, Seeded strain-like transmission of β -amyloid morphotypes in APP transgenic mice. *EMBO Rep.* **14**, 1017–1022 (2013).
 76. A. S. Cohen, E. Calkins, Electron Microscopic Observations on a Fibrous Component in Amyloid of Diverse Origins. *Nature*, 1202–1203 (1959).
 77. T. Shirahama, A. S. Cohen, Structure of Amyloid Fibrils after Negative Staining and High-resolution Electron Microscopy (1965).
 78. C. Goldsbury, P. Frey, V. Olivieri, U. Aepli, S. A. Müller, Multiple assembly pathways underlie amyloid- β fibril polymorphisms. *J. Mol. Biol.* **352**, 282–298 (2005).
 79. M. Fändrich, J. Meinhardt, N. Grigorieff, Structural polymorphism of Alzheimer A β and other amyloid fibrils. *Prion* **3**, 89–93 (2009).
 80. C. Seuring, *et al.*, Amyloid Fibril Polymorphism: Almost Identical on the Atomic Level, Mesoscopically Very Different. *J. Phys. Chem. B*, acs.jpcc.6b10624 (2017).
 81. J. L. Guo, *et al.*, Distinct α -Synuclein Strains Differentially Promote Tau Inclusions in Neurons. *Cell* **154**, 103–117 (2013).
 82. C. Peng, *et al.*, Cellular milieu imparts distinct pathological α -synuclein strains in α -synucleinopathies. *Nature* **557**, 558–563 (2018).
 83. C. Peng, R. J. Gathagan, V. M. Y. Lee, Distinct α -Synuclein strains and implications for heterogeneity among α -Synucleinopathies. *Neurobiol. Dis.* **109**, 209–218 (2018).
 84. D. W. Sanders, *et al.*, Distinct Tau Prion Strains Propagate in Cells and Mice and Define Different Tauopathies. *Neuron* **82**, 1271–1288 (2014).
 85. R. Tycko, Solid state NMR studies of amyloid fibril structure. *October*, 279–299 (2011).
 86. E. M. Sigurdsson, Ed., *Amyloid proteins methods and protocols*, First (Humana Press, 2005).
 87. R. Halfmann, S. Lindquist, Screening for amyloid aggregation by Semi-Denaturing Detergent-Agarose Gel Electrophoresis. *J. Vis. Exp.*, 20–22 (2008).
 88. D. Pinotsi, *et al.*, Direct observation of heterogeneous amyloid fibril growth kinetics via two-color super-resolution microscopy. *Nano Lett.* **14**, 339–345 (2014).
 89. M. R. Nilsson, Techniques to study amyloid fibril formation in vitro. *Methods* **34**, 151–160 (2004).
 90. X. chen Bai, G. McMullan, S. H. W. Scheres, How cryo-EM is revolutionizing structural biology. *Trends Biochem. Sci.* **40**, 49–57 (2014).
 91. W. Page Faulk, G. Malcolm Taylor, Communication to the editors. An immunocolloid method for the electron microscope. *Immunochimistry* **8**, 1081–1083 (1971).

92. D. S. Eisenberg, M. R. Sawaya, Structural Studies of Amyloid Proteins at the Molecular Level. *Annu. Rev. Biochem.* **86**, 69–95 (2017).
93. M. Zhu, P. O. Souillac, C. Ionescu-Zanetti, S. A. Carter, A. L. Fink, Surface-catalyzed amyloid fibril formation. *J. Biol. Chem.* **277**, 50914–50922 (2002).
94. M. Fändrich, M. Schmidt, N. Grigorieff, Recent progress in understanding Alzheimer's β -amyloid structures. *Trends Biochem. Sci.* **36**, 338–345 (2011).
95. M. Ohi, Y. Li, Y. Cheng, T. Walz, Negative staining and image classification—powerful tools in modern electron microscopy. *Biol. Proced. Online* **6**, 23–34 (2004).
96. C. J. Newcomb, T. J. Moyer, S. S. Lee, S. I. Stupp, Advances in cryogenic transmission electron microscopy for the characterization of dynamic self-assembling nanostructures. *Curr. Opin. Colloid Interface Sci.* **17**, 350–359 (2012).
97. M. Vilar, *et al.*, The fold of alpha-synuclein fibrils. *Proc. Natl. Acad. Sci. U. S. A.* **105**, 8637–42 (2008).
98. A. Ruivo, *et al.*, Gold nanoparticles in ancient and contemporary ruby glass. *J. Cult. Herit.* **9** (2008).
99. W. J. Stark, P. R. Stoessel, W. Wohlleben, A. Hafner, Industrial applications of nanoparticles. *Chem. Soc. Rev.* **44**, 5793–5805 (2015).
100. E. Boisselier, D. Astruc, Gold nanoparticles in nanomedicine: preparations, imaging, diagnostics, therapies and toxicity. *Chem. Soc. Rev.* **38**, 1759–1782 (2009).
101. T. Sun, *et al.*, Engineered nanoparticles for drug delivery in cancer therapy. *Angew. Chemie - Int. Ed.* **53**, 12320–12364 (2014).
102. M. De, P. S. Ghosh, V. M. Rotello, Applications of nanoparticles in biology. *Adv. Mater.* **20**, 4225–4241 (2008).
103. K. A. Howard, T. Vorup-jensen, *Nanomedicine*.
104. L. Zhang, *et al.*, Nanoparticles in Medicine: Therapeutic Applications and Developments. *Transl. Med.* **83**, 761–769 (2008).
105. S. Ov, Applications of nanoparticles in biology and medicine. *J. Nanobiotechnology* **6**, 1–6 (2004).
106. R. Nagarajan, Nanoparticles: Building blocks for nanotechnology. *ACS Symp. Ser.* **996**, 2–14 (2008).
107. J. L. Gilmore, X. Yi, L. Quan, A. V. Kabanov, Novel nanomaterials for clinical neuroscience. *J. NeuroImmune Pharmacol.* **3**, 83–94 (2008).
108. P. Polak, O. Shefi, Nanometric agents in the service of neuroscience: Manipulation of neuronal growth and activity using nanoparticles. *Nanomedicine Nanotechnology, Biol.*

- Med.* **11**, 1467–1479 (2015).
109. M. Zaman, E. Ahmad, A. Qadeer, G. Rabbani, R. H. Khan, Nanoparticles in relation to peptide and protein aggregation. *Int. J. Nanomedicine* **9**, 899–912 (2014).
 110. W. hui Wu, *et al.*, TiO₂ nanoparticles promote β -amyloid fibrillation in vitro. *Biochem. Biophys. Res. Commun.* **373**, 315–318 (2008).
 111. S. Linse, *et al.*, Nucleation of protein fibrillation by nanoparticles. *Proc. Natl. Acad. Sci. U. S. A.* **104**, 8691–8696 (2007).
 112. C. Cabaleiro-lago, *et al.*, Inhibition of Amyloid β Protein Fibrillation by Polymeric Nanoparticles Inhibition of Amyloid Protein Fibrillation by Polymeric. *October*, 15437–15443 (2008).
 113. Y. H. Liao, Y. J. Chang, Y. Yoshiike, Y. C. Chang, Y. R. Chen, Negatively charged gold nanoparticles inhibit Alzheimer's amyloid- β fibrillization, induce fibril dissociation, and mitigate neurotoxicity. *Small* **8**, 3631–3639 (2012).
 114. E. Nance, *The Role of Nanoparticles in Neuroscience* (2019) <https://doi.org/10.33548/scientia383>.
 115. Y. Kim, J. H. Park, H. Lee, J. M. Nam, How Do the Size, Charge and Shape of Nanoparticles Affect Amyloid β Aggregation on Brain Lipid Bilayer? *Sci. Rep.* **6**, 1–14 (2016).
 116. G. Gao, *et al.*, The size-effect of gold nanoparticles and nanoclusters in the inhibition of amyloid- β fibrillation. *Nanoscale* **9**, 4107–4113 (2017).
 117. R. C. Triulzi, *et al.*, Photothermal ablation of amyloid aggregates by gold nanoparticles. *Colloids Surfaces B Biointerfaces* **63**, 200–208 (2008).
 118. Z. Yang, *et al.*, Destruction of amyloid fibrils by graphene through penetration and extraction of peptides. *Nanoscale* **7**, 18725–18737 (2015).
 119. T. Bu, *et al.*, Adsorption and separation of amyloid beta aggregates using ferromagnetic nanoparticles coated with charged polymer brushes. *J. Mater. Chem. B* **3**, 3351–3357 (2015).
 120. H. Skaat, M. Sorci, G. Belfort, S. Margel, Effect of maghemite nanoparticles on insulin amyloid fibril formation: Selective labeling, kinetics, and fibril removal by a magnetic field. *J. Biomed. Mater. Res. - Part A* **91**, 342–351 (2009).
 121. H. Skaat, S. Margel, Synthesis of fluorescent-maghemite nanoparticles as multimodal imaging agents for amyloid- β fibrils detection and removal by a magnetic field. *Biochem. Biophys. Res. Commun.* **386**, 645–649 (2009).
 122. D. Azria, S. Blanquer, J.-M. Verdier, E. Belamie, Nanoparticles as contrast agents for

- brain Nuclear Magnetic Resonance Imaging in Alzheimer Disease diagnosis. *J. Mater. Chem. B* (2017) <https://doi.org/10.1039/C7TB01599B>.
123. M. Kollmer, *et al.*, Electron tomography reveals the fibril structure and lipid interactions in amyloid deposits. *Pnas* **2**, 1523496113- (2016).
 124. R. Hermann, P. Walther, M. Müller, Immunogold labeling in scanning electron microscopy. *Histochem. Cell Biol.* **106**, 31–39 (1996).
 125. E. C. T. Yeung, C. Stasolla, M. J. Sumner, B. Q. Huang, Plant microtechniques and protocols. *Plant Microtech. Protoc.*, 1–572 (2015).
 126. J. Kumar, *et al.*, Detection of amyloid fibrils in Parkinson’s disease using plasmonic chirality. *Proc. Natl. Acad. Sci.* **115**, 3225–3230 (2018).
 127. Y. Yoshiike, T. Akagi, A. Takashima, Surface structure of amyloid- β fibrils contributes to cytotoxicity. *Biochemistry* **46**, 9805–9812 (2007).
 128. P. Delobel, *et al.*, Analysis of tau phosphorylation and truncation in a mouse model of human tauopathy. *Am. J. Pathol.* **172**, 123–131 (2008).
 129. S. Poviloniene, *et al.*, Functionalization of α -synuclein fibrils. *Beilstein J. Nanotechnol.* **6**, 124–133 (2015).
 130. A. M. Jackson, J. W. Myerson, F. Stellacci, Spontaneous assembly of subnanometre-ordered domains in the ligand shell of monolayer-protected nanoparticles. *Nat. Mater.* **3**, 330–336 (2004).
 131. X. Liu, M. Yu, H. Kim, M. Mameli, F. Stellacci, Determination of monolayer-protected gold nanoparticle ligand-shell morphology using NMR. *Nat. Commun.* **3**, 1182 (2012).
 132. P. J. Silva, “Discriminative adsorption of amphiphilic monolayer protected gold nanoparticles on amyloid fibers,” École Polytechnique Fédérale de Lausanne. (2016).
 133. N. Zheng, J. Fan, G. D. Stucky, One-step one-phase synthesis of monodisperse noble-metallic nanoparticles and their colloidal crystals. *J. Am. Chem. Soc.* **128**, 6550–6551 (2006).
 134. R. E. Holmlin, X. Chen, R. G. Chapman, S. Takayama, G. M. Whitesides, Zwitterionic SAMs that resist nonspecific adsorption of protein from aqueous buffer. *Langmuir* **17**, 2841–2850 (2001).
 135. G. Lee, *et al.*, Mapping the surface charge distribution of amyloid fibril. *Appl. Phys. Lett.* **101** (2012).
 136. O. G. Jones, *et al.*, Complexation of β -lactoglobulin fibrils and sulfated polysaccharides. *Biomacromolecules* **12**, 3056–3065 (2011).
 137. E. Cattaneo, C. Zuccato, M. Tartari, Normal huntingtin function: an alternative approach

- to Huntington's disease. *Nat. Rev. Neurosci.* **6**, 919–30 (2005).
138. A. Reiner, I. Dragatsis, S. Zeitlin, D. Goldowitz, Wild-type huntingtin plays a role in brain development and neuronal survival. *Mol. Neurobiol.* **28**, 259–276 (2003).
 139. J. Adamcik, *et al.*, Understanding amyloid aggregation by statistical analysis of atomic force microscopy images. *Nat. Nanotechnol.* **5**, 423–428 (2010).
 140. S. W. Liebman, S. C. Meredith, Protein folding: Sticky N17 speeds huntingtin pile-up. *Nat. Chem. Biol.* **6**, 7–8 (2010).
 141. K. Sathasivam, *et al.*, Aberrant splicing of HTT generates the pathogenic exon 1 protein in Huntington disease. *Proc. Natl. Acad. Sci. U. S. A.* **110**, 2366–2370 (2013).
 142. S. M. DeGuire, *et al.*, N-terminal Huntingtin (Htt) phosphorylation is a molecular switch regulating Htt aggregation, helical conformation, internalization, and nuclear targeting. *J. Biol. Chem.* **293**, 18540–18558 (2018).
 143. L. F. DiGiovanni, A. J. Mocle, J. Xia, R. Truant, Huntingtin N17 domain is a reactive oxygen species sensor regulating huntingtin phosphorylation and localization. *Hum. Mol. Genet.* **25**, 3937–3945 (2016).
 144. A. Chiki, *et al.*, Mutant Exon1 Huntingtin Aggregation is Regulated by T3 Phosphorylation-Induced Structural Changes and Crosstalk between T3 Phosphorylation and Acetylation at K6. *Angew. Chemie - Int. Ed.* **56**, 5202–5207 (2017).
 145. J. R. Arndt, M. Chaibva, J. Legleiter, The emerging role of the first 17 amino acids of huntingtin in Huntington's disease. *Biomol. Concepts* **6**, 33–46 (2015).
 146. M. Goedert, Alpha-synuclein and neurodegenerative diseases. *Nat. Rev. Neurosci.* **2**, 492–501 (2001).
 147. L. Stefanis, α -Synuclein in Parkinson's Disease. 1–24 (2019).
 148. D. Eliezer, The mysterious C-terminal tail of alpha-synuclein: Nanobody's guess. *J. Mol. Biol.* **425**, 2393–2396 (2013).
 149. O. Uzun, *et al.*, Water-soluble amphiphilic gold nanoparticles with structured ligand shells. *Chem. Commun.*, 196–198 (2008).
 150. Z. P. AU - Guven, *et al.*, Synthesis and Characterization of Amphiphilic Gold Nanoparticles. *JoVE*, e58872 (2019).
 151. R. P. Carney, *et al.*, Electrical method to quantify nanoparticle interaction with lipid bilayers. *ACS Nano* **7**, 932–942 (2013).
 152. S. Vieweg, A. Ansaloni, Z.-M. Wang, J. B. Warner, H. A. Lashuel, An Intein-based Strategy for the Production of Tag-free Huntingtin Exon 1 Proteins enables New Insights into the PolyQ Dependence of Httex1 Aggregation and Fibril Formation. *J. Biol. Chem.*

- 291**, 12074–12086 (2016).
153. B. Fauvet, *et al.*, α -Synuclein in central nervous system and from erythrocytes, mammalian cells, and *Escherichia coli* exists predominantly as disordered monomer. *J. Biol. Chem.* **287**, 15345–15364 (2012).
 154. A. S. Cohen, E. Calkins, Electron Microscopic Observations on a Fibrous Component in Amyloid of Diverse Origins. *Nature* **183**, 1813–1814 (1959).
 155. J. Adamcik, R. Mezzenga, Adjustable twisting periodic pitch of amyloid fibrils. *Soft Matter* **7**, 5437–5443 (2011).
 156. A. Sidhu, I. S. Nolten, V. Raussens, M. M. A. E. Claessens, V. Subramaniam, Distinct mechanisms determine α -synuclein fibril morphology during growth and maturation. *ACS Chem. Neurosci.*, aacschemneuro.6b00287 (2016).
 157. L. R. Volpatti, M. Vendruscolo, C. M. Dobson, T. P. J. Knowles, A clear view of polymorphism, twist, and chirality in amyloid fibril formation. *ACS Nano* **7**, 10443–10448 (2013).
 158. S. Assenza, J. Adamcik, R. Mezzenga, P. De Los Rios, Universal Behavior in the Mesoscale Properties of Amyloid Fibrils. *Phys. Rev. Lett.* **113**, 1–5 (2014).
 159. C. Sachse, M. Fandrich, N. Grigorieff, Paired β -sheet structure of an A (1-40) amyloid fibril revealed by electron microscopy. *Proc. Natl. Acad. Sci.* **105**, 7462–7466 (2008).
 160. C. Sachse, *et al.*, Quaternary Structure of a Mature Amyloid Fibril from Alzheimer's A β (1-40) Peptide. *J. Mol. Biol.* **362**, 347–354 (2006).
 161. P. Ganguly, *et al.*, Tau assembly: The dominant role of PHF6 (VQIVYK) in microtubule binding region repeat R3. *J. Phys. Chem. B* **119**, 4582–4593 (2015).
 162. M. Margittai, R. Langen, Side chain-dependent stacking modulates tau filament structure. *J. Biol. Chem.* **281**, 37820–37827 (2006).
 163. K. Minoura, *et al.*, Different associational and conformational behaviors between the second and third repeat fragments in the tau microtubule-binding domain. *Eur. J. Biochem.* **271**, 545–552 (2004).
 164. A. Jan, D. M. Hartley, H. A. Lashuel, Preparation and characterization of toxic A β aggregates for structural and functional studies in Alzheimer's disease research. *Nat. Protoc.* **5**, 1186–1209 (2010).
 165. M. C. Owen, *et al.*, Effects of in vivo conditions on amyloid aggregation. *Chem. Soc. Rev.* **48**, 3946–3996 (2019).
 166. M. Kollmer, *et al.*, Cryo-EM structure and polymorphism of A β amyloid fibrils purified from Alzheimer's brain tissue. 1–8.

167. O. A. Morozova, Z. M. March, A. S. Robinson, D. W. Colby, Conformational features of tau fibrils from alzheimer's disease brain are faithfully propagated by unmodified recombinant protein. *Biochemistry* **52**, 6960–6967 (2013).
168. K. Annamalai, *et al.*, Common Fibril Structures Imply Systemically Conserved Protein Misfolding Pathways In Vivo. *Angew. Chemie - Int. Ed.* **56**, 7510–7514 (2017).
169. G. V Johnson, W. H. Stoothoff, Tau phosphorylation in neuronal cell function and dysfunction. *J. Cell Sci.* **117**, 5721–5729 (2004).
170. M. Fändrich, *et al.*, Amyloid fibril polymorphism: a challenge for molecular imaging and therapy. *J. Intern. Med.* **283**, 218–237 (2018).
171. M. A. Gertz, *et al.*, Diagnosis, Prognosis, and Therapy of Transthyretin Amyloidosis. *J. Am. Coll. Cardiol.* **66**, 2451–2466 (2015).
172. K. Klement, *et al.*, Effect of Different Salt Ions on the Propensity of Aggregation and on the Structure of Alzheimer's A β (1-40) Amyloid Fibrils. *J. Mol. Biol.* **373**, 1321–1333 (2007).
173. S. Bedrood, *et al.*, Fibril structure of human islet amyloid polypeptide. *J. Biol. Chem.* **287**, 5235–5241 (2012).
174. T. Watanabe-Nakayama, *et al.*, High-speed atomic force microscopy reveals structural dynamics of amyloid β ₁₋₄₂ aggregates. *Proc. Natl. Acad. Sci.* **113**, 5835–5840 (2016).
175. A. T. Petkova, W. Yau, R. Tycko, Experimental Constraints on Quaternary Structure in Alzheimer's β -Amyloid. 498–512 (2006).
176. O. Khalaf, *et al.*, The H50Q mutation enhances $\alpha\alpha$ -synuclein aggregation, secretion, and toxicity. *J. Biol. Chem.* **289**, 21856–21876 (2014).
177. F. D'Angelo, *et al.*, A yeast model for amyloid- β aggregation exemplifies the role of membrane trafficking and PICALM in cytotoxicity. *DMM Dis. Model. Mech.* **6**, 206–216 (2013).
178. C. B. Verchere, *et al.*, Islet amyloid formation associated with hyperglycemia in transgenic mice with pancreatic beta cell expression of human islet amyloid polypeptide. *Proc. Natl. Acad. Sci. U. S. A.* **93**, 3492–3496 (1996).
179. E. Scherzinger, *et al.*, Huntingtin encoded polyglutamine expansions form amyloid-like protein aggregates *in vitro* and *in vivo*. **90**, 549–558 (1997).
180. F. Yang, *et al.*, Curcumin inhibits formation of amyloid β oligomers and fibrils, binds plaques, and reduces amyloid *in vivo*. *J. Biol. Chem.* **280**, 5892–5901 (2005).
181. L. M. Byrne, E. J. Wild, Cerebrospinal Fluid Biomarkers for Huntington's Disease. *J. Huntingtons. Dis.* **5**, 1–13 (2016).

182. J. Shi, Fluctuations of CSF amyloid- β levels: Implications for a diagnostic and therapeutic biomarker. *Neurology* **69**, 1063–1065 (2007).
183. T. Tokuda, *et al.*, Detection of elevated levels of α -synuclein oligomers in CSF from patients with Parkinson disease. *Neurology* **75**, 1766–1772 (2010).
184. S. McClendon, C. C. Rospigliosi, D. Eliezer, Charge neutralization and collapse of the C-terminal tail of alpha-synuclein at low pH. *Protein Sci.* **18**, 1531–1540 (2009).
185. Y. Su, P. T. Chang, Acidic pH promotes the formation of toxic fibrils from β -amyloid peptide. *Brain Res.* **893**, 287–291 (2001).
186. G. Ratnaswamy, E. Koepf, H. Bekele, H. Yin, J. W. Kelly, The amyloidogenicity of gelsolin is controlled by proteolysis and pH. *Chem. Biol.* **6**, 293–304 (1999).
187. H. A. Lashuel, C. Wurth, L. Woo, J. W. Kelly, The most pathogenic transthyretin variant, L55P, forms amyloid fibrils under acidic conditions and protofilaments under physiological conditions. *Biochemistry* **38**, 13560–13573 (1999).
188. W. B. Stine, K. N. Dahlgren, G. A. Krafft, M. J. LaDu, In vitro characterization of conditions for amyloid- β peptide oligomerization and fibrillogenesis. *J. Biol. Chem.* **278**, 11612–11622 (2003).
189. Y. Yan, *et al.*, PH-dependent aggregation and disaggregation of native β -lactoglobulin in low salt. *Langmuir* **29**, 4584–4593 (2013).
190. E. Audain, Y. Ramos, H. Hermjakob, D. R. Flower, Y. Perez-Riverol, Accurate estimation of isoelectric point of protein and peptide based on amino acid sequences. *Bioinformatics* **32**, 821–827 (2016).
191. R. C. Van Lehn, *et al.*, Effect of particle diameter and surface composition on the spontaneous fusion of monolayer-protected gold nanoparticles with lipid bilayers. *Nano Lett.* **13**, 4060–4067 (2013).
192. W. Hoyer, D. Cherny, V. Subramaniam, T. M. Jovin, Impact of the acidic C-terminal region comprising amino acids 109-140 on α -synuclein aggregation in vitro. *Biochemistry* **43**, 16233–16242 (2004).
193. H. Kawasaki, K. Hamaguchi, I. Osaka, R. Arakawa, Ph-dependent synthesis of pepsin-mediated gold nanoclusters with blue green and red fluorescent emission. *Adv. Funct. Mater.* **21**, 3508–3515 (2011).
194. S. M. Ansar, S. Chakraborty, C. L. Kitchens, pH-responsive mercaptoundecanoic acid functionalized gold nanoparticles and applications in catalysis. *Nanomaterials* **8**, 1–12 (2018).
195. W. Patungwasa, J. H. Hodak, pH tunable morphology of the gold nanoparticles

- produced by citrate reduction. *Mater. Chem. Phys.* **108**, 45–54 (2008).
196. P. J. Marek, V. Patsalo, D. F. Green, D. P. Raleigh, Ionic strength effects on amyloid formation by amylin are a complicated interplay among debye screening, ion selectivity, and hofmeister effects. *Biochemistry* **51**, 8478–8490 (2012).
 197. R. Huang, R. P. Carney, K. Ikuma, F. Stellacci, B. L. T. Lau, Effects of Surface Compositional and Structural Heterogeneity on Nanoparticle Protein Interactions: Different Protein Configurations. 5402–5412 (2014).
 198. A. Bekdemir, F. Stellacci, A centrifugation-based physicochemical characterization method for the interaction between proteins and nanoparticles. *Nat. Commun.* **7**, 1–8 (2016).
 199. L. M. DiMemmo, *et al.*, Real-time observation of protein aggregates in pharmaceutical formulations using liquid cell electron microscopy. *Lab a Chip - Miniaturisation Chem. Biol.* **17** (2017).
 200. F. M. Ross, Opportunities and challenges in liquid cell electron microscopy. *Science (80-.).* **350** (2015).
 201. H.-G. Liao, H. Zheng, Liquid Cell Transmission Electron Microscopy. *Annu. Rev. Phys. Chem.* **67**, 719–747 (2016).
 202. J. Park, *et al.*, Direct Observation of Wet Biological Samples by Graphene Liquid Cell Transmission Electron Microscopy. *Nano Lett.* **15**, 4737–4744 (2015).
 203. N. De Jonge, F. M. Ross, Electron microscopy of specimens in liquid. *Nat. Nanotechnol.* **6**, 695–704 (2011).
 204. J. R. Silveira, A. G. Hughson, B. Caughey, Fractionation of Prion Protein Aggregates by Asymmetrical Flow Field-Flow Fractionation. *Methods Enzymol.* **412**, 21–33 (2006).
 205. S. Moraes Silva, R. Tavallaie, L. Sandiford, R. D. Tilley, J. J. Gooding, Gold coated magnetic nanoparticles: from preparation to surface modification for analytical and biomedical applications. *Chem. Commun.* **52**, 7528–7540 (2016).
 206. A. Verma, *et al.*, Surface-structure-regulated cell-membrane penetration by monolayer-protected nanoparticles. *Nat. Mater.* **7**, 588–595 (2008).
 207. F. Sousa, *et al.*, Superparamagnetic nanoparticles as high efficiency magnetic resonance imaging T2 contrast agent. *Bioconjug. Chem.* **28**, 161–170 (2017).

Curriculum Vitae

Urszula Cendrowska

Av. D'Echallens 42, 1004 Lausanne, Switzerland

Tel: + 41 78 73 627 45

u.cendrowska@gmail.com

Work experience

- 2019 **Internship** at BASF, Chemical Company, Germany (2 months)
Work heavily oriented on Cryo TEM study of various samples
- 2014 – 2015 **Scientific assistant** at École Polytechnique Fédérale de Lausanne, Laboratory of the Physics of Living Matter, Switzerland (13 months)
Work focused on the AFM study of amyloid fibrils involved in Huntington's disease

Education

- 2020 **Materials Science PhD Thesis:** *Gold nanoparticles as a new tool in amyloid studies*, École Polytechnique Fédérale de Lausanne, Switzerland, Supramolecular Nanomaterials and Interfaces Laboratory (4.5 years)
Work focused on nanoparticle based contrast agent development for Cryo TEM microscopy studies of amyloid fibrils
- 2015 – 2018 **Fellow of Marie Skłodowska-Curie Action** Innovative Training Network (ITN) iSwitch: *Integrated self-assembled Switchable systems and materials: towards responsive organic electronics* (3 years)
- 2014 **Research internship** at École Polytechnique Fédérale de Lausanne, Laboratory of Physics of Living Matter, Switzerland (2 months)
Work focused on the AFM study of amyloid fibrils involved in Huntington's disease
- 2013 **Biotechnology MSc Thesis:** *Influence of FABP 4 gene polymorphism on fatty acids composition in milk from Polish Red cattle*, University of Agriculture, Cracow, Poland (2.5 years)
Research focused on the study of DNA polymorphism and its influence on the level and type of fatty acids and other components in cattle's milk
- 2012 **Research internship** at Ghent University, Faculty of Bioscience Engineering, Belgium (2 months)
A molecular biology study focused on the the problem of declining number of bumblebees in the context of parasites
- 2011 **Biotechnology BSc Thesis:** *Methods of optimization DNA isolation from cow's milk somatic cells*, University of Agriculture, Cracow, Poland (3.5 years)
Research focused on the isolation of the DNA, of the highest purity and amount, from milk somatic cells

Teaching experience

- 2017 – 2018 **Teaching assistant and undergraduate students supervisor**
EPFL Master courses: Biotechnology Lab (BIOENG - 433), Biomaterials (MSE - 471) and undergraduate student supervision
- 2011 – 2013 **Private tutor**
Chemistry and biology for high school and middle school students

Publications

1. Cendrowska U, Silva PHJ , Ait-Bouziad N, Müller M, Guven ZP, Vieweg S, Chiki A, Radamaker L, Thangaraj S, Fändrich M, Tavanti F, Menziani MC, AlexanderNKatz A, Stellacci F, Lashuel HA. *Unraveling the Complexity of Amyloid Polymorphism Using Gold Nanoparticles and Cryo-EM*. Proceedings of the National Academy of Sciences of the United States of America, accepted 2020
2. Guven ZP, Silva PHJ, Luo Z, Cendrowska U, Gasbarri M, Jones ST, Stellacci F. *Synthesis and Characterization of Amphiphilic Gold Nanoparticles*. Jove, 2019
3. DeGuire SM, Ruggeri FS, Fares MB, Chiki A, Cendrowska U, Dietler G, Lashuel HA. *N-terminal Huntingtin (Htt) phosphorylation is a molecular switch regulating Htt aggregation, helical conformation, internalization, and nuclear targeting*. JBC, 2018
4. Chiki A, DeGuire SM, Ruggeri FS, Sanfelice S, Ansaloni A, Wang ZM, Cendrowska U, Burai R, Vieweg S, Pastore A, Dietler G, Lashuel HA. *Mutant exon1 Huntingtin aggregation is regulated by T3 phosphorylation-induced structural changes and crosstalk between T3 phosphorylation and acetylation at K6*. Angewandte Chemie International Edition, 2017
5. Ruggeri FS, Vieweg S, Cendrowska U, Longo G, Chiki A, Lashuel HA, Dietler G. *Nanoscale studies link amyloid maturity with polyglutamine diseases onset*. Scientific Reports, 2016

Professional, computer skills and languages

Scientific skills	<ul style="list-style-type: none">• Expertise in TEM imaging of biological and solid samples• Expertise in Cryo TEM imaging of biological and solid samples• Intermediate AFM imaging skills• Expertise in preparing various types of samples for microscopy measurements• Intermediate laboratory skills from the scope of molecular biology and microbiology• Data treatment, analysis and presentation
Computer skills	Excellent command of Microsoft Office™ tools (Word™, Excel™, Power Point™), good command of data and image processing tools (Origin™, SPIP™, ImageJ, Gwyddion, Pebbles) and graphic programs (Gimp)
Languages	Polish – native, English – fluent, French – conversational

Soft skills and personal interests

Soft skills	<ul style="list-style-type: none">• High communication skills: presentations, discussing, public speaking• Flexibility: adaptability, willing to learn, adjusts easily to rapid changes• Critical thinking: creativity, problem solving, decision making• Positive attitude: patience, humour, courtesy• Works efficiently in a team and individually
Personal interests	<ul style="list-style-type: none">• Amateur journalism• Crafts, video and graphics creation• Travels